AD-A149 473 INVESTIGATION OF A REUSABLE FUEL-AIR EXPLOSIVE NUCLEAR 1/2
AIRBLAST SIMULATOR(U) S-CUBED LA JOLLA CA
T H PIERCE ET AL. 01 FEB 82 SSS-R-81-4897 DNA-5990F
UNCLASSIFIED DNA001-80-C-0067 F/G 18/3 NL

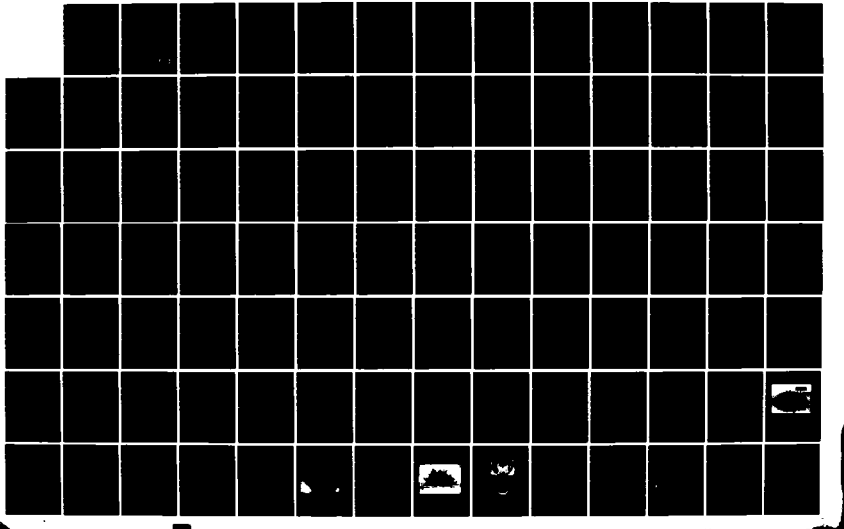

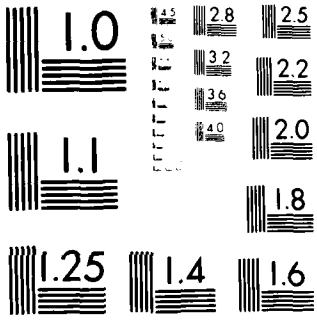

MICROCOPY RESOLUTION TEST CHART
NATIONAL BUREAU OF STANDARDS 1963-A

AD-A149 473

(12)

DNA 5990F

INVESTIGATION OF A REUSABLE FUEL-AIR EXPLOSIVE NUCLEAR AIRBLAST SIMULATOR

T.H. Pierce
R.T. Sedgwick
M.A. Groethe
S-CUBED, A Division of Maxwell Labs, Incoporated
P.O. Box 1620
La Jolla, California 92038

1 February 1982

Final Report for Period 1 January 1980—1 April 1981

CONTRACT No. DNA 001-80-C-0067

APPROVED FOR PUBLIC RELEASE;
DISTRIBUTION UNLIMITED.

THIS WORK WAS SPONSORED BY THE DEFENSE NUCLEAR AGENCY
UNDER RDT&E RMSS CODE B344080464 Y99QAXSD07056 H2590D.

Prepared for
Director
DEFENSE NUCLEAR AGENCY
Washington, DC 20305

DTIC
ELECTE
JAN 23 1985
S D
B

84 11 14 205

Destroy this report when it is no longer needed. Do not return to sender.

PLEASE NOTIFY THE DEFENSE NUCLEAR AGENCY, ATTN: STTI, WASHINGTON, D.C. 20305, IF YOUR ADDRESS IS INCORRECT, IF YOU WISH TO BE DELETED FROM THE DISTRIBUTION LIST, OR IF THE ADDRESSEE IS NO LONGER EMPLOYED BY YOUR ORGANIZATION.

UNCLASSIFIED

SECURITY CLASSIFICATION OF THIS PAGE (When Data Entered)

REPORT DOCUMENTATION PAGE		READ INSTRUCTIONS BEFORE COMPLETING FORM
1 REPORT NUMBER DNA 5990F	2. GOVT ACCESSION NO. AD A119473	3. RECIPIENT'S CATALOG NUMBER
4 TITLE and Subtitle INVESTIGATION OF A REUSABLE FUEL-AIR EXPLOSIVE NUCLEAR AIRBLAST SIMULATOR		5. TYPE OF REPORT & PERIOD COVERED Final Report for Period 1 Jan 80—1 Apr 81
		6 PERFORMING ORG. REPORT NUMBER SSS-R-81-4897
7 AUTHOR(s) T. H. Pierce R. T. Sedgwick M. A. Groethe		8 CONTRACT OR GRANT NUMBER(s) DNA 001-80-C-0067
9 PERFORMING ORGANIZATION NAME AND ADDRESS S-CUBED (A Division of Maxwell Labs, Inc.) P.O. Box 1620 La Jolla, California 92038		10 PROGRAM ELEMENT, PROJECT, TASK AREA & WORK UNIT NUMBERS Subtask Y99QAXSD070-56
11 CONTROLLING OFFICE NAME AND ADDRESS Director Defense Nuclear Agency Washington, DC 20305		12. REPORT DATE 1 February 1982
		13. NUMBER OF PAGES 136
14 MONITORING AGENCY NAME & ADDRESS(if different from Controlling Office)		15. SECURITY CLASS (of this report) UNCLASSIFIED
		15a. DECLASSIFICATION DOWNGRADING SCHEDULE N/A since UNCLASSIFIED

16. DISTRIBUTION STATEMENT (of this Report)

Approved for public release; distribution is unlimited.

17 DISTRIBUTION STATEMENT (of the abstract entered in Block 20, if different from Report)

18 SUPPLEMENTARY NOTES

This work was sponsored by the Defense Nuclear Agency under RDT&E RMSS Code B344030464 Y99QAXSD07056 H2590D.

19 KEY WORDS (Continue on reverse side if necessary and identify by block number)

Fuel-Air Explosions	Blastwaves
Nuclear Airblast Simulation	Pressure Calibration
Detonation	Pressure Measurement
Liquid Dispensing	

20 ABSTRACT (Continue on reverse side if necessary and identify by block number)

Development requirements relating to a reusable, one-kiloton level nuclear airblast simulator using fuel-air explosives is being investigated. The simulator concept is that of a large liquid fuel dispenser, comprising a cluster of radially-directed nozzles. An appropriate fuel would be impulsively injected through this nozzle cluster and the hemispherically-shaped fuel-air cloud so formed would then be detonated. During the contract period reported, work progressed in three areas. These are: the design

DD FORM 1473 EDITION OF 1 NOV 65 IS OBSOLETE

UNCLASSIFIED

SECURITY CLASSIFICATION OF THIS PAGE (When Data Entered)

20 ABSTRACT (Continued)

of an experimental, full-scale single-nozzle disperser; an initial investigation of the sources of secondary compression waves in fuel-air explosions; and improvements in data acquisition procedures.

Accession For
NTIS GRA&I ☑
DTIC TAB ☐
Unannounced ☐
Justification
By
Distribution/
Availability Codes
Dist | Avail and/or Special
A-1

TABLE OF CONVERSION FACTORS TO SI UNITS

To Convert From	To	Multiply By
angstrom	meters (m)	1.000 000 x E -10
atmosphere (normal)	kilo pascal (kPa)	1.013 25 x E +2
bar	kilo pascal (kPa)	1.000 000 x E +2
barn	meter^2 (m^2)	1.000 000 x E -28
British thermal unit (thermochemical)	joule (J)	1.054 350 x E +3
cal (thermochemical)/cm^2	mega joule/m^2 (MJ/m^2)	4.184 000 x E -2
calorie (thermochemical)	joule (J)	4.184 000
calorie (thermochemical)/g	joule per kilogram (J/kg)	4.184 000 x E +3
degree Celsius	degree kelvin (K)	$T_K = t°_C + 273.15$
degree (angle)	radian (rad)	1.745 329 x E -2
degree Fahrenheit	degree kelvin (K)	$T_K = (t°_F + 459.67/1.8)$
electron volt	joule (J)	1.602 19 x E -19
erg	joule (J)	1.000 000 x E -7
erg/second	watt (W)	1.000 000 x E -7
foot	meter (m)	3.048 000 x E -1
foot-pound-force	joule (J)	1.355 818
gallon (U.S. liquid)	meter^3 (m^3)	3.785 412 x E -3
inch	meter (m)	2.54 000 x E -2
kilotons	terajoules	4.183
kip (1000 lbf)	newton (N)	4.448 222 x E +3
kip/inch^2(ksi)	kilo pascal (kPa)	6.894 757 x E +3
ktap	newton-second/m^2 ($N-s/m^2$)	1.000 000 x E +2
micron	meter (m)	1.000 000 x E -6
mil	meter (m)	2.540 000 x E -5
mile (international)	meter (m)	1.609 344 x E +3
ounce	kilogram (kg)	2.834 952 x E -2
pound-force (lbf avoirdupois)	newton (N)	4.448 222

TABLE OF CONVERSION FACTORS TO SI UNITS

(Concluded)

To Convert From	To	Multiply By
pound-force inch	newton-meter (N·m)	1.129 848 x E -1
pound-force/inch	newton/meter (N/m)	1.751 268 x E +2
pound-force/foot^2	kilo pascal (kPa)	4.788 026 x E -2
pound-force/inch^2(psi)	kilo pascal (kPa)	6.894 757
pound-mass (lbm avoirdupois)	kilogram (kg)	4.535 924 x E -1
pound-mass-foot^2 (moment of inertia)	kilogram-meter^2 (kg·m^2)	4.214 011 x E -2
pound-mass/foot^3	kilogram-meter^3 (kg/m^3)	1.601 846 x E +1
shake	second (s)	1.000 000 x E -8
slug	kilogram (kg)	1.459 390 x E +1
torr (mm Hg, 0°C)	kilo pascal (kPa)	1.333 22 x E -1

TABLE OF CONTENTS

LIST OF ILLUSTRATIONS

LIST OF ILLUSTRATIONS (Continued)

LIST OF ILLUSTRATIONS (Continued)

LIST OF ILLUSTRATIONS (Continued)

LIST OF ILLUSTRATIONS (Concluded)

I. INTRODUCTION

A large-scale reusable free-field nuclear airblast simulator based on fuel-air explosives (FAE) has been investigated. A fuel-air explosive consists of a combustible atmospheric dispersion of fuel droplets, fuel vapor, or a combination of these. Subsequent explosion of the fuel-air cloud is induced in the detonative (as opposed to deflagrative) mode. This results in peak explosion overpressures on the order of 2 MPa (300 psi), developed as the detonation front propagates through the cloud.

The feasibility of an FAE nuclear airblast simulator is contingent on developing a technique to very rapidly form an unconfined fuel-air cloud of the required size. The usefulness of the simulator would also depend on the degree to which a cloud so formed and detonated simulates a nuclear airblast, at least in the sense of producing correct target response.

In order to generate the highest usable overpressure levels from a given fuel-air cloud, hemispherical cloud geometry is desirable. With other geometries, the airblast emerging from the detonated fuel-air cloud would not be expected to be point symmetric in the cloud vicinity. The cloud formation scheme that has been under investigation for producing hemispherical clouds is that of impulsive liquid fuel injection from a central dispensing source on the ground. The fuel is forced at high pressure through a large number of hydraulic nozzles aimed in directions that are distributed uniformly throughout the hemispherical volume of air. It has been estimated that a 1 KT simulation would require a cloud with a radius of 71 m (233 ft) and containing 85,400 kg (188,000 lbm) of fuel (assuming propylene oxide).

Earlier research at Systems, Science and Software (S^3) addressed various aspects of the physical, technological, and engineering/economic feasibility of an FAE/nuclear airblast simulator. These efforts are discussed in detail in References 1 and 2.

In early experimental work (Ref 1), small-scale fuel-air clouds (1/4 ton nuclear equivalent, nominal) were formed and detonated, and full-scale jets from single nozzles were tested. The small-scale propylene oxide/air clouds were reasonably hemispherical in outline but they were not well filled in with spray because too few nozzles were used. In order to detonate these clouds with good results it was found necessary to allow the clouds to dwell for some time (1 - 2 seconds) after their initial formation. At the time of detonation, the clouds had settled into non-hemispherical shapes. The dwell time that was allowed for settling and evaporation resulted in explosions with relatively high effective blast yield (74 percent of the heat of combustion). However, it was recognized that long dwell times could not be tolerated in practice due to problems with cloud displacement by wind. In more recent tests, the dwell time was reduced. While the clouds formed were not perfectly nemispherical, pressure waveforms in these tests were similar to nuclear airblast curve fits with the exception that many of the waveforms contained second shocks of unidentified origin.

Early tests with large-scale jets from single nozzles achieved projection of propylene oxide to a distance of about 55 m (180 ft). This was short of the 71 m (233 ft) jet reach necessary to develop a fuel-air cloud at the 1 KT nuclear level. It was felt that reach was being limited by the fuel pressurization system (dispenser) which was capable of pressures up to about 0.5 MPa (75 psi). In addition, the piston used in this early dispenser was relatively small. As a result, when large nozzles were used, the dispenser start-up time was comparable to the total dispensing time.

In an attempt to achieve greater reach, a dispenser having a much larger piston was designed. The piston in this second-generation dispenser was driven by a gas generator which provided dispensing pressures up to about 1.6 MPa (230 psi). The start-up

time of the new dispenser was sufficiently fast; however, the anticipated increases in jet reach nave not as yet been realized. Based upon experiments with smaller jets, it is currently believed that while somewhat higher dispensing pressures are still needed, the primary obstacle to increased jet reach is the fuel capabity of the dispenser.

The present report summarizes progress made during 1980 in three areas; namely, the design of a high-capacity, high-pressure impulsive fuel dispensing system, an assessment of the possible causes of secondary waves that have been observed in fuel-air explosions, and improvements in instrumentation which were made to enhance the quality of the pressure data. These areas are discussed respectively in Sections II through IV. Concluding remarks and recommendations for further work are given in Section V.

II. LARGE CAPACITY IMPULSIVE FUEL DISPENSER

A full-scale FAE/nuclear airblast simulator at 1 KT equivalent yield would impulsively form and then detonate hemispherical fuel-air clouds on the order of 71 m (233 ft) radius. To demonstrate that individual fuel jets can be projected to distances of this magnitude, a dispenser with considerably greater capacity than that of the existing unit (Reference 2) is required. A dispenser having 0.42 m^3 (110 gal) capacity and 14 MPa (2000 psi) operating pressure capability was designed and engineered during the presently reported contract period. Details of the design considerations are discussed in this section.

1. BASIC DESIGN REQUIREMENTS

Previous S^3 work with hydraulic jets discharged from single nozzles (References 1 and 2) has indicated the general influence on jet reach of nozzle diameter, jet discharge velocity, and the quantity of fuel dispensed. Figure 1 illustrates that, at fixed nozzle diameter, the maximum jet travel (reach) first increases with nozzle pressure drop (or jet velocity) and then levels off or decreases somewhat. Above the knee of the curve, which occurs roughly at 0.6 MPa (90 psi) in Figure 1, a substantial increase in the degree of jet atomization and transverse jet spreading is observed. The pressure at the knee is considered the minimum level that is useful for generating well atomized jets.

Figure 2 shows that, as would be expected, jet reach increases with nozzle diameter. Typical jet reach is in the range of 1000-2000 nozzle diameters, with 1500 being a useful rule-of-thumb value for hydrocarbon fuels.

In Figure 3, the effect of the quantity of fuel dispensed on jet reach is illustrated. The jet reach drops off rapidly when the quantity dispensed is below a certain level. This is believed to be due to breakup of the jet tail when the jet is short (low dispensed

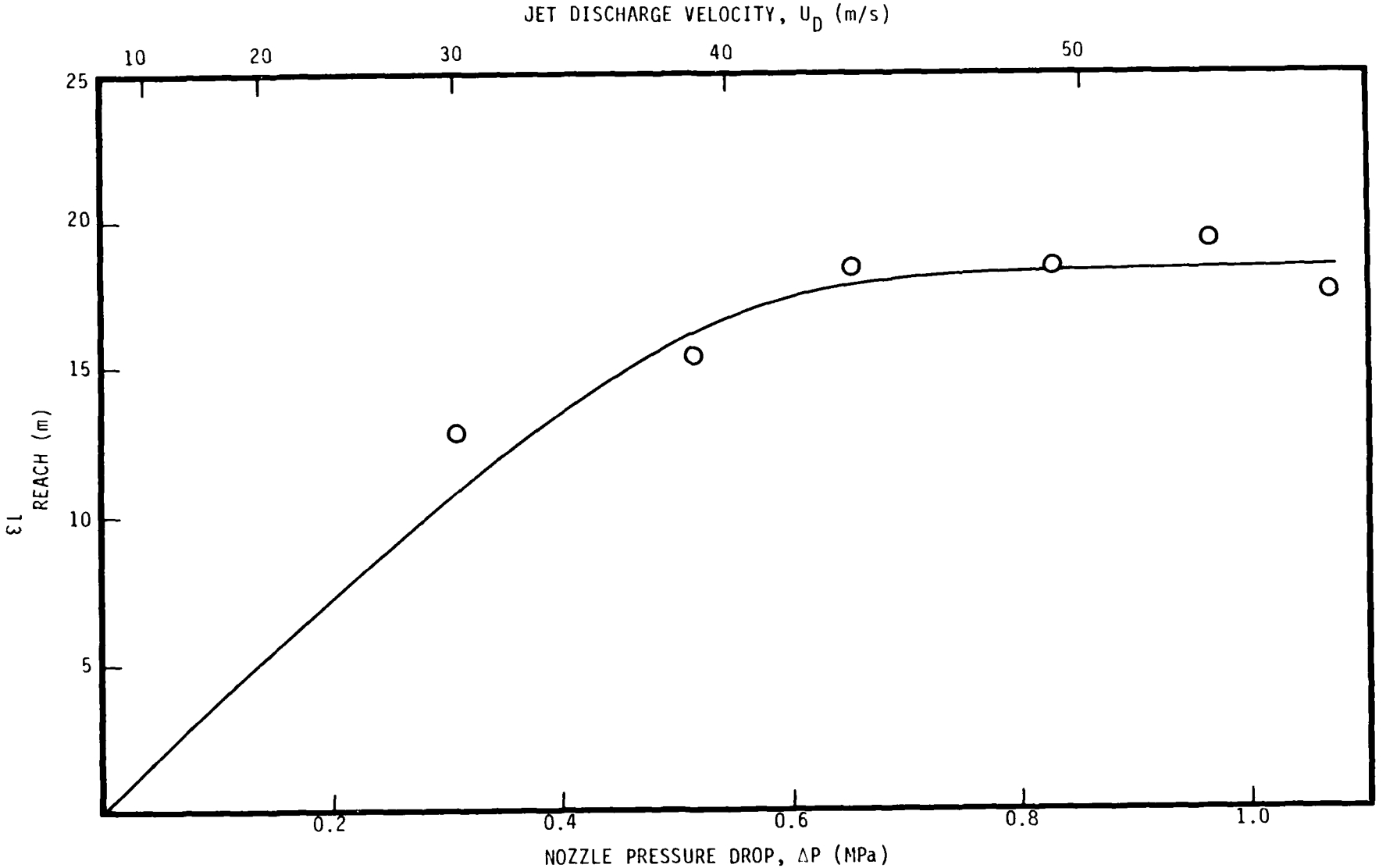

Figure 1. Ultimate jet reach versus pressure drop and velocity for heptane, 1.27 cm (0.5 in.) diameter nozzle.

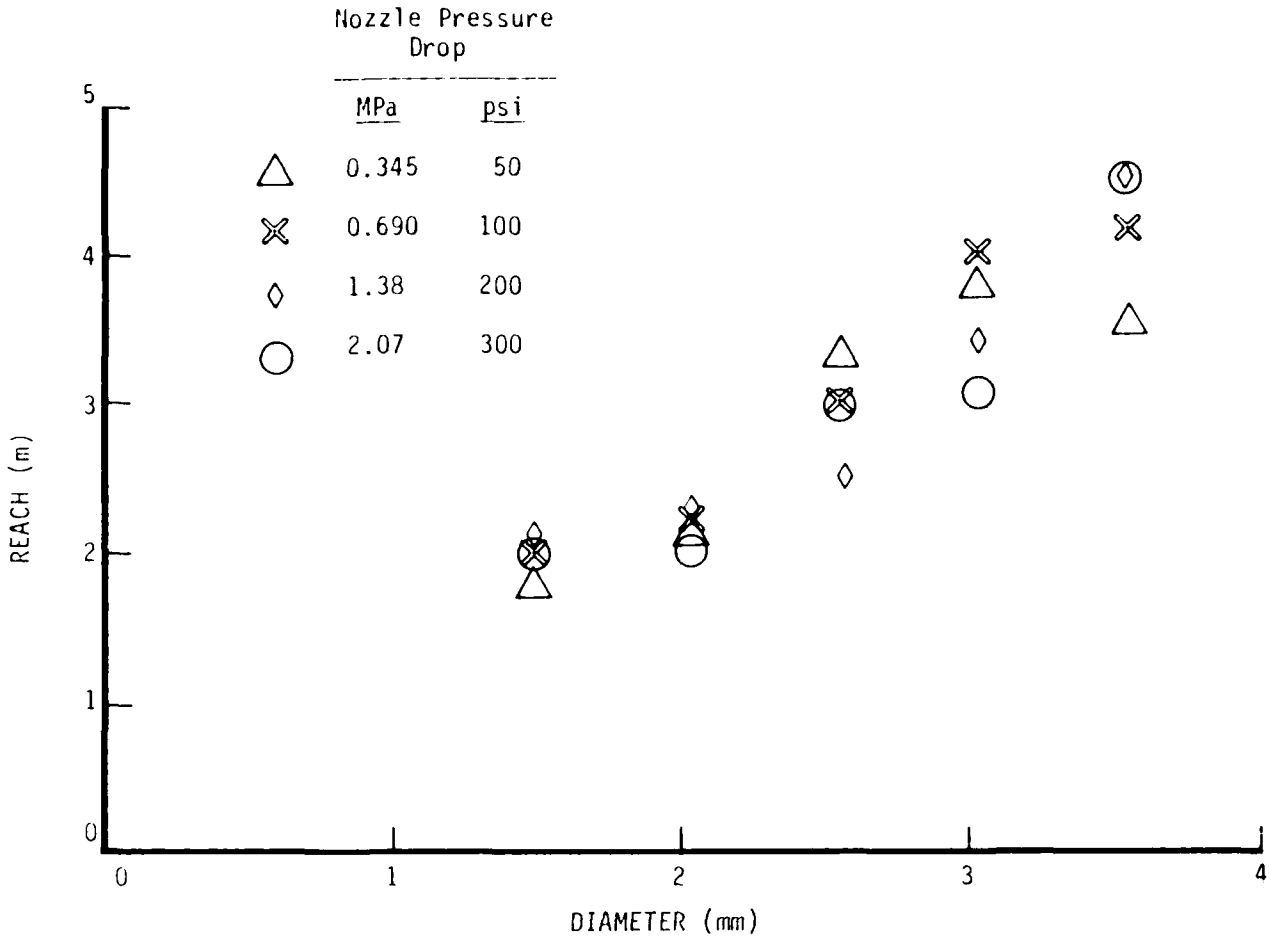

Figure 2. Ultimate jet reach versus nozzle diameter (kerosene jets).

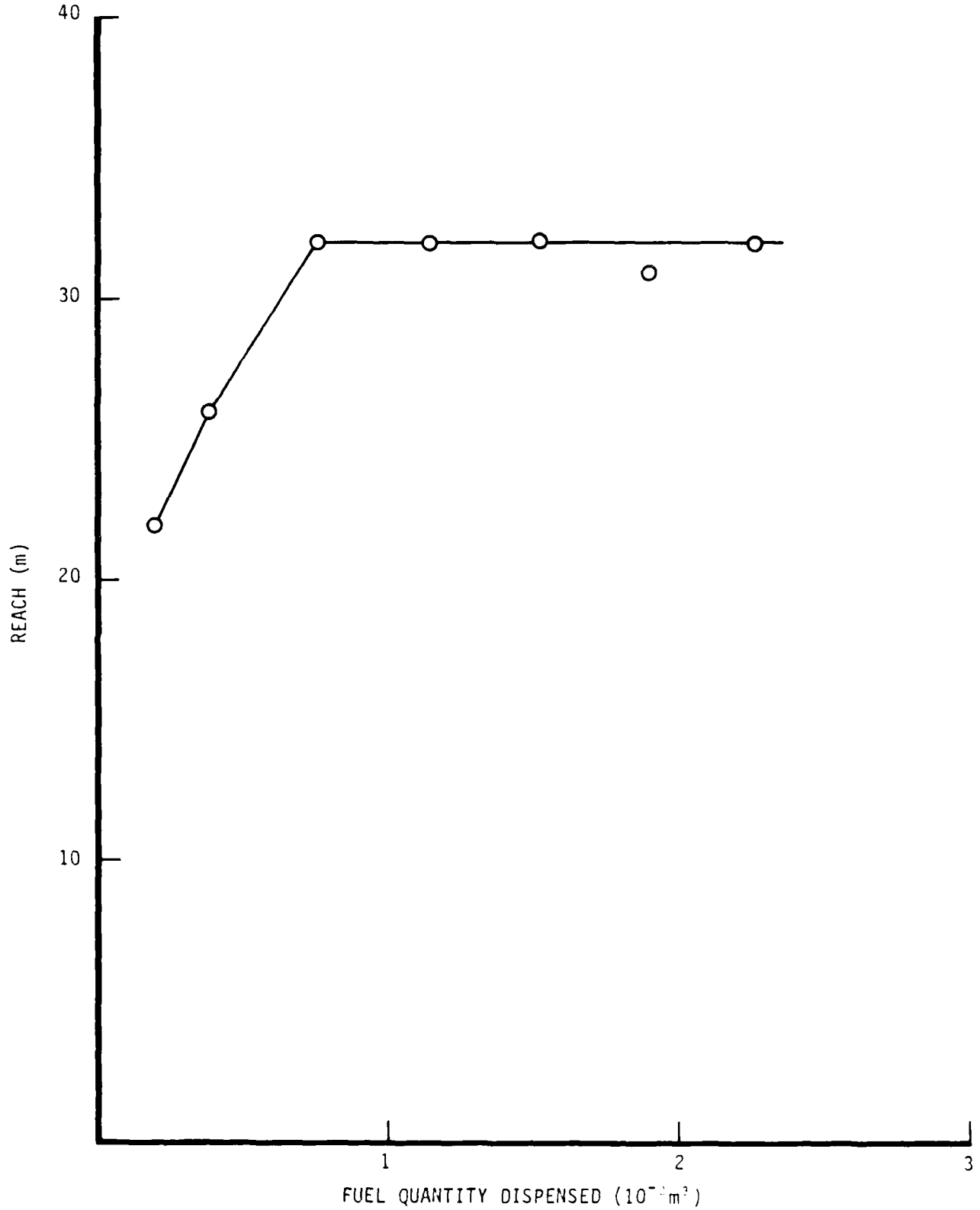

Figure 3. Ultimate jet reach versus fuel quantity dispensed. (2.54 cm (1 in.) diameter nozzle, heptane, nominal driving pressure = 1.23 MPa (180 psi)).

fuel quantity). The disturbance responsible for tail breakup rapidly propagates toward the jet nose (or head), causing premature jet rupture and diminished reach. A semi-empirical relation for the smallest volume of liquid that can be dispensed without reach reduction was derived in Reference 2. The result is

$$V_{F_{min}} = 0.428\ u_D \left(\frac{\rho_\ell D_N^7}{\sigma_\ell} \right)^{1/2} , \qquad (1)$$

where u_D is jet discharge velocity, D_N is nozzle diameter, and ρ_ℓ, σ_ℓ are the fluid density and surface tension respectively.

Although these three basic features of impulsive jet breakup have been investigated in survey experiments, a series of tests in which the controlling parameters are systematically varied has not as yet been conducted. Because of this, the design requirements for the full-scale single jet dispenser were necessarily based on some rather crude estimates.

A limited number of experiments had earlier been carried out with small diameter, steady-state (continuous) jets (Ref. 2). In those experiments, it appeared that the atomization of 0.36 cm (0.14 in) diameter propylene oxide jets diminished substantially below jet velocities of about 25 m/s (82 ft/s). For present purposes, it was assumed that this velocity is the minimum that would result in full reach. More recent tests with heptane, dispensed through a 2.5 cm (1 in) diameter nozzle, indicated for this size nozzle that the minimum velocity for full reach is about 40 m/s (130 ft/s) (see Figure 1). Based on these two data points, a very rough extrapolation to larget jet sizes was made. In SI units this extrapolation is

$$u_{D_{min}} = 700\ D_N + 22.5. \qquad (2)$$

If jet reach is taken to be 1500 nozzle diameters, then a nozzle of 0.06 m (2.36 in) diameter would be required for a jet to

reach 90 m (295 ft). From Equation (2), the jet velocity would then have to be at least u_D = 64.5 m/s (211 ft/s) for the jet to attain the 90 m (295 ft) reach and to be at least minimally atomized. This velocity corresponds to a nozzle pressure drop of 1.42 MPa (206 psi) for heptane. Finally, from Equation (1), at least 0.264 m^3 (70 gal) of heptane (σ_ℓ = 0.0209 N/m (0.00143 lb/ft)) would have to be dispensed through the nozzle.

Due to the considerable uncertainty of these coarse estimates, it was felt that the large dispenser should be substantially over-designed. For this reason it was decided that the dispenser would be designed to operate at 14 MPa (2000 psi), have a maximum capacity of 0.42 m^3 (110 gal), and be capable of accommodating nozzles as large as 0.1 m (4 in) diameter.

2. DISPENSER CONFIGURATION

Several possible dispenser configurations were described in Reference 2. Among the various options, those in which the fluid is discharged by a high pressure gas that is separated from the fluid by a piston were judged most practical. Working experience was previously gained with two dispenser configurations of this type. In one (Figure 4), the driver gas flowed from a source container through an orifice constriction and into a free volume (an initially void region) behind the piston. In concept this is a good design because the pressure drop-off after startup in the free volume (which increases during dispensing) can be minimized with a relatively small driver gas source volume. However, the orifice used witn the device in Figure 4 was rather small so that the initial piston acceleration was quite sluggish. In addition, very high source pressures were needed to obtain the desired free volume pressure levels.

The second dispenser configuration tested employed a gas generator to elevate the free volume pressure. This design (Figure 5) eliminated the need for a compressed gas source. An arrangement

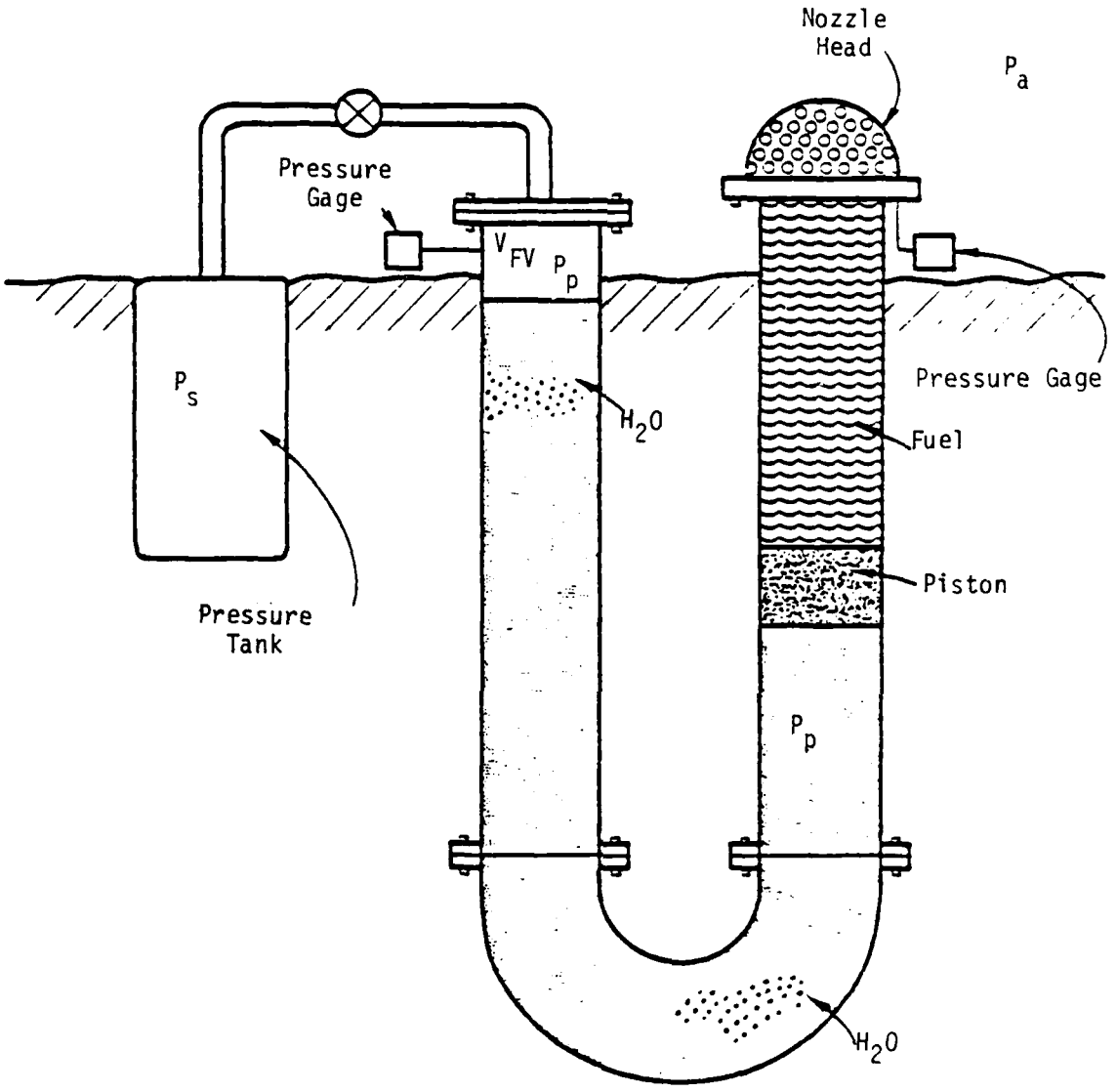

Figure 4. Schematic diagram showing the U-tube used in the experimental investigation for disseminating fuel to form hemispherical fuel-air explosive clouds. One leg of the U-tube was pressurized in order to force the fuel through a nozzle head attached to the other leg of the U-tube.

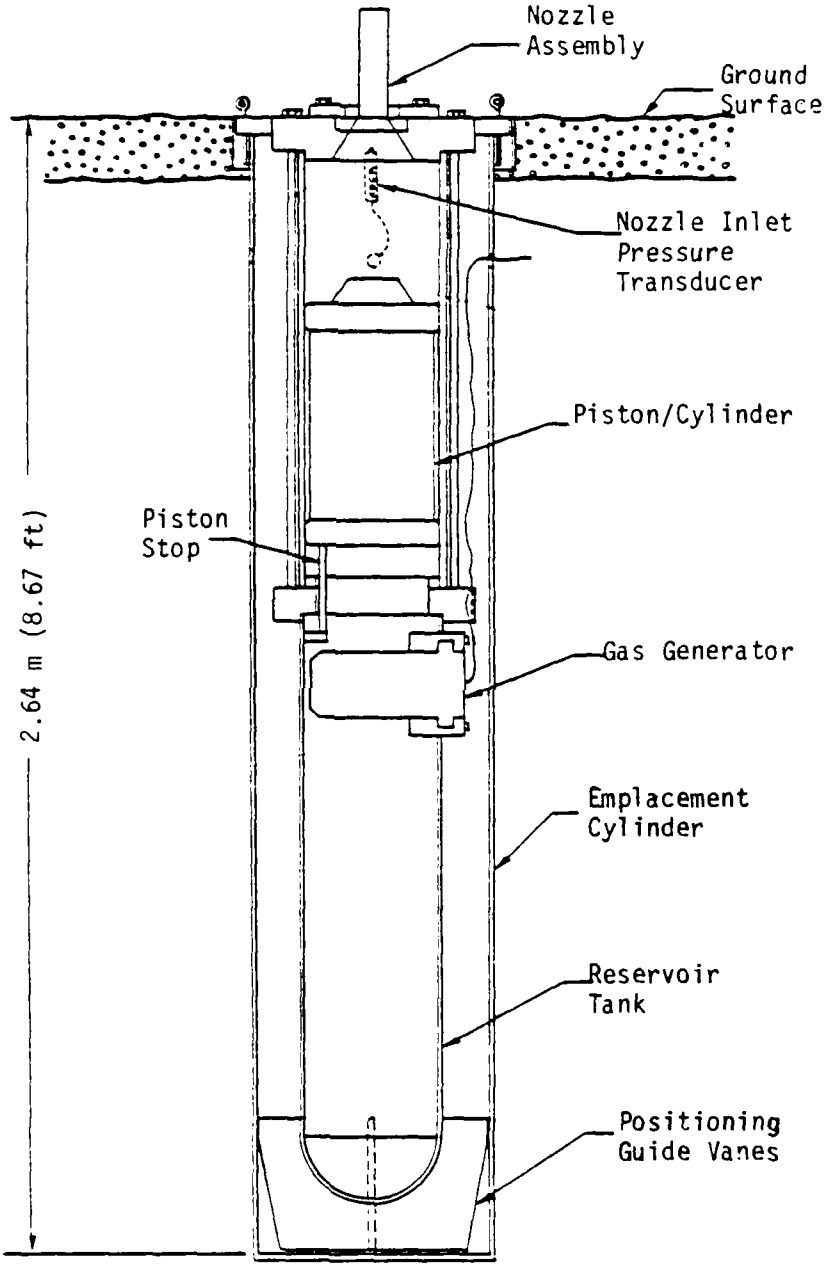

Figure 5. Schematic of linear fuel dispenser.

of this type could be quite successful if the propellant were tailored to raise the free volume pressure rapidly at first, and to then burn more slowly so as to sustain the pressure while dispensing progresses. In the experimental unit that was built, the propellant used was smokeless powder (Hercules Red Dot). The products of combustion of this propellant were restrained in a breech by a diaphragm until combustion was nearly completed. The products were then exhausted impulsively into the free volume. This fast blowdown resulted in very rapid initial free volume pressure rise and in good piston acceleration. However, during dispensing the free volume pressure decreased substantially due to gas expansion and heat transfer.

A gas generator designed to meet the needs of a full-scale simulator installation would appear at present to be the most promising piston driver option. However, for experimental single-nozzle work, it is necessary to test a wide range of nozzle sizes, driver pressures, and dispensed fuel quantities. Since a different tailored gas generator would be required for each such variation, this approach would be very costly. For that reason, further use of gas generators in the experimental work was not considered advisable.

Three configurations were considered for the large capacity dispenser. These are illustrated schematically on Figure 6. The first (Figure 6a) would use ambient temperature air or nitrogen for the driver gas. The high-pressure gas source container would be directly linked to the dispenser cylinder as shown. The piston would be initially restrained from motion by a cable that would then be severed using an explosive actuator to start fluid dispensing. This configuration has the advantage that the initial piston acceleration is maximized for any given supply pressure, since the piston is exposed to the full supply pressure in advance of the event that starts the test. On the other hand, explosive actuators of the size needed for this application would represent a nontrivial

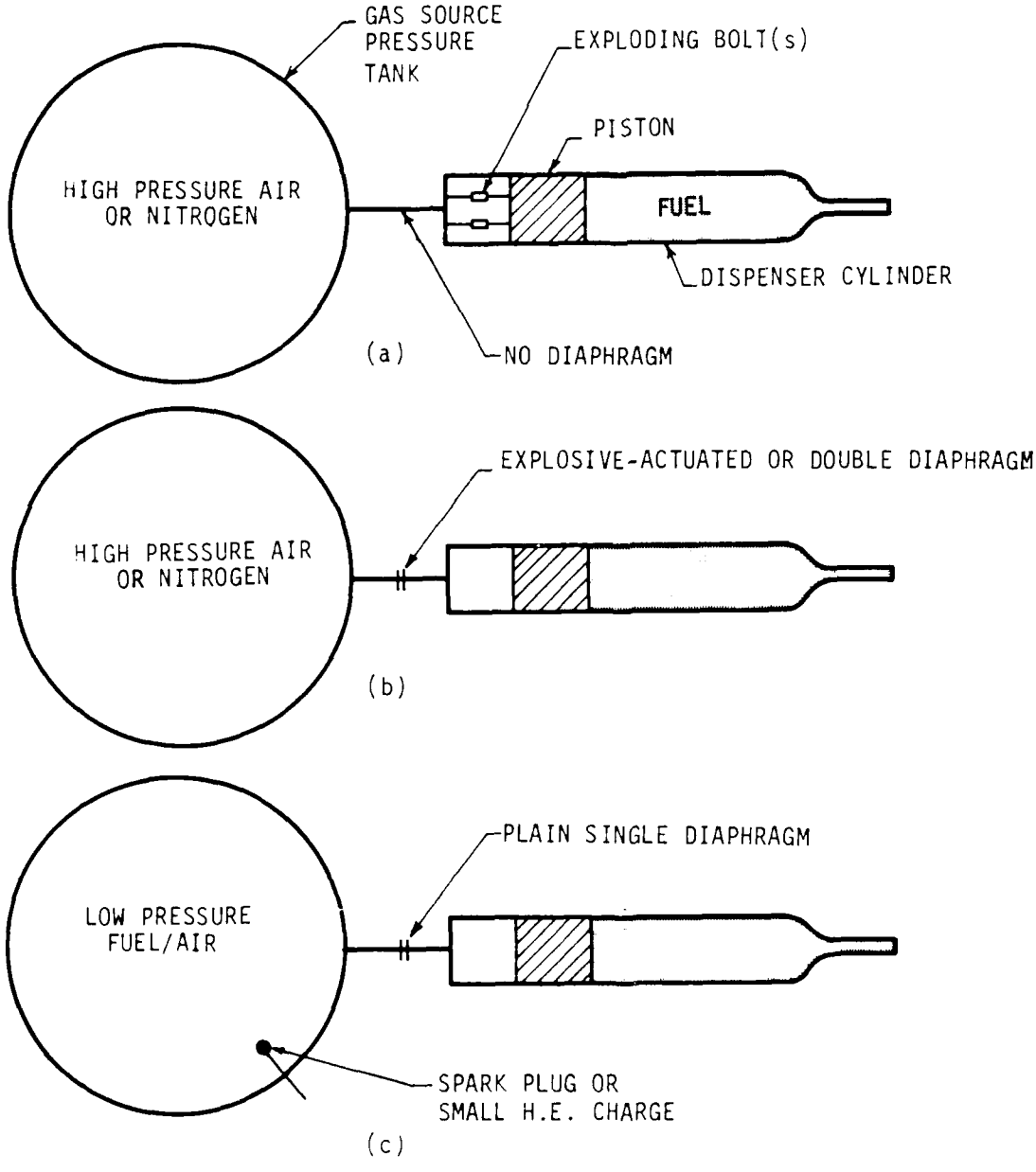

Figure 6. Large capacity dispenser configurations.

added expense. Additionally, provisions would have to be made to access the area behind the piston so as to enable replacement of the explosive actuators.

The second dispenser configuration that was considered, Figure 6b, would also make use of a large-volume air or nitrogen gas supply. In this case, however, the space (if any) behind the piston would be initially at ambient pressure. A diaphragm would be located in the connecting plumbing between the supply vessel and the dispenser cylinder. To start the dispensing process, this diaphragm would be ruptured. Fast rupture would be accomplished through the use of a small explosive device, or by means of any of the techniques used commonly in shock tubes, such as a double-diaphragm arrangement. Fast diaphragm opening is essential for adequate piston acceleration performance; the opening of an electrically or air actuated valve is much too slow for this application. The configuration of Figure 6b would be simpler to build and to operate than that of Figure 6a. However, the initial piston acceleration would be somewhat slower than that in the design of Figure 6a, for equivalent driver pressures. This is due to the time required for pressure to develop in the space behind the piston.

The designs in Figures 6a and 6b both require a considerable quantity of high pressure air or nitrogen. High pressure air could be loaded with a compressor. The use of such compressors requires extreme care, however, due to the possibility for explosion. The supply gas vessel would also have to be kept extremely clean for the same reason. In addition, a fairly large compressor would be needed to avoid extended pump-up time. It is felt far preferable to use nitrogen gas rather than compressed air. Nitrogen can be supplied at the time of use from large trailor-mounted transport containers. In this case, loading of the gas source vessel would take only a few minutes and there would be no hazard of explosion. On the other hand, in the quantities required, the cost of the nitrogen and delivery service would be several hundred dollars per test.

The third dispenser design considered is that of Figure 6c. Here the arrangement is identical to that of Figure 6b except that combustion products from a gas-phase fuel-air explosion are used as the driver gas. The gas supply bottle would be charged with a fuel-air mixture, at relatively low initial pressure, which would be detonated to start the test. A diaphragm would be used (as in the design of Figure 6b); however, in this case, only a plain, single diaphragm would be needed, and the diaphragm would have only to withstand a much lower initial pressure. Alternately, the fuel-air mixture could be deflagrated (ignited by a spark plug) and a thicker diaphragm employed which would rupture when the combustion product pressure was near its maximum level. The combustion driver scheme would by far have the lowest expendible materials cost per test of the three options in Figure 6. It would also have the greatest safety if fuel injection were to be done remotely just before a test, since there would be no extended period of high pressure gas storage. However, it is not known how accurately the fuel and air can be mixed (if they are loaded separately); poor mixing would compromise test repeatibility. Also, the supply gas pressure vessel would have to be capable of sustaining the pressures developed behind a reflected detonation at the vessel walls.

To promote fuel-air mixing, a number of small fuel containers could be located at various points on the pressure vessel and discharged into it simultaneously. The highest possible discharge velocity would be used to encourage turbulent mixing within the vessel. This suggests that the fuel chosen should have a high vapor pressure (since it would be supplied from standard gas cylinders). A promising candidate fuel, for example, would be ethylene, which is relatively inexpensive and has a vapor pressure or approximately 8.3 MPa (1200 psi).

The constant-volume combustion characteristics of initially stoichiometric ethylene-air mixtures were computed using the S[3] URAKL code. The code computes the product state which is in

thermodynamic and chemical equilibrium. The result, plotted on Figure 7, is an essentially linear relation between the final pressure P_2 and the initial mixture pressure, P_1, such that $P_2/P_1 \doteq 9.6$.

A large pressure vessel, located at the S^3-operated Green Farm Test Site, was available for use with the high capacity dispenser. This is a spherical explosion vessel that had previously been used for confined detonation experiments, and which is capable of withstanding very high pressures. The vessel has an internal volume of approximately 3.21 m^3 (113 ft^3). The quantity of ethylene that it would be necessary to inject into this vessel (with the appropriate amount of air) was calculated from the perfect gas law and is plotted for reference on Figure 8.

Two other simple calculations relating to the combustion driver design are of interest. If the fuel-air mixture detonates within the pressure vessel, the pressures sustained on the vessel walls will be considerably in excess of the equilibrium, constant-volume level. For stoichiometric ethylene-air mixtures, the detonation pressure is about 17.1 times the initial mixture pressure. If this detonation reflects normally from a surface, a simplified calculation shows that the reflected pressure could be expected to be about 33.2 times the initial mixture pressure. To achieve a final equilibrium pressure of 13.8 MPa (2000 psi) throughout the vessel requires an absolute initial ethylene-air pressure of P_1 = 1.44 MPa (209 psi), so that in this extreme case the reflected detonation pressure would reach 47.8 MPa (6930 psi). The spherical explosion vessel mentioned above had been hydrotested when new to 52 MPa (7500 psi) and so it was thought that it would be suitable for this service.

Finally, an estimate of the explosion vessel wall temperature, after thermally equilibrating with the combustion products, was also made. The explosion vessel is made of steel and has a mass of approximately 1.54 x 10^4 KG (17 tons). For the extreme case of

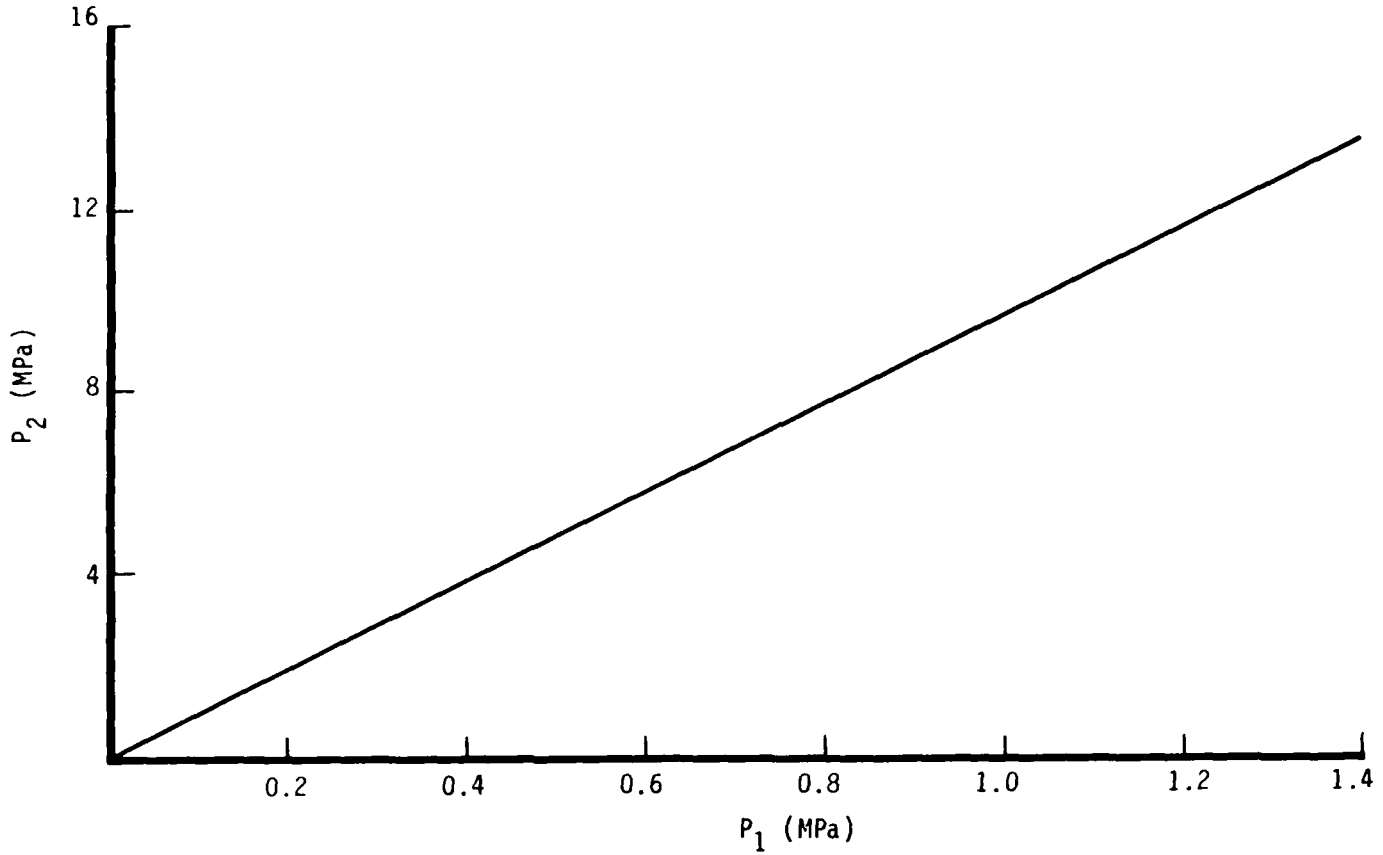

Figure 7. Equilibrium product pressure, P_2, versus initial reactant mixture pressure, P_1, for constant volume combustion of ethylene in air. Initial temperature is 300°K.

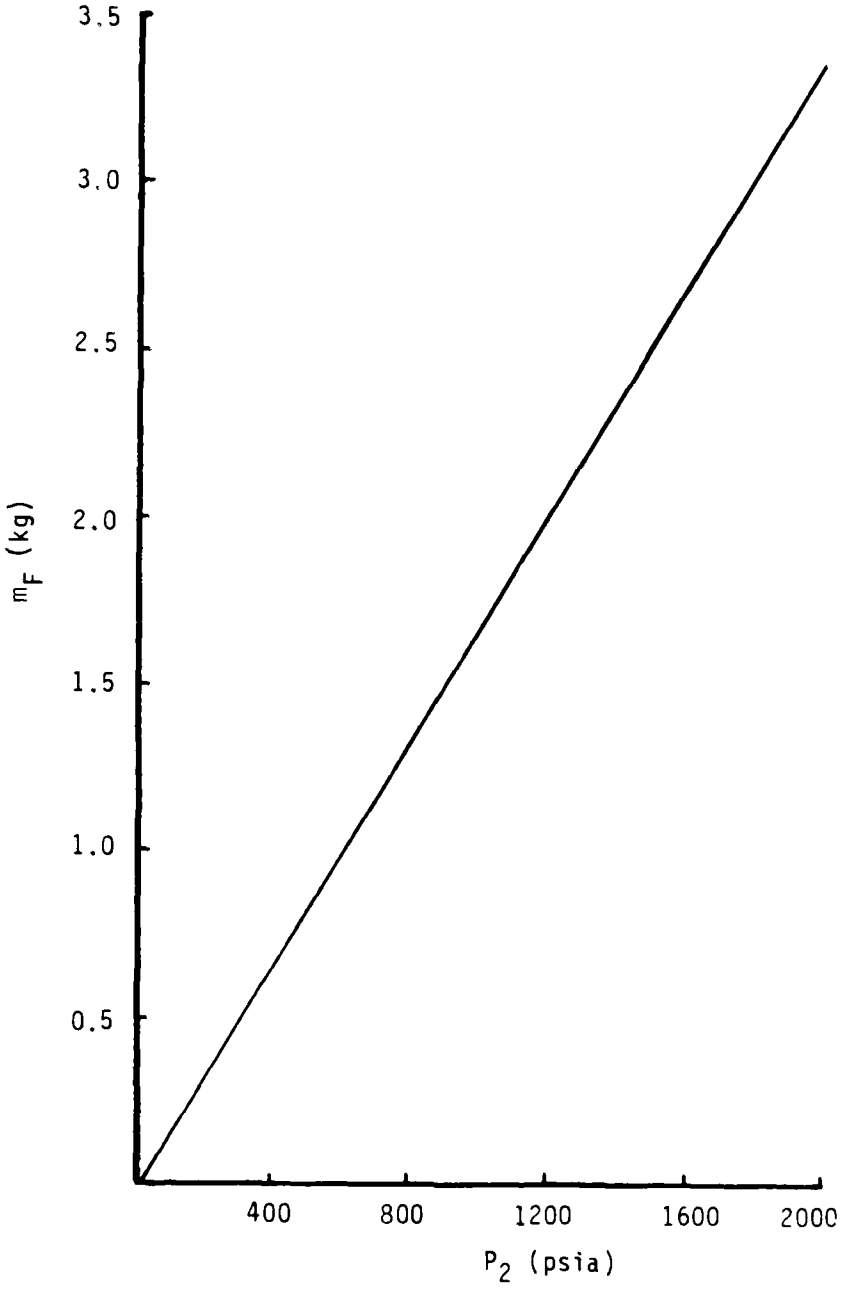

Figure 8. Mass of ethylene required for stoichiometric mixture with air in explosion vessel, m_F, versus combustion product pressure at constant volume, P_2, explosion vessel volume = 3.21 m^3 (113 ft^3).

ethylene combustion products at 13.8 MPa (2000 psi), a straightforward First Law analysis gave an expected wall temperature rise of approximately 21°C (38°F) above the initial ambient level. This was regarded as negligible.

All three of the dispenser configurations that have been described are considered viable. At the time of this writing, the arrangement of Figure 6b is favored in spite of its higher per-test cost. This is because that design appears to offer the greatest experimental control with minimal operating complexity. However, it was felt that the three configurations were similar enough that the design of the dispenser should be such as to accommodate all three. At small additional cost, this would permit the flexibility to change driver options should such a change become desirable.

3. DISPENSER SIZING AND PERFORMANCE CALCULATIONS

The fundamental design variable in sizing the dispenser is the diameter of the piston. For fixed dispensed-liquid capacity and maximum operating pressure, the cost of the dispenser assembly increases with piston diameter. As this diameter is increased, the cylinder wall thickness, the size of the cylinder end caps and the sizes of all seals increase. In addition, larger fabricating equipment is required, at generally greater cost. However, a large piston diameter improves dispenser performance and minimizes the overall cylinder length (which simplifies installation). Because of these tradeoffs, it was decided to select the smallest piston diameter consistent with performance requirements and with readily available cylinder lengths.

The total internal volume of the dispenser cylinder is simply the sum of the volumes occupied by the piston and by the maximum amount of fluid to be dispensed. In Figure 9 the associated overall cylinder length is plotted as a function of inside (or piston) diameter, assuming that the piston length is twice its diameter (for stability). As can be seen, rather unwieldly cylinder lengths would be needed for piston diameters much smaller than about 30 cm (12 in.).

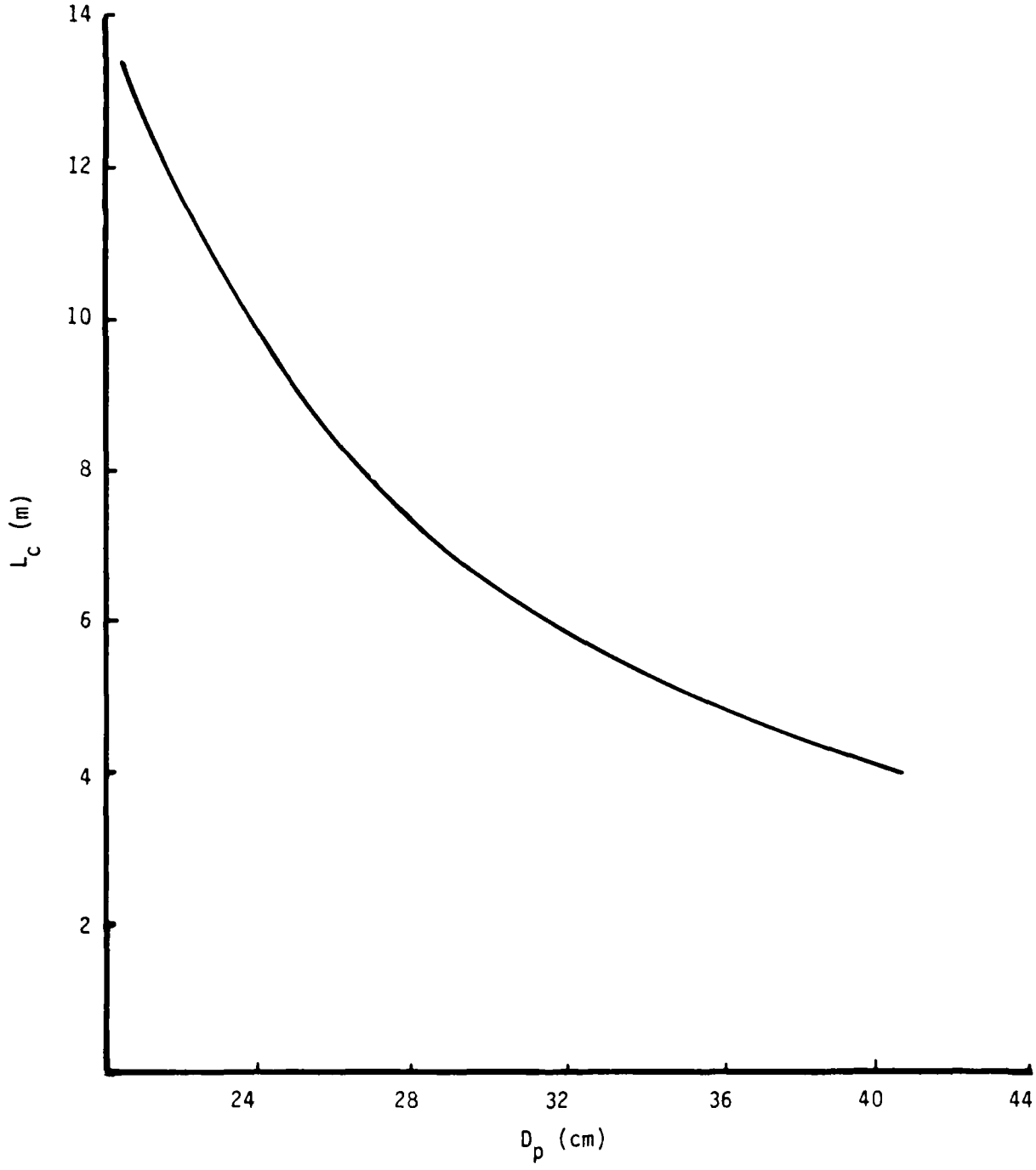

Figure 9. Total cylinder length L_c versus inside diameter for fuel volume V_ℓ = 0.417 m^3 (110 gal).

Dispenser performance was analyzed to first order with a simplified model. The sketch in Figure 10 defines the various pressures, temperatures, masses, and volumes that are involved. Since the maximum value of V_F is much less than V_C, changes in the pressure-vessel pressure and temperature were ignored. Frictional effects in the connecting pipe were also neglected (these are discussed later in this Section). The smallest area in the connecting plumbing, here referred to as the orifice, is A_O. The fluid pressure was assumed to be uniform throughout the liquid reservoir (the velocity throughout was taken to equal the piston velocity). Characteristic time intervals corresponding to significant changes in the value of P_ℓ were assumed to be long compared to characteristic sound propagation times through the liquid. The liquid flow through the nozzle was accordingly treated as quasi-steady, and the Bernoulli equation was used.

The equation of motion for the piston under these conditions is

$$(m_\ell + m_P)\frac{du_P}{dt} = (P_F - P_A)A_P - \frac{1}{2}\rho_\ell u_P^2 A_P\left[\left(\frac{A_P}{A_N}\right)^2 - 1\right] \tag{3}$$

where u_P is the piston velocity, P_A is ambient atmospheric pressure, and ρ_ℓ is the fluid density. This equation was derived in Reference 2. The rate of fluid efflux from the dispenser is

$$\frac{dm_\ell}{dt} = -\rho_\ell u_D A_N \tag{4}$$

where the discharge (jet) velocity is (from mass conservation)

$$u_D = \frac{u_P A_P}{A_N} \quad . \tag{5}$$

It is also noted that

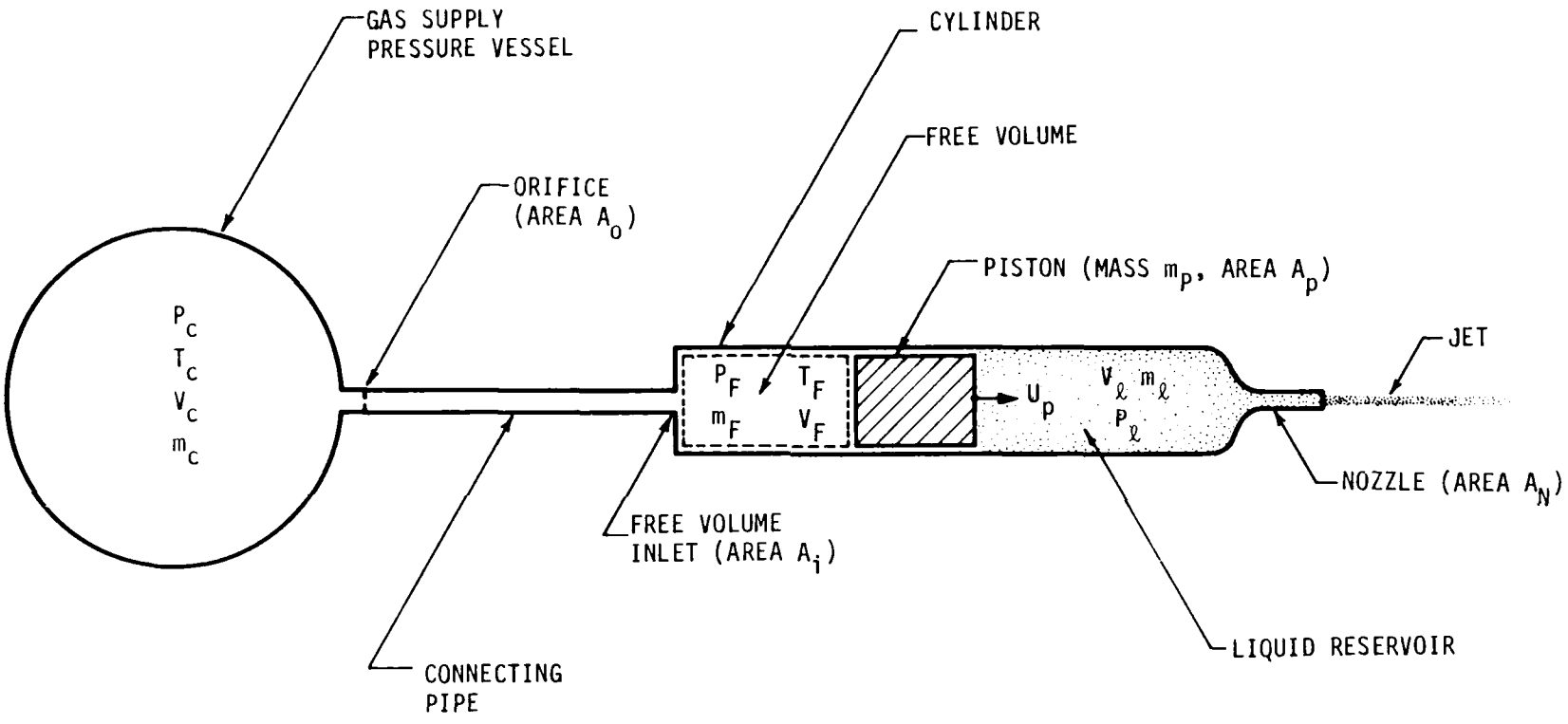

Figure 10. Arrangement for dispenser performance analysis.

$$m_\ell = \rho_\ell V_\ell \tag{6}$$

where

$$V_\ell + V_F = V_T \tag{7}$$

expresses the constancy of the total cylinder volume ahead of and behind the piston at all times. Finally, the fluid pressure P_ℓ is related to the piston velocity by

$$P_\ell = P_A + \frac{1}{2}\rho_\ell u_p^2 \left[\left(\frac{A_P}{A_N} \right)^2 - 1 \right] \tag{8}$$

from the Bernoulli equation.

In order to evaluate Equations (2) - (8), the time varying free volume pressure, $P_F(t)$, must be known. This was calculated from thermodynamic principles, using the expanding control volume which is indicated by the dashed line on Figure 10, and which coincides with the dispenser free volume. For this control volume the energy equation is

$$\frac{dE_F}{dt} = \dot{m}_i(e_i + u_i^2/2) + \dot{m}_i P_i v_i - P_p u_p A_p \tag{9}$$

where E_F is the total instantaneous energy content in the free volume, and $\dot{m}_i$, e_i, u_i, P_i, and v_i refer respectively to the mass flow rate, specific internal energy, gas velocity, pressure, and specific volume at the free volume inlet. Writing $E_F = m_F e_F$ and noting that from conservation of mass $dm_F/dt = \dot{m}_i$, then for a thermally and calorically perfect gas, Equation (9) can be reduced to

$$\frac{dT_F}{dt} = \frac{\dot{m}_i}{m_F}(\gamma T_C - T_F) - (\gamma - 1)\frac{u_p A_p T_F}{V_F} \quad , \tag{10}$$

where γ is the specific heats ratio of the gas. In simplifying Equation (9), quasi-steady gas flow from the gas supply pressure vessel to the free volume inlet was assumed, so that the steady state energy equation between those points, $h_c = h_i + u_i^2/2$, could be used (h is enthalpy). The relation between P_F and T_F is then simply

$$P_F = \frac{m_F R T_F}{V_F} \quad , \tag{11}$$

where R is the specific gas constant. Also, the equation for free volume expansion is

$$\frac{dV_F}{dt} = u_p A_p \quad . \tag{12}$$

To complete this set of equations, the rate of mass flow into the free volume, $\dot{m}_i$, is needed. From mass conservation, $\dot{m}_i = \dot{m}_o$, where $\dot{m}_o$ is the flow rate through the orifice. If the orifice is not exactly at the free volume inlet, flow through it will be choked when $P_F \leq P_{BC}$, where the back pressure for incipient choking in this case is

$$P_{BC} = P_C \left(1 + \frac{\gamma-1}{2} M_{ic}^2 \right)^{-\frac{\gamma}{\gamma-1}} \quad , \tag{13}$$

and the Mach number at the inlet corresponding to choked orifice flow is M_{ic}, determined from

$$\frac{A_i}{A_o} = \frac{1}{M_{ic}} \left[\left(\frac{2}{\gamma+1} \right) \left(1 + \frac{\gamma-1}{2} M_{ic}^2 \right) \right]^{\frac{\gamma+1}{2(\gamma-1)}} \quad .$$

Therefore, when $P_F \leq P_{BC}$,

$$\dot{m}_i = \dot{m}_o = P_c A_o \sqrt{\frac{\gamma}{RT_c}} \left(\frac{2}{\gamma+1}\right)^{\frac{\gamma+1}{2(\gamma-1)}} \quad . \tag{14}$$

On the other hand, if $P_{BC} < P_F \leq P_c$, the orifice is not choked. In this latter case, the Mach number at the free volume inlet is

$$M_i = \sqrt{\left(\frac{2}{\gamma-1}\right)\left[\left(\frac{P_c}{P_F}\right)^{\frac{\gamma-1}{\gamma}} - 1\right]} \tag{15}$$

and the inlet mass flow rate is

$$\dot{m}_i = P_c A_i M_i \sqrt{\frac{\gamma}{RT_c}} \left(1 + \frac{\gamma-1}{2} M_i^2\right)^{-\frac{\gamma+1}{2(\gamma-1)}} \quad . \tag{16}$$

This group of equations was numerically integrated for a variety of possible conditions. In all cases, the initial piston velocity, $u_p(0)$ was zero, $P_F(0) = P_\ell(0) = P_A = 1$ atm, and $T_F = 20°C$ (68°F). The gas initially in the free volume was assumed for convenience to be the same as the driver gas. The initial mass in the free volume was calculated from Equation (11). Required input to the calculation was the initial liquid and free volumes, $V_\ell(0)$ and $V_F(0)$ (or V_T); the gas supply pressure, temperature, and thermal properties, P_c, T_c, γ, and R; the fluid density, ρ_ℓ; the piston, nozzle, orifice and free volume inlet cross-sectional areas, A_p, A_N, A_o, and A_i; and the piston mass. The last of these was estimated from $m_p = \rho_p V_p$ in which ρ_p represents a bulk mass density of the piston. The piston volume was calculated as before by assuming that the piston length-to-diameter ratio is two. A suitable value for ρ_p, based on a previously built dispenser piston, is $\rho_p = 1150$ kg/m^3 (71.9 lbm/ft^3).

In the calculations, it was assumed that the steel explosion vessel would be used as the gas supply container. The largest existing outlet port on this vessel is 8.75 cm (3.44 in) in

diameter. This size was used in most of the calculations as the orifice diameter. The connecting pipe between the pressure vessel and the dispenser cylinder inlet was assumed to be 3-inch double-extra-strong steel pipe, which has an inside diameter of 17.5 cm (6.87 in). This diameter was used to calculate the cylinder inlet area, A_1.

Figures 11 through 14 illustrate the computed dispenser dynamics for the case of a 0.102 m (4 in) diameter nozzle and a 0.356 m (14 in.) diameter piston, with $V(0) = 1/3\ V_T$ (all calculations assume $V_T = 0.42\ m^3$ (110 gal)). The gas supply in this case was ethylene/air combustion products at $P_c = 16.1$ MPa (2335 psi), $T_c = 2876°K$ (5177°R), and with $\gamma = 1.184$ and $W = 28.4$ (molecular weight).

Gas flow from the supply vessel into the dispenser free volume causes the free volume pressure P_F to begin rising at once. The piston and the fluid ahead of it begin to accelerate, and this acceleration initially increases with time. While liquid is being discharged from the dispenser, the dispensing (or fluid) pressure P_f begins to rise. As this takes place the piston acceleration steadily diminishes. The piston velocity continues to increase, however, as P_f approaches but does not exactly reach P_F. During this period, gas flow into the dispenser more than compensates for free volume expansion, so that P_F steadily increases. This process continues until the gas flow to the dispenser ceases to be choked. Then the inlet mass flow rate drops substantially and equilibrium operation is soon after established with $P_f = P_F =$ constant and $u_p =$ constant until all fluid has been dispensed. The value of P_f at this time is only slightly below the supply pressure. Note that the temperature in the free volume eventually increases above that in the supply vessel, due to flow work. The increase is not, however, as great as that which would occur in the absence of free volume expansion. (The free volume temperature is of significance to the selection of piston seals.)

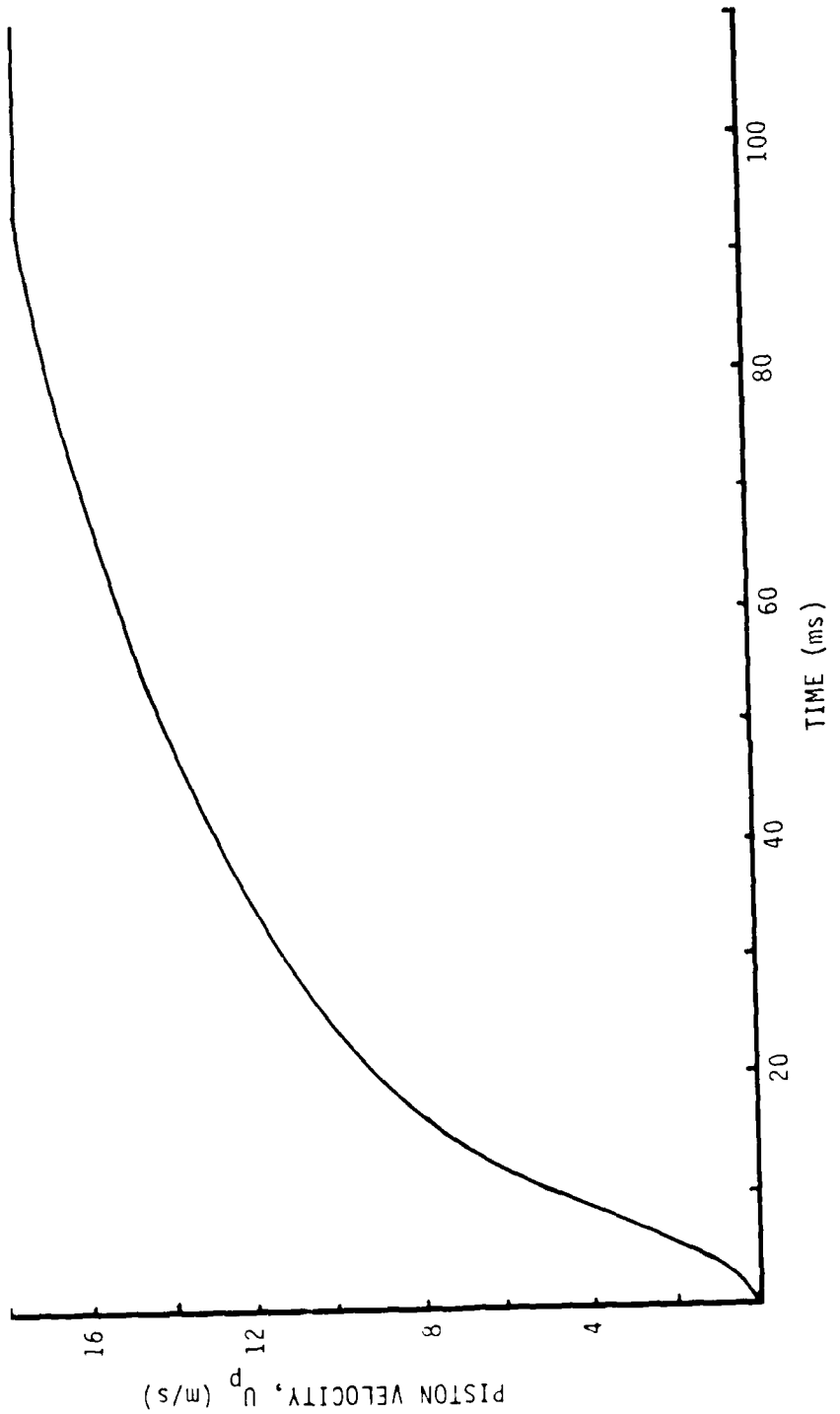

Figure 11. Dispenser piston velocity versus time (see text for conditions).

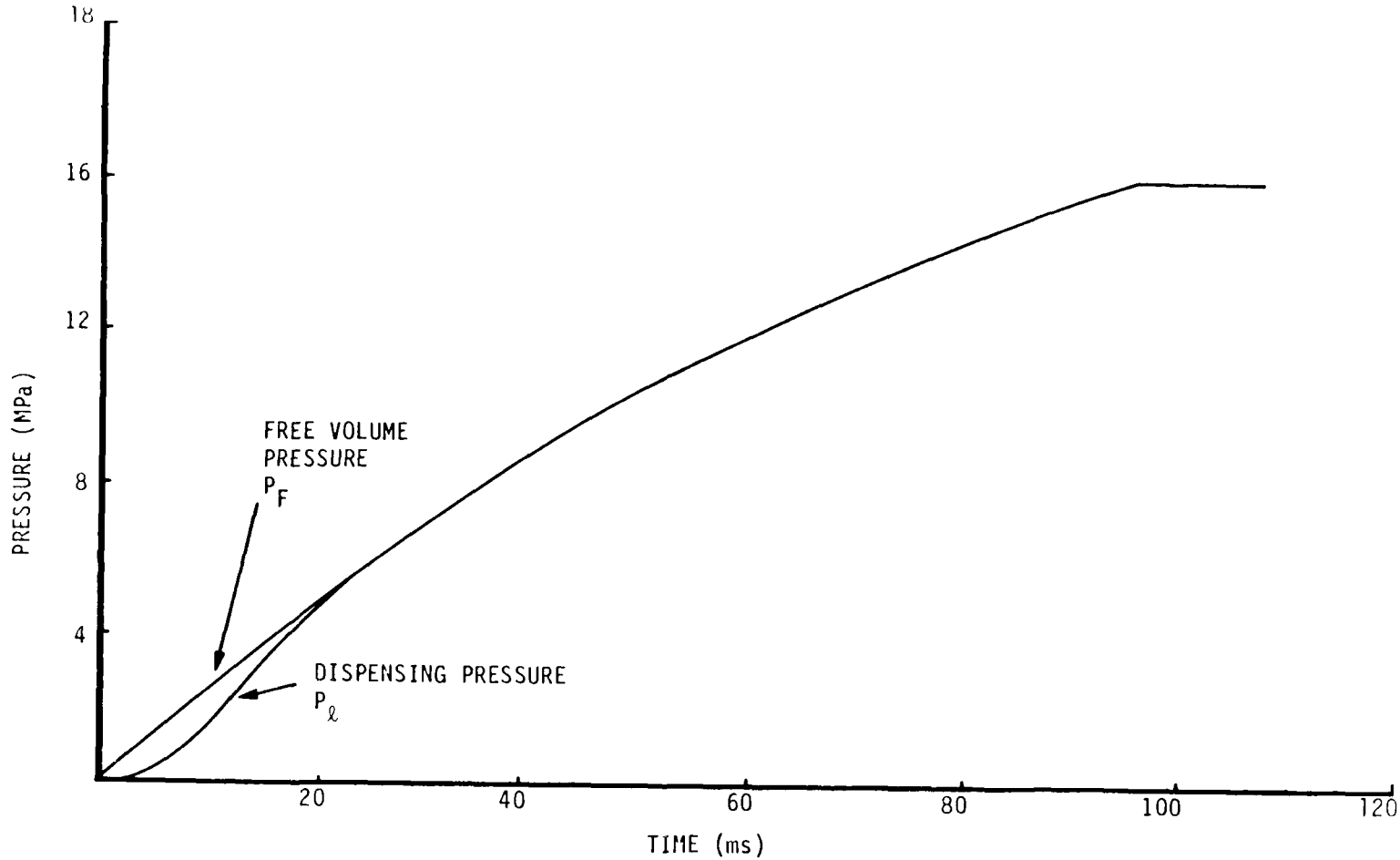

Figure 12. Free volume pressure P_F, and dispensing pressure P_ℓ versus time (see text for conditions).

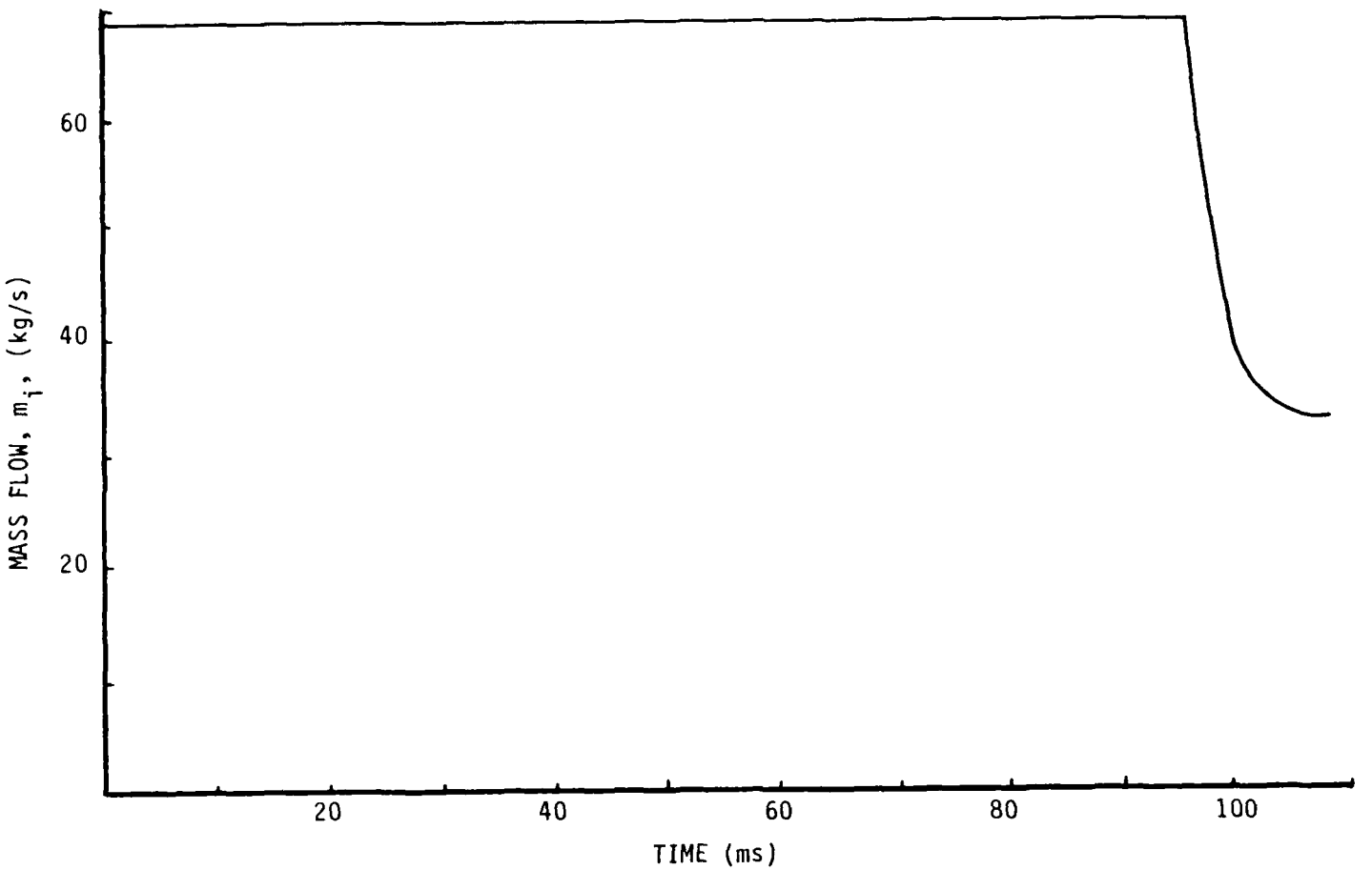

Figure 13. Flow rate of driver gas into free volume versus time (see text for conditions).

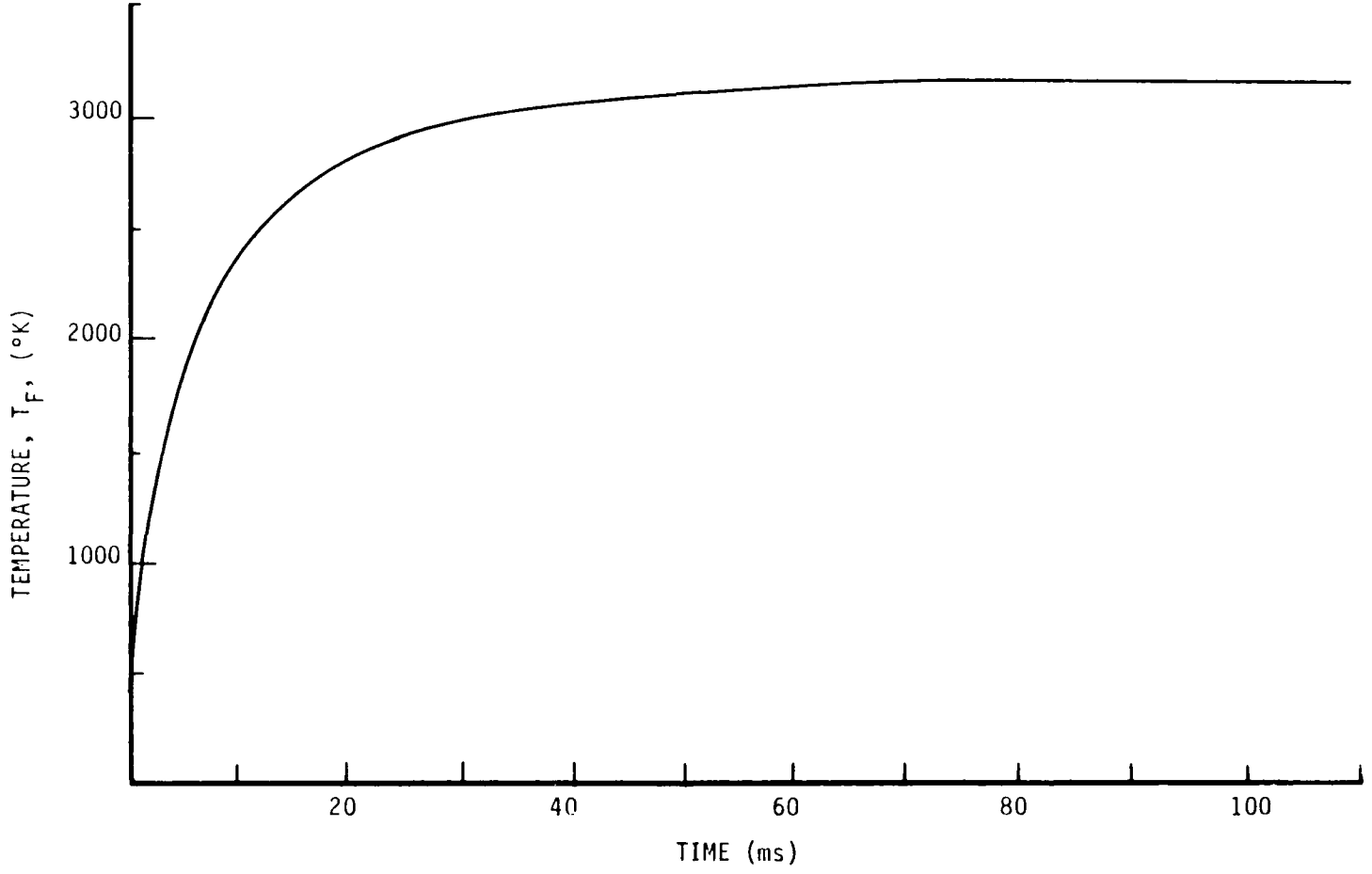

Figure 14. Free volume gas temperature versus time (see text for conditions).

while Figures 11 through 14 illustrate the dispenser dynamics clearly, the example itself is one of very poor dispenser performance. The acceleration or startup time t_{AC}, defined here as the time preceding constant-pressure dispensing, is in this case nearly 90 percent of the total dispensing time, t_D. This poor performance is the combined result of a large-diameter nozzle, a relatively small orifice, and a large initial free volume.

As the initial free volume is reduced, startup performance of the dispenser rapidly improves. The time for the free volume to be filled with supply gas decreases while the total dispensing time increases. In Figure 15, startup time is plotted as a function of the quantity of liquid dispensed (see Equation (7)). All conditions other than $V_\ell(0)$ are the same as in the previous example. When the dispenser is loaded to near full liquid capacity, the startup time is less than 6 percent of the dispensing time, which is considered satisfactory performance. On the other hand, if the load were much less than about 1/3 of full capacity, the dispenser would not reach a constant pressure condition during the entire dispensing period.

Although the dispenser was to be designed for P_ℓ = 14 MPa (2000 psi), $V_\ell(0) = V_T$ = 0.42 m^3 (110 gal), and D_N = 0.1 m (4 in.), it was anticipated that experiments would be necessary with pressures as low as 3.45 MPa (500 psi) and with fuel loads as low as 0.14 m^3 (37 gal) (1/3 capacity). Since dispenser performance would be poorest with 1/3-capacity loads, it was decided to further analyze startup dynamics only for that case, so that the dispenser could then be designed for satisfactory operation under the most difficult conditions.

Table 1 summarizes these calculations. In all cases, the fluid dispensed was assumed to be heptane. The piston mass was estimated as described earlier. The piston, nozzle, orifice, and dispenser inlet diameters, D_p, D_N, D_o, and D_i are listed as are the driver gas pressure and temperature, P_c and T_c, and the driver gas specific heats ratio and molecular weight, γ and W.

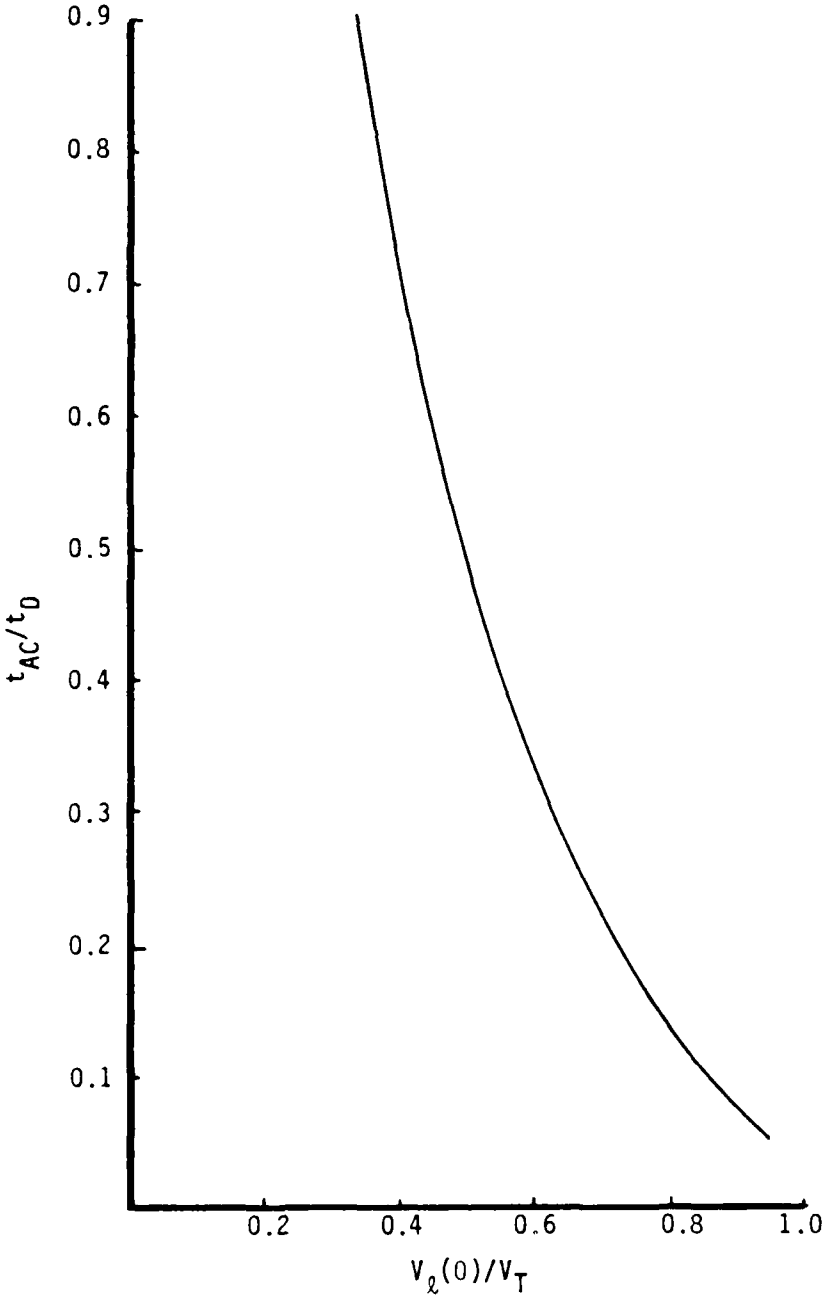

Figure 15. Piston acceleration time versus quantity of liquid dispensed (see text for conditions).

Dispenser performance is characterized principally by the ratio of acceleration (startup) time, t_{AC}, to total dispensing time, t_D, (which is also tabulated separately for reference). In all of the cases listed, with the exception of Case 7, the driver gas assumed was the products of ethylene-air combustion.

Case Number 1 is a reference base. Performance is quite poor, but it is not as bad as in Case 2, which was the example discussed earlier (Figures 11 through 14). The difference between these two cases is the nozzle diameter, which is 7.6 cm (3 in.) in Case 1 and 10 cm (4 in.) in Case 2.

Increasing the piston diameter from 36 cm (14 in.) to 41 cm (16 in.) does not improve dispenser performance in this range of conditions, as can be seen by comparing Cases 1 and 3. A 36 cm (14 in.) piston therefore appeared to be the best design choice.

Case 4 demonstrates the relative performance of the dispenser at lower driver pressures. The ratio of startup to dispensing times is considerably reduced, compared with Case 1. Although t_{AC} increases as P_c is reduced, the concomitant increase in t_D is much larger. Consequently, worst-case dispenser performance occurs at the highest driver pressures, contrary to what might be intuitively expected.

On considering these first four cases, it was evident that in order to attain acceptable high-pressure dispenser performance, with less than full fluid capacity, it would be necessary to enlarge the orifice diameter, D_o. As mentioned earlier, the available pressure supply vessel has an existing 8.74 cm (3.44 in.) diameter port. Increasing the size of this port would be possible, but as the modification would represent additional expense and delay, it had been hoped to be able to make use of the existing opening.

In Table 1, Cases 5 through 7, the dispenser performance with an enlarged orifice is indicated. Because of the location of the explosion vessel port, the maximum practical enlargement would

TABLE 1

CONDITIONS FOR DISPENSER PERFORMANCE ANALYSIS, $V_\ell(o)/V_T = 1/3$

Case #	D_p (cm)	D_p (in)	D_N (cm)	D_N (in)	D_o (cm)	D_o (in)	D_i (cm)	D_i (in)	P_c (MPa)	P_c (psi)
1	35.6	14	7.62	3	8.74	3.44	17.5	6.87	16.1	2335
2	35.6	14	10.2	4	8.74	3.44	17.5	6.87	16.1	2335
3	40.6	16	7.62	3	8.74	3.44	17.5	6.87	16.1	2335
4	35.6	14	7.62	3	8.74	3.44	17.5	6.87	3.27	474
5	35.6	14	7.62	3	17.5	6.87	17.5	6.87	16.1	2335
6	35.6	14	7.62	3	17.5	6.87	17.5	6.87	13.4	1937
7	35.6	14	7.62	3	17.5	6.87	17.5	6.87	13.8	2000

Case #	T_c (°C)	T_c (°F)	γ	W	t_D (ms)	t_{AC}/t_D
1	2603	4717	1.184	28.4	166	0.470
2	2603	4717	1.184	28.4	108	0.888
3	2603	4717	1.184	28.4	166	0.470
4	2527	4580	1.172	28.3	344	0.206
5	2603	4717	1.184	28.4	148	0.135
6	2595	4702	1.183	28.4	163	0.123
7	27	80	2.40	28.8	170	0.335

correspond to the inside diameter of standard 8 in. double-extra-strong pipe, that is, 17.5 cm (6.87 in.). As can be seen by comparing cases 5 and 1, such an increase in D_o would greatly enhance dispenser performance. The fractional startup time would be reduced by a factor of about 3.5. This considerable improvement would make dispenser performance acceptable at 1/3 liquid capacity and the highest driver pressure. It is felt that the pressure vessel modification to enlarge the port diameter would be justified.

Cases 6 and 7 compare dispenser performance at approximately equal driver pressure but with different driver gases. In both cases, the enlarged orifice is assumed. Case 6 represents performance with ethylene-air combustion products at P_c = 13 MPa (2000 psi). The conditions in Case 7 are nearly identical, except that the driver gas is compressed air (equilibrated to ambient temperature). The dispenser performance using air as the driver gas is unfortunately quite poor. The performance with combustion products is far superior, due to their elevated temperature. Although the mass flow rate into the dispenser is lower with combustion products than it is with air, the free volume pressure develops much more rapidly (see Equations (11) and (14)). This leads to enhanced piston acceleration and hence a shorter acceleration time. Note that the dispensing times are about the same in these two cases. It is expected that the performance of nitrogen as a driver gas would be almost identical to that of air.

4. FACILITY LAYOUT

One of the principal concerns in the physical layout of the large-capacity dispenser was the ability to successfully photograph the liquid jets. In all previous work the jets had been discharged vertically. Difficulties were encountered in photographing those sections of the jets which extended above the horizon in the camera's field of view. The jets could be made visible on high-speed films only when a special film and lens filter were conjunctively used, and that technique was successful only when the sky was

a deep blue (Reference 2). The same jets were however easily photographed without any unusual procedures when the background was dark green or brown foliage.

As a result of these experiences, it was felt that it would be preferable to dispense the jets horizontally. The dispenser would be oriented so that the fluid would be discharged in a plane parallel to a densely foliated hillside. Horizontal dispensing could be accomplished in two ways. Either the dispenser could itself be mounted horizontally, or the dispenser could be mounted vertically and the jets directed horizontally by means of curved nozzles.

Neither of these options was felt to be entirely satisfactory. To minimize centrifugal effects in curved nozzle flow, a large radius of curvature would be required. This would result in large, bulky nozzles. In addition, the curved nozzles would have to be rigidly supported against the substantial side thrust that would be developed in them. On the other hand, if the dispenser were horizontally oriented, the fluid would have to be initially confined by some form of nozzle cap. This arrangement might prove satisfactory if a cap or diaphragm were used which would definitely have no effect on the jet flow.

It seemed a simpler solution to mount the dispenser at a shallow angle and use straight nozzles, as illustrated by the scale drawing of Figures 16 and 17. At the location of the spherical explosion vessel, it was possible to elevate the dispenser at a 16 degree angle above horizontal. This was determined by laying out ground projections of the jet path and perpendicular camera line of sight, using a transit. A large helium-filled balloon was then raised to represent the tip of a 122 m (400 ft) long jet. This is about 25 percent longer than the greatest actual jet reach expected. When the balloon reached the top of the background hill, as viewed through the camera, its elevation angle with respect to the explosion vessel was found to be 16 degrees.

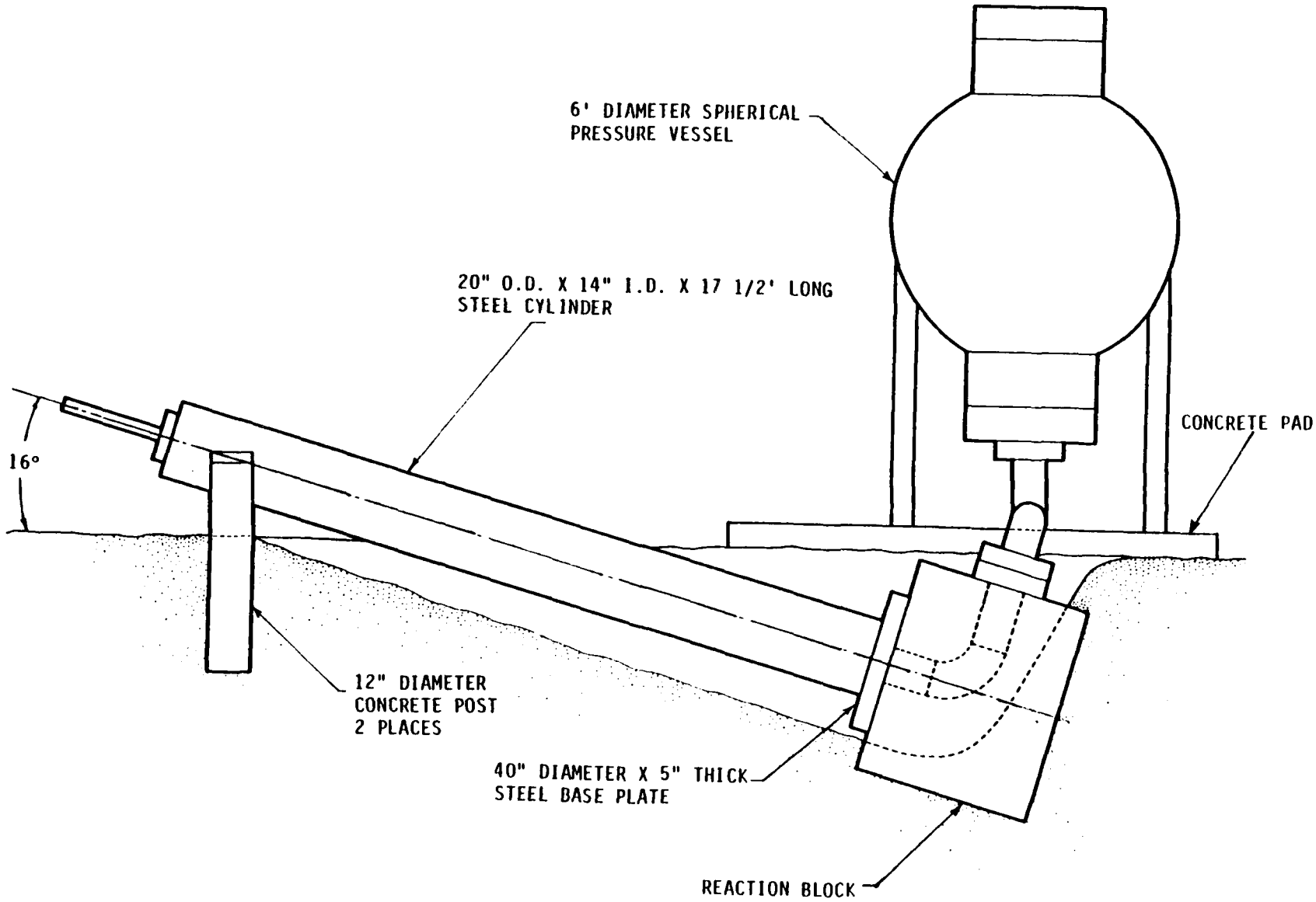

Figure 16. Dispenser system layout elevation.

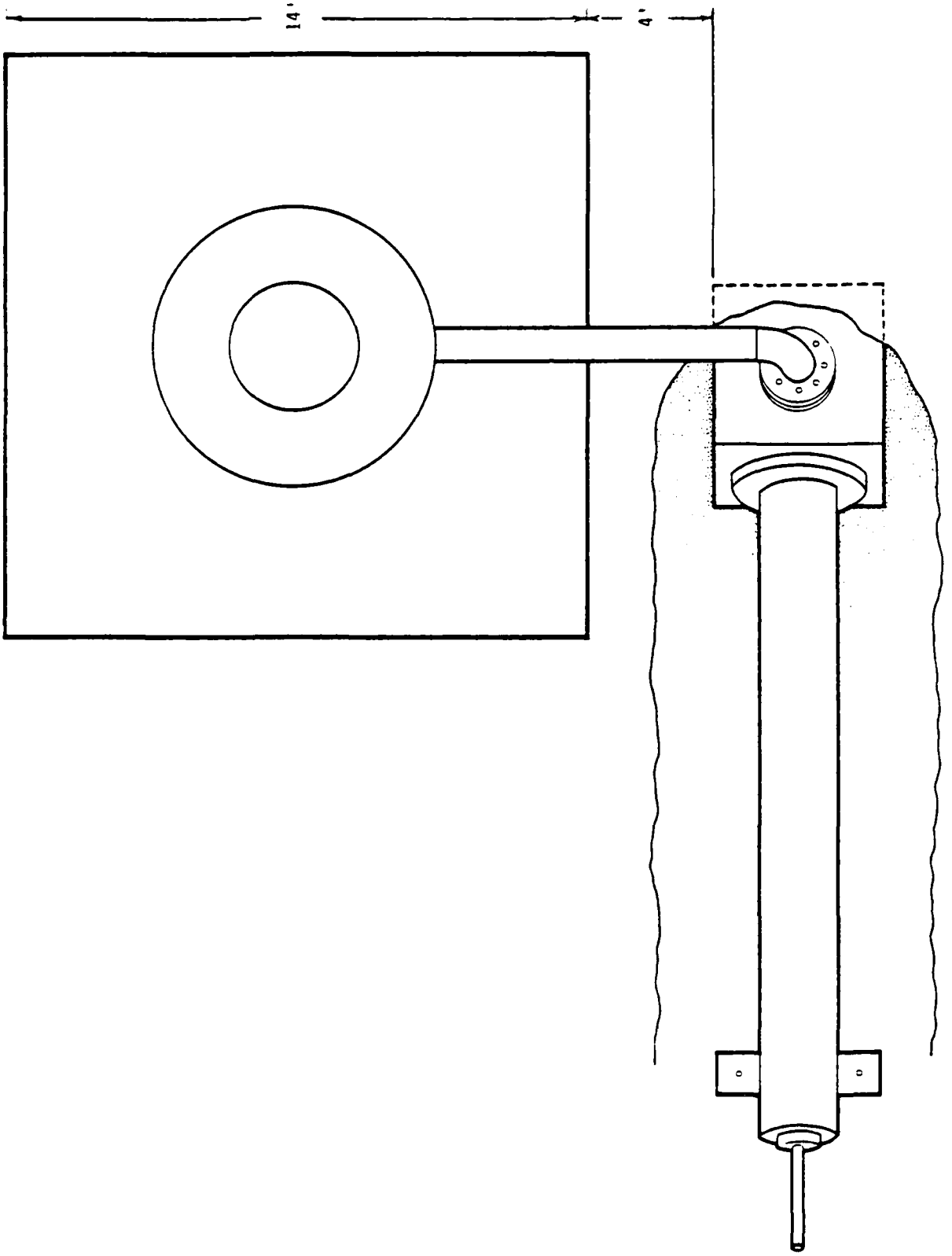

Figure 17. Dispenser system planform.

When oriented at a 16 degree elevation angle, it would be possible to fill the dispenser to capacity without capping the nozzle exit. The straight sections of the discharge nozzles are ten inside diameters in length. For diameters greater than about 3 cm (1.2 in.), the ends of all nozzles would be above the highest point inside the dispenser cylinder.

On the schematic sketches of Figures 16 and 17, the dispenser cylinder is shown installed below grade adjacent to the existing spherical pressure vessel. This arrangement minimizes the above-ground support structure, provides convenient access to the nozzle end of the cylinder, and permits the reaction block to bear against soil. The reaction block design was not completed. However, thrust levels that the block would sustain were calculated. In the most severe case, with P_C = 13.8 MPa (2000 psi) and D_N = 10.2 cm (4 in.), the thrust developed by the dispenser would reach 0.225 MN (5.07×10^4 lb).

An additional concern relating to the dispenser layout was the magnitude of frictional losses in the connecting plumbing between the pressure vessel and the dispenser cylinder. Friction was not considered in the performance analysis described earlier. The configuration shown in Figures 16 and 17 would require a minimum of about 6.1 m (20 ft) of piping including three 90 degree elbows. The largest pipe size that can be mated to the outlet port of the pressure vessel is 8 in. (double-extra-strong), which has an inside diameter of 17.5 cm (6.87 in.). If necessary, the piping could be enlarged a short distance beyond the outlet port to any larger size. However, high pressure pipe is very expensive in large sizes and it was felt that the smallest size that would not significantly affect dispenser performance should be used.

A reasonable value for the friction coefficient of common steel pipe is f = 0.008. In that case, each of the three 90 degree elbows contributes the frictional equivalent of about 30 pipe diameters of length (Reference 3). The total effective length of

the connecting pipe in Figures 16 and 17 is therefore $L_E = L + 90D$, where L is the actual length of straight pipe sections of inside diameter D.

The pressure drop in the connecting pipe can be readily calculated once the Mach number at its entrance (just downstream of the pressure vessel port) is known. This was estimated by ignoring the drop in pressure and temperature within the pressure vessel from stagnation conditions to the pipe entrance. The entrance Mach number is then

$$M_1 = \frac{\dot{m}}{P_c A}\sqrt{\frac{RT_c}{\gamma}} \quad , \tag{17}$$

where $\dot{m}$ is the mass flow through the pipe of area A, P_c and T_c are the driver gas stagnation pressure and temperature, and γ, R are the specific heats ratio and specific gas constant of the driver gas.

Once a value for M_1 was determined, the Mach number M_2 at the end of the connecting pipe (dispenser cylinder inlet) was found from

$$\frac{4fL_E}{D} = \left(\frac{\gamma+1}{2\gamma}\right) \ell n \left[\frac{\left(1 + \frac{\gamma-1}{2} M_2^2\right) M_1^2}{\left(1 + \frac{\gamma-1}{2} M_1^2\right) M_2^2} \right] + \frac{1}{\gamma M_1^2} - \frac{1}{\gamma M_2^2} \quad . \tag{18}$$

Then the piping pressure loss, $\Delta P = P_1 - P_2$, was calculated,

$$\frac{\Delta P}{P_c} = 1 - \frac{M_1}{M_2}\sqrt{\frac{1 + \frac{\gamma-1}{2} M_1^2}{1 + \frac{\gamma-1}{2} M_2^2}} \quad , \tag{19}$$

where P_1 and P_2 are the piping entrance and exit pressures, and $P_1 \doteq P_c$ was assumed.

Representative friction loss calculations were made for dispenser conditions corresponding to Cases 5 and 7 on Table 1.

These two sets of conditions are similar except that in Case 5 the driver gas was ethylene/air combustion products, while in Case 7 the driver gas was ambient temperature air. The mass flow rates used in the calculations were the values associated with the constant-pressure dispensing period. The results are plotted on Figure 18. The fractional pressure drop due to friction would be less than one percent for inside pipe diameters greater than D = 14.2 cm (5.6 in.), if combustion products were used as the driver gas. For equivalent pipe sizes the pressure losses are substantially greater when air is used as driver gas. This is due to the much larger mass flow through the piping when compressed air is used.

5. PISTON BRAKING

With a driver pressure of 16.1 MPa (2335 psi), the steady-state velocity of a 35.6 cm (14 in.) diameter piston dispensing heptane through a 10.1 cm (4 in.) diameter nozzle is about 18 m/s (59 ft/s). If the piston mass were 90 kg (198 lbm), its kinetic energy would be 14.6 kJ (1.07×10^4 ft-lb). In order to minimize the risk of impact damage when the piston completes its travel, some provision to stop the piston in a controlled manner is needed.

The most straightforward braking device for this application is a quill-type shock absorber, which is illustrated schematically on Figure 19. The quill is a projection that attaches to the front of the piston, as shown. As the quill enters the nozzle inlet, fluid is forced by the advancing piston to flow from the reservoir indicated through a continually decreasing minimum area. If the quill length and shape are appropriately designed, the reservoir pressure will rise during this process in such a way that the piston is smoothly decelerated to zero velocity.

During the period of steady-state dispensing, the piston velocity is constant and the pressures acting on it are uniform and equal on both ends. As the quill enters the nozzle inlet, the pressure on the back side of the piston remains uniform and at the

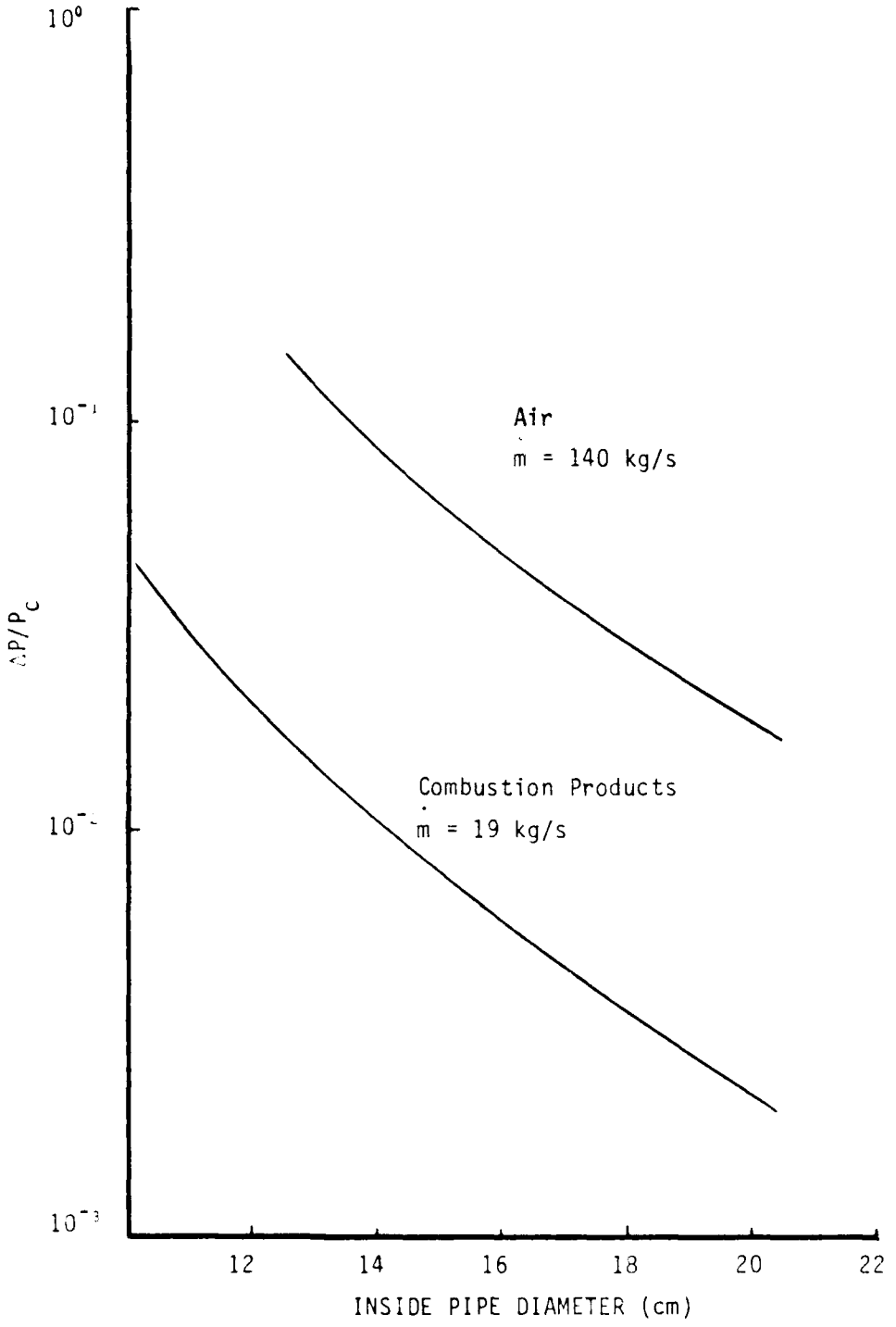

Figure 18. Connecting pipe frictional pressure loss versus pipe diameter (see text for conditions).

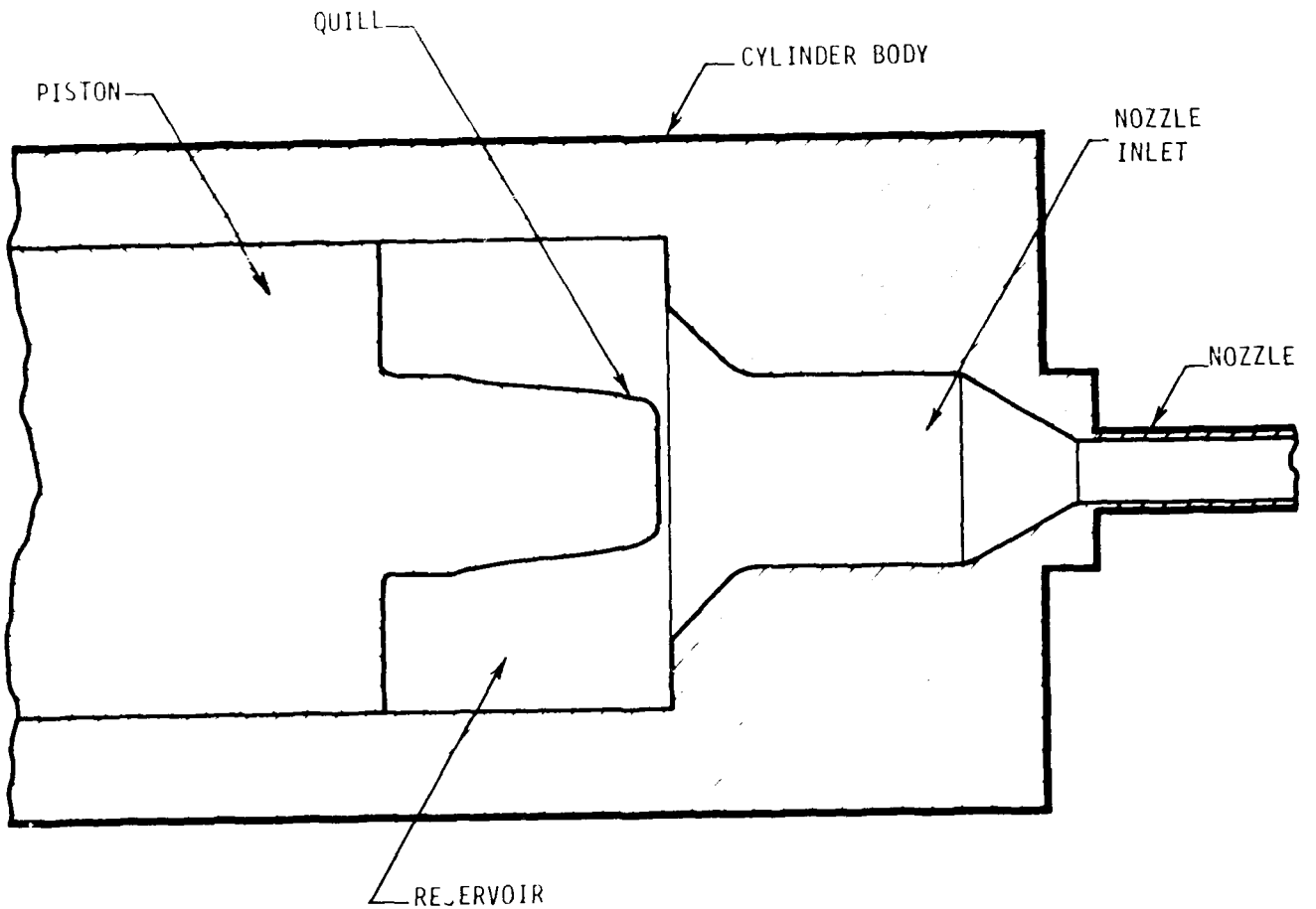

Figure 19. Schematic of quill shock absorber piston braking device.

level P_F (see Figure 10). During this period the pressure in the reservoir, P_R, rises, while the fluid pressure drops off along the quill surface to a value below P_F at its front end. The reduced pressure on the front surface of the quill opposes piston deceleration, so that it is desirable to minimize the area of that surface. In the simplified analysis that follows, the pressure on the entire surface of the quil' was assumed, for purposes of writing the piston equation of motion, to be zero. This assumption was expected to result in calculated reservoir pressures somewhat above those actually needed.

Accordingly, the piston motion during the deceleration period is described by

$$m_p \frac{du_p}{dt} = P_F A_p - P_R A_A \tag{20}$$

and

$$\frac{dx_p}{dt} = u_p \quad , \tag{21}$$

in which A_A is the annular area between the base of the quill and the inside wall of the cylinder body. The time $t = 0$ is defined as the moment of first entry by the quill into the nozzle inlet, which is the condition shown in Figure 19. At this moment the piston position, x_p, is taken to be zero, and the piston velocity is $u_p = u_{p_o}$.

The mode of stopping selected was that of constant deceleration. This would require $P_R(t)$ = constant in Equation 20. In reality, P_R could be constant only after a short initial interval during which it increases from P_F, but this initial interval was ignored. Equation (20) then integrates to

$$u_p = u_{p_o} - Bt \tag{22}$$

where

$$B \equiv \frac{P_R A_A}{m_p} - \frac{P_F A_P}{m_p} \quad . \tag{23}$$

The piston will have stopped ($u_p = 0$) at the time

$$t_E = \frac{u_{p_o}}{B} \quad .$$

From Equations (21) and (22) the piston path is simply

$$x_p = u_{p_o} t - \frac{1}{2} B t^2$$

so that at $t = t_E$, the piston will have moved the distance

$$x_{p_E} = \frac{u_{p_o}^2}{2B} \quad . \tag{24}$$

Now, equating x_{p_E} in Equation (24) to the length of the quill, L_Q, and using Equation (23), leads to the required reservoir pressure,

$$P_R = \frac{m_p u_{p_o}^2}{2 L_Q A_A} + \frac{P_F A_p}{A_A} \quad . \tag{25}$$

The required surface geometry of the quill was established by considering the flow out of the reservoir. It was assumed that the pressure is zero at and downstream of the minimum flow area, A_M, which occurs between the quill and nozzle inlet surfaces. If it is further assumed that the flow is quasi-steady, then the instantaneous mass flow rate is

$$\dot{m}_\ell = A_M \sqrt{2\rho_\ell P_R} \quad . \tag{26}$$

However, if the fluid is considered incompressible, the mass flowing through the minimum area must equal that displaced by the moving piston; that is,

$$\dot{m}_\ell = \rho_\ell u_p A_A \quad . \tag{27}$$

Equating Equations (26) and (27) to solve for A_M, and incorporating Equation (25), gives

$$A_M = \rho_\ell u_p A_A \sqrt{\frac{L_Q A_A}{\rho_\ell (m_p u_{p_o}^2 + 2L_Q P_F A_p)}} \quad . \tag{28}$$

The piston velocity is the only time-dependent variable in Equation (28). It is related to its instantaneous position by

$$\frac{du_p}{dx_p} = \frac{du_p}{dt} \frac{dt}{dx_p} \quad ,$$

or, in view of Equations (20) and (21) ,

$$\frac{du_p}{dx_p} = \frac{P_F A_p - P_R A_A}{m_p u_p} \quad .$$

Upon integrating, and using Equation (25), this becomes

$$u_p = u_{p_o} (1 - x_p/L_Q)^{1/2} \quad . \tag{29}$$

Therefore Equation (28) can be written

$$A_M = \rho_\ell A_A u_{p_o} \left[\frac{L_Q A_A \left(1 - \frac{x_p}{L_Q}\right)}{\rho_\ell (m_p u_{p_o}^2 + 2 L_Q P_F A_p)} \right]^{1/2} \quad . \tag{30}$$

This equation is an explicit relation between the minimum flow area, A_M, and the piston position, x_p, during the constant deceleration process. It is clearly impossible with a single, fixed-surface quill to accomplish uniform stopping under all dispenser operating conditions. The quill was therefore designed to be replaceable.

The calculated variation in A_M with x_p appears in Figure 20 for the following case: L_Q = 0.152 m (6 in.), A_A = 0.0813 m^2 (126 in^2), ρ_ℓ = 683 kg/m^3 (42.7 lbm/ft^3), m_p = 91 kg (200 lbm), u_{p_o} = 18 m/s (59.0 ft/s), A_p = 0.0994 m^2 (154 in^2), and P_F = 13.8 MPa (2000 psi). The areas A_A and A_p correspond to a piston diameter of 35.6 cm (14 in.) and a quill base diameter of 15.2 cm (6 in.). The liquid density is that of heptane. Under these conditions the reservoir pressure, calculated from Equation (25), would be P_R = 18.1 MPa (2620 psi) and the braking time would be t_E = 16.9 ms. The variation in quill radius along its length was determined from the data in Figure 20 by graphical means.

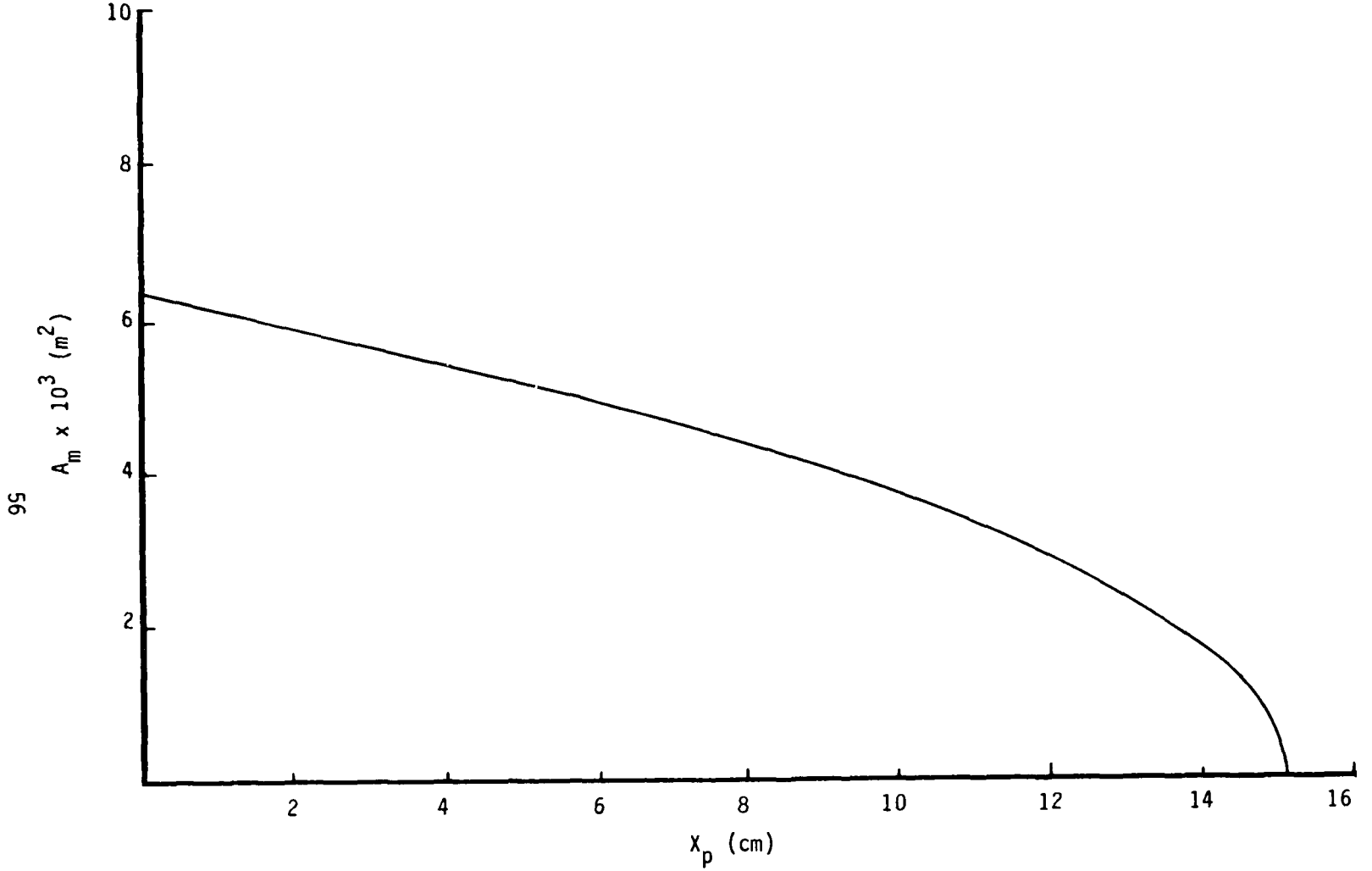

Figure 20. Minimum flow area between quill and nozzle inlet as a function of piston travel during deceleration period (see text for conditions).

III. SECONDARY WAVE SYSTEMS IN FUEL-AIR EXPLOSIONS

One of the issues of FAE/nuclear airblast simulation feasibility that has not been fully resolved is the question of pressure waveform fidelity. By this is meant the degree of temporal correlation between the static pressures produced at equivalent radii in FAE and in scaled nuclear airblasts. Accurate waveform correspondence is considered requisite for meaningful airblast testing of certain targets.

Four types of waveform aberrations are illustrated schematically on Figure 21. Negative curvature in the pressure decay, Figure 21(a), leads to early impulse buildup as compared with positive curvature (shown as a dashed line). The spiked excursion shown in Figure 21(b) would have a slapping effect on a target, but it does not otherwise significantly alter the average pressure profile or waveform impulse. The low-amplitude secondary wave in Figure 21(c) occurs in the negative phase and is not normally considered deleterious. The source of this particular wave is well understood (e.g., see Reference 2).

The fourth type of waveform distortion, represented by Figure 21(d), is presently of greatest concern. Pressure excursions of this type, which occur during the positive phase, consist either of compression wave packets or of shock fronts, followed by relatively slow expansion. These large-amplitude secondary wave systems contribute non-negligible additional overpressure impulse to the blast.

A particularly dramatic example of a large-amplitude secondary wave is given in Figure 22. Secondary waves of this kind have been observed in many of the FAE simulator tests. Most, however, are not of the magnitude in Figure 22, and it has frequently been difficult to distinguish what are thought to be secondary waves from other waveform disturbances.

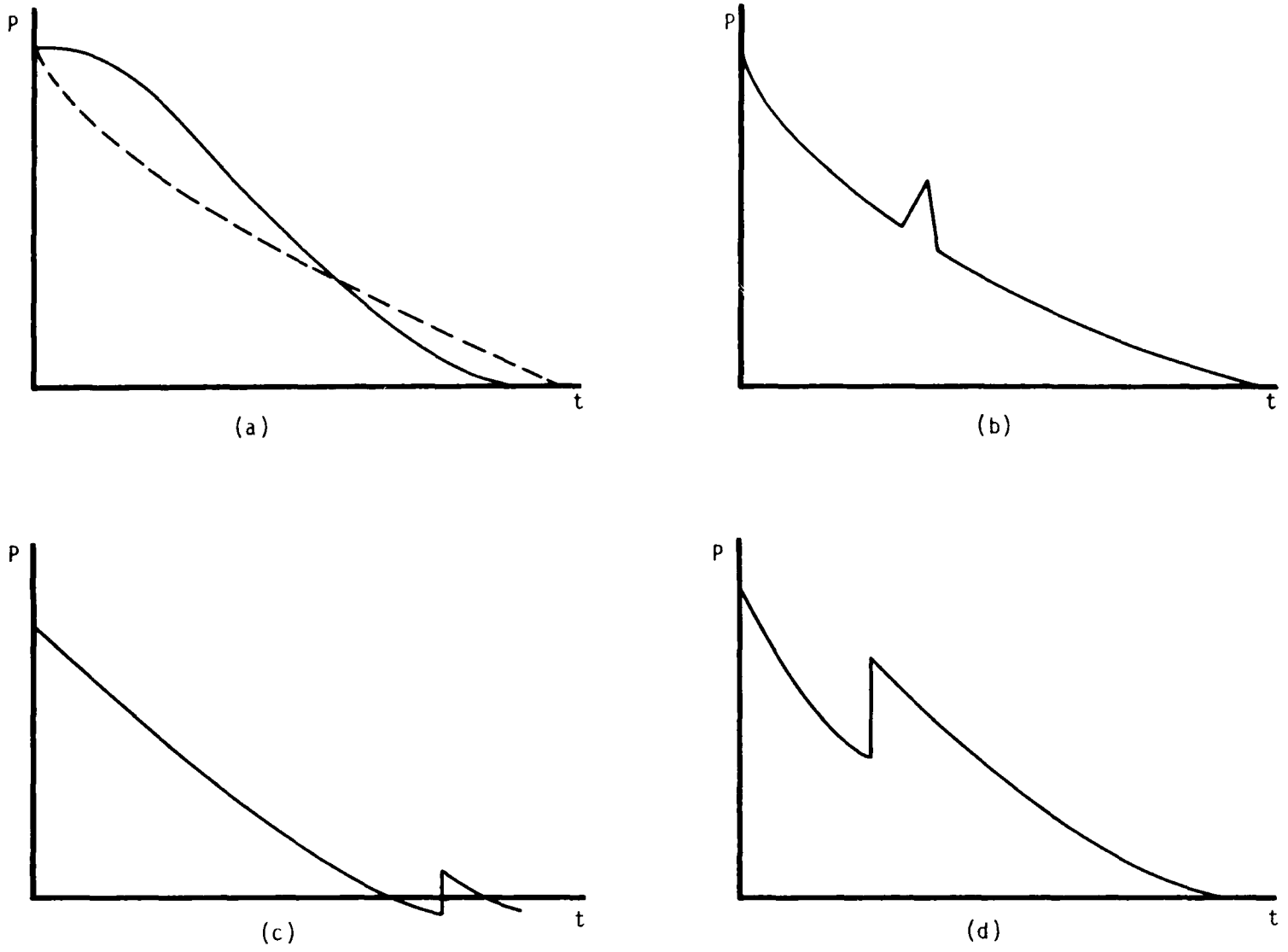

Figure 21. Types of pressure-time waveform aberrations in fuel-air explosions (schematics); (a) negative curvature and inflection (dashed line has positive curvature); (b) impulsive spike; (c) low amplitude secondary wave in negative phase; (d) secondary wave in positive phase with significant added impulse.

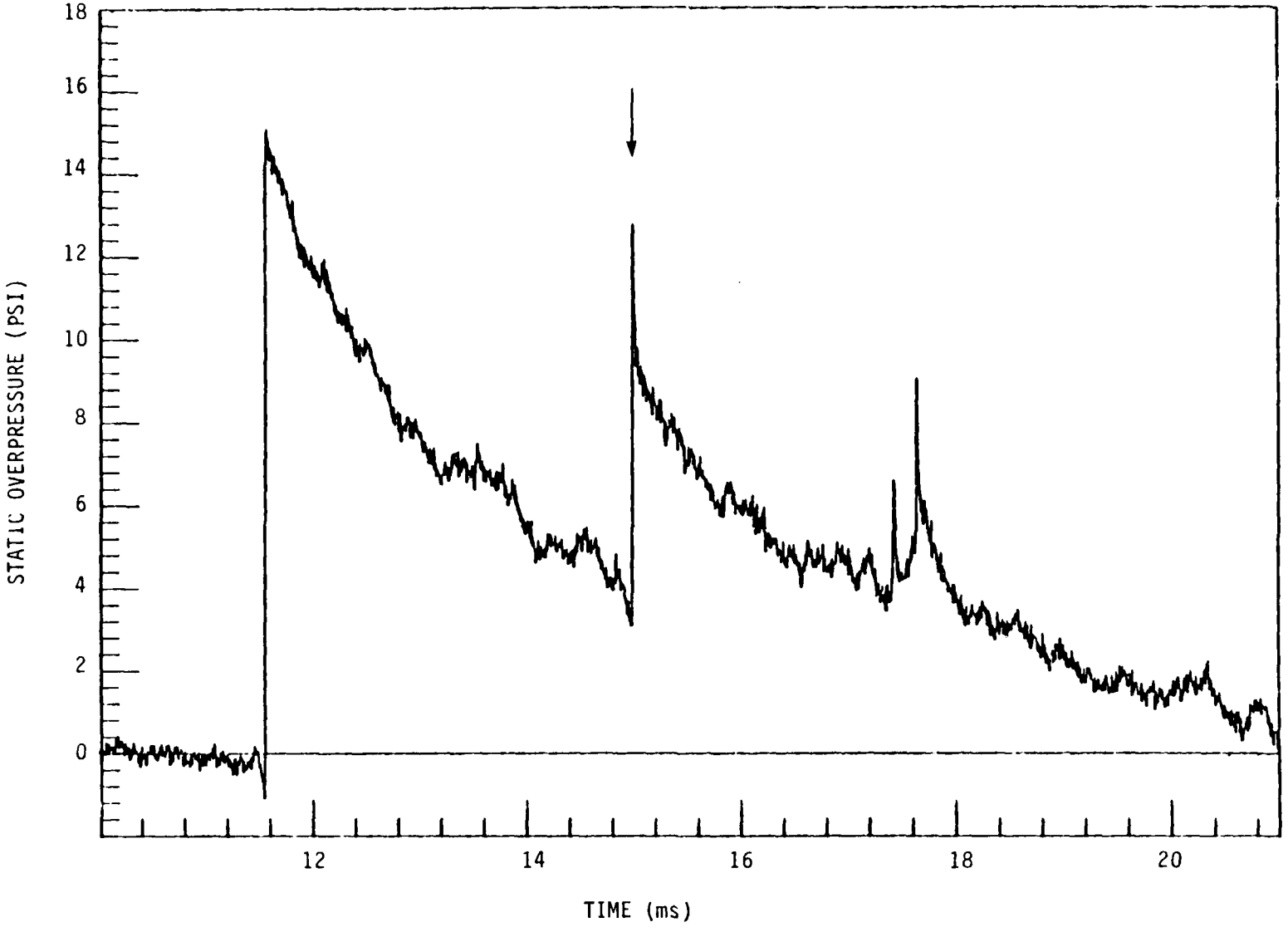

Figure 22. Example of large amplitude secondary wave. Arrow indicates conjectured location of wave front. Data from FAE test CD-14; 22.7 kg (50 lbm) propylene oxide, R = 10.1 m (33.0 ft).

The static pressure records in Figures 23 to 28 are unsmoothed raw data taken from a recent test of the nominal 1/4-tone FAE simulator. In this test it appears that a compression wave packet, originating within the exploded fuel-air cloud, coalesced into a shock while overtaking the blastwave front. An x-t plot of the secondary wave front appears in Figure 28 (what is believed to be the front is indicated by arrows on Figures 23 to 27). A much greater spatial resolution of blastwave pressures is needed in order to identify and trace the progress of secondary waves with greater accuracy. For present purposes, secondary wave fronts have been associated with those points on the pressure records at which abrupt increases in either the average pressure levels or the average values of dP/dt are observed.

The secondary waves appear to be somewhat rotationally asymmetrical. Figure 30 is a pressure record from the same test and approximately the same radial distance as that of Figure 25, but the two pressure transducers were 90 degrees apart. On Figure 30, the front of the secondary wave seems relatively clear, at least as compared with Figure 25. However, when the two pressure records were superimposed, Figure 31, what had appeared to be the respective secondary wave fronts did not align. There does seem to be reasonable rotational symmetry in blastwave time of arrival, peak overpressure, positive phase duration, and impulse development (Figure 32). There also appears to be some degree of pressure-time correspondence over that segment of the secondary wave marked by arrows on Figure 31.

In most cases, static and stagnation pressure records, taken at the same location, are consistent with one another, indicating the arrival and passage of secondary waves at nearly coincident times. An example if Figure 33. However, in some instances, such

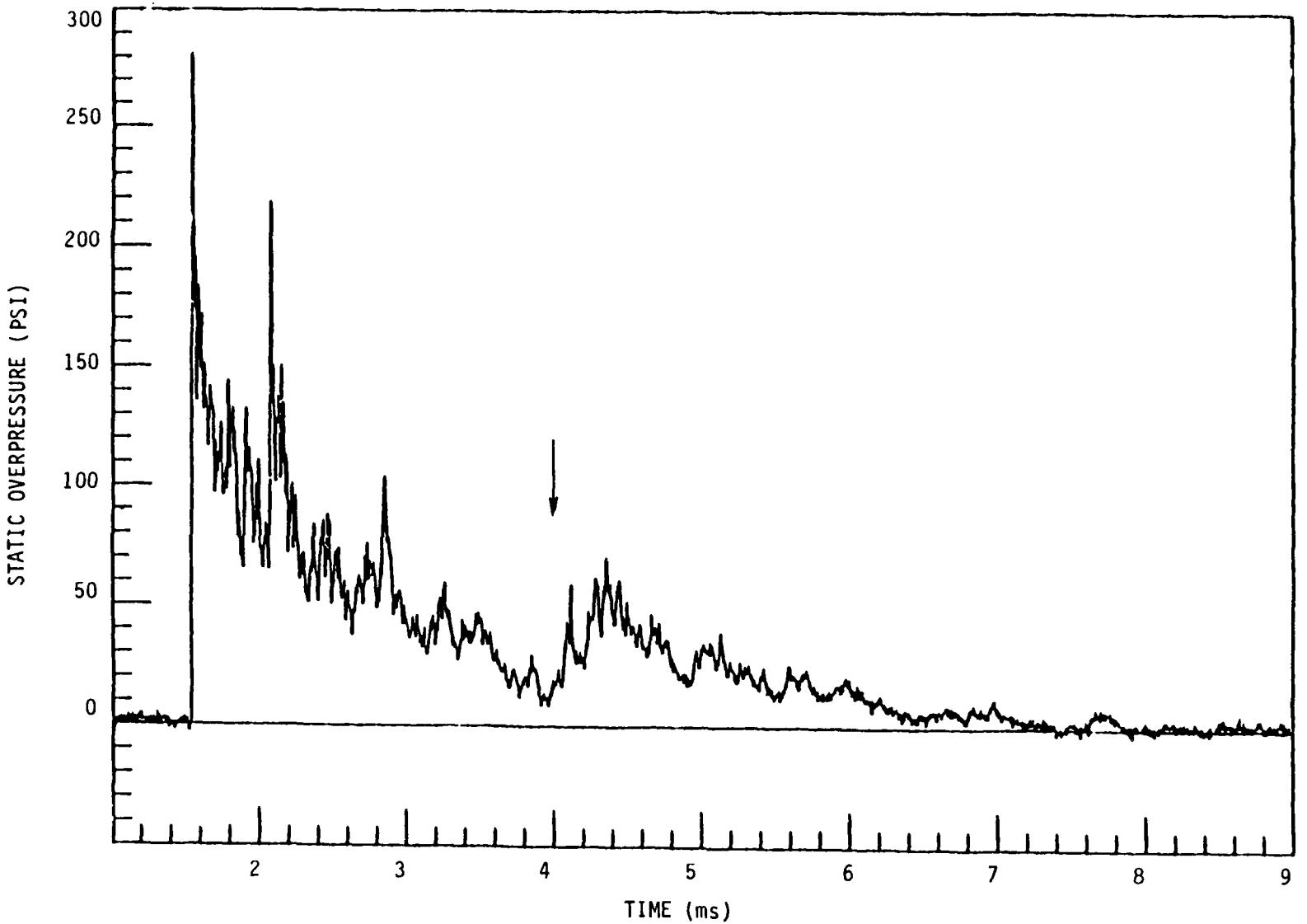

Figure 23. Secondary wave in experimental pressure profile. Arrow indicates approximate location of wave front. Data from FAE test CD-13; 22.7 kg (50 lbm) propylene oxide, R = 2.91 m (9.54 ft).

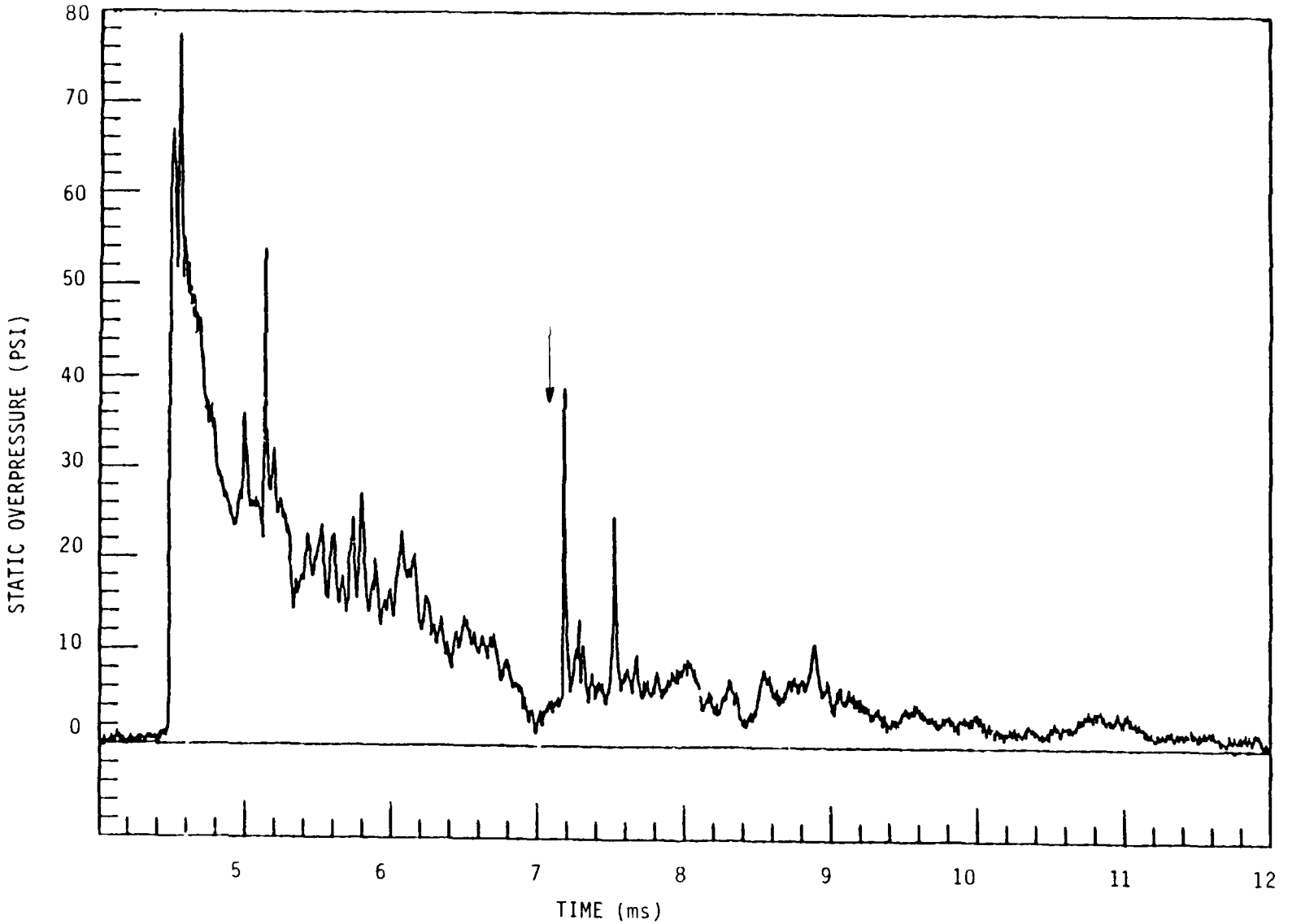

Figure 24. Secondary wave in experimental pressure profile. Arrow indicates approximate location of wave front. Data from FAE test CD-13; 22.7 kg (50 lbm) propylene oxide, R = 5.92 m (19.4 ft).

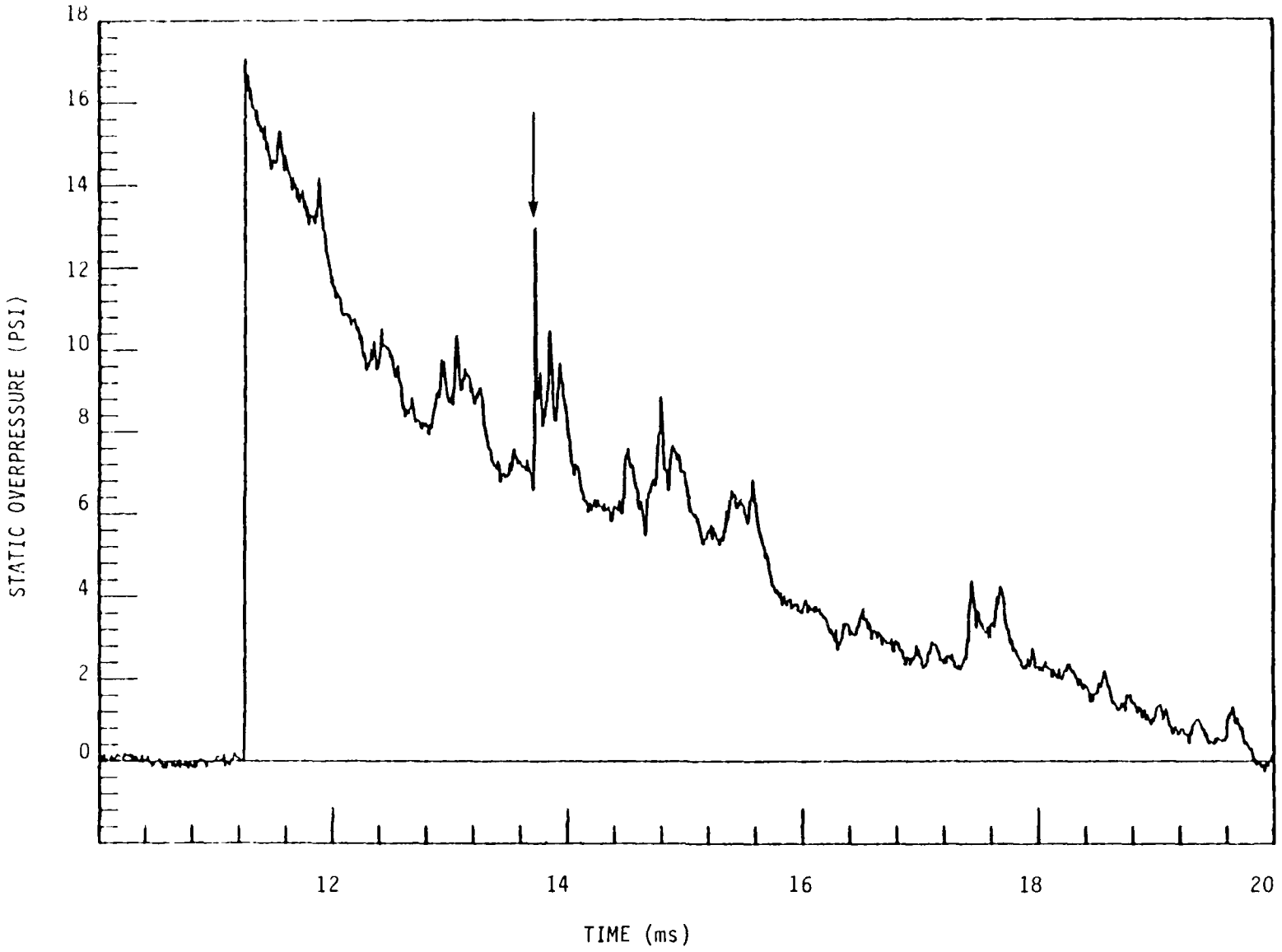

Figure 25. Secondary wave in experimental pressure profile. Arrow indicates approximate location of wave front. Data from FAE test CD-13; 22.7 kg (50 lbm) propylene oxide, R = 9.93 m (32.6 ft).

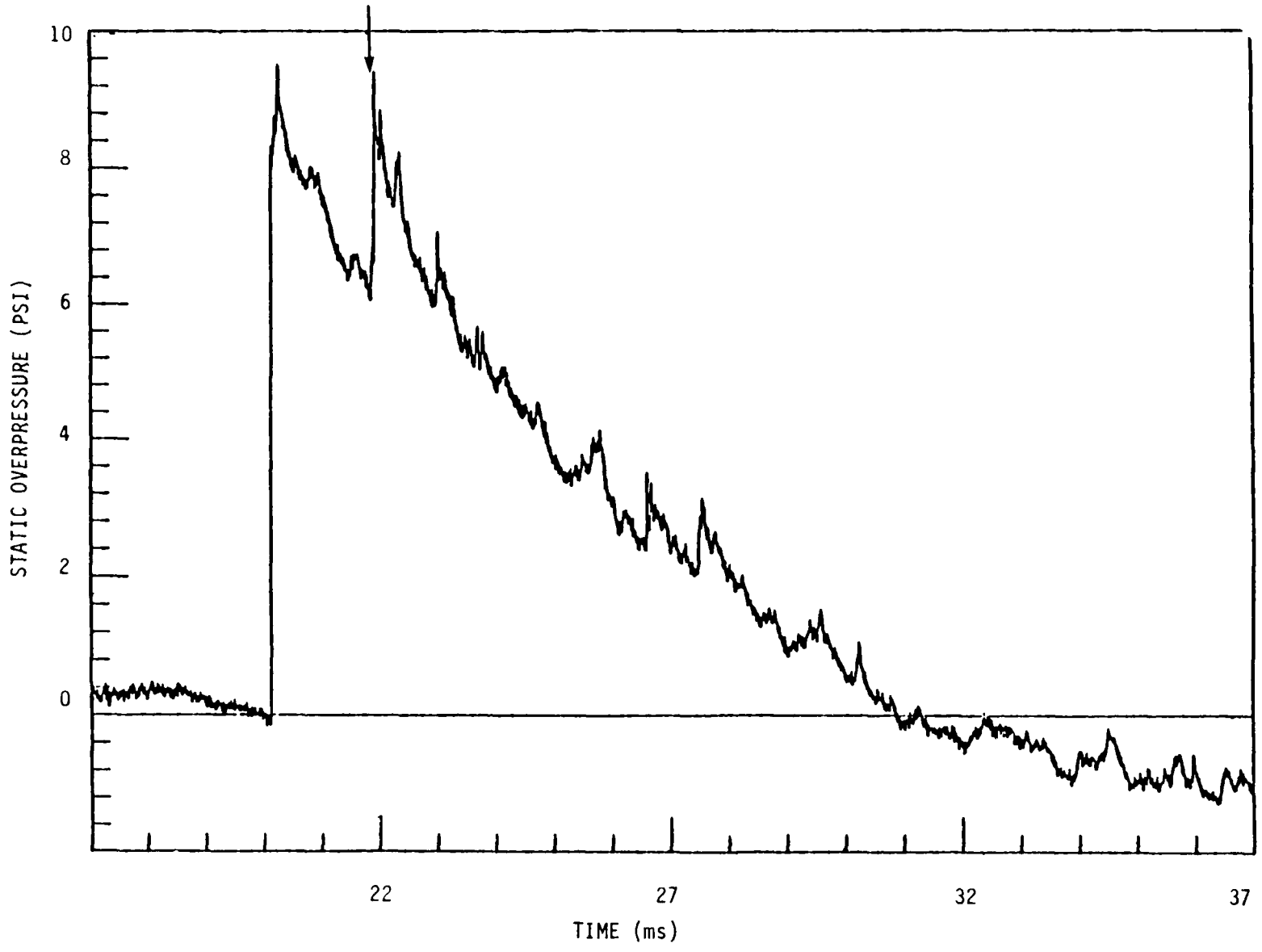

Figure 26. Secondary wave in experimental pressure profile. Arrow indicates approximate location of wave front. Data from FAE test CD-13; 22.7 kg (50 lbm) propylene oxide, R = 13.9 m (45.6 ft).

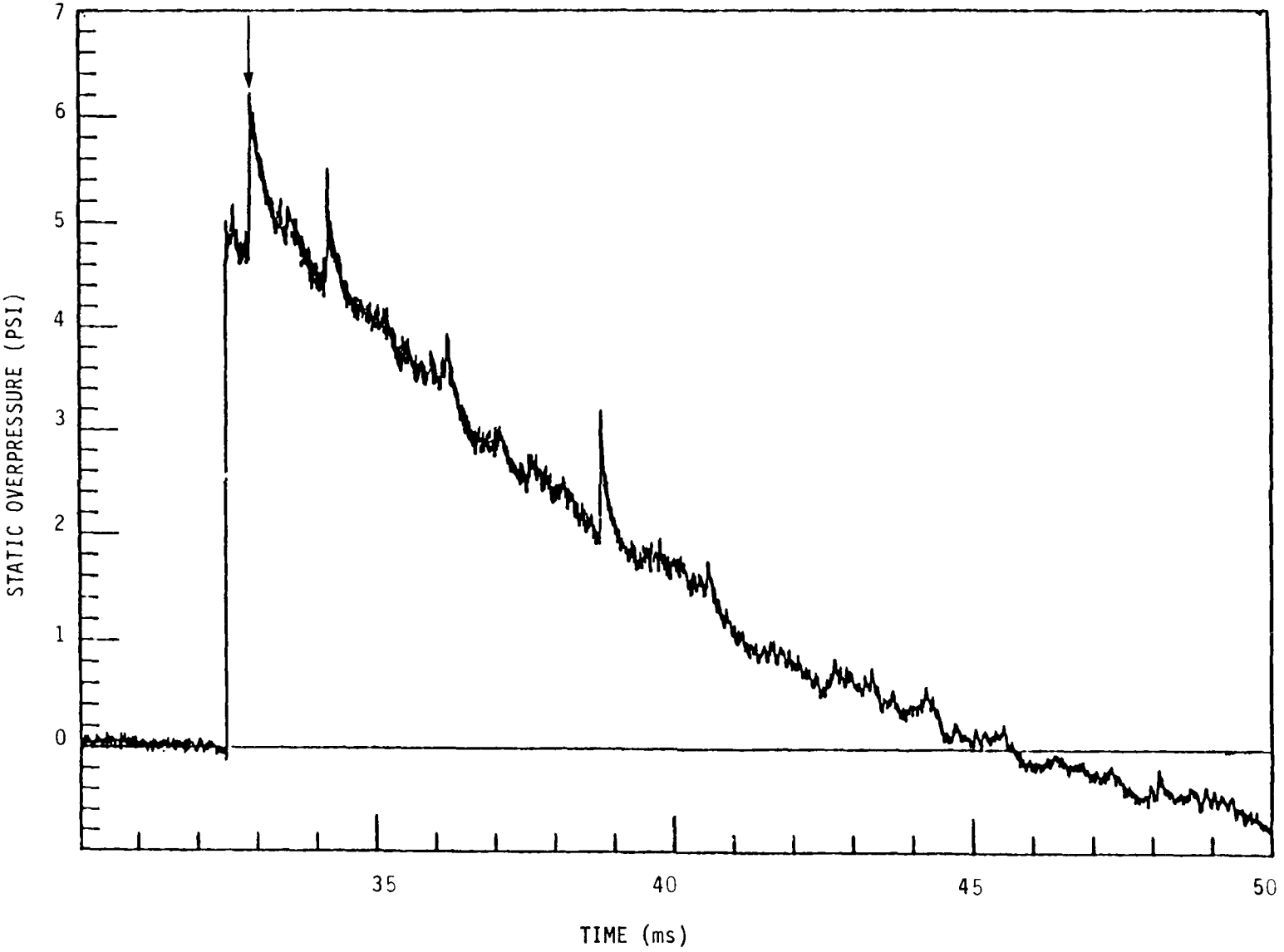

Figure 27. Secondary wave in experimental pressure profile. Arrow indicates approximate location of wave front. Data from FAE test CD-13; 22.7 kg (50 lbm) propylene oxide, R - 18.9 m (62.0 ft).

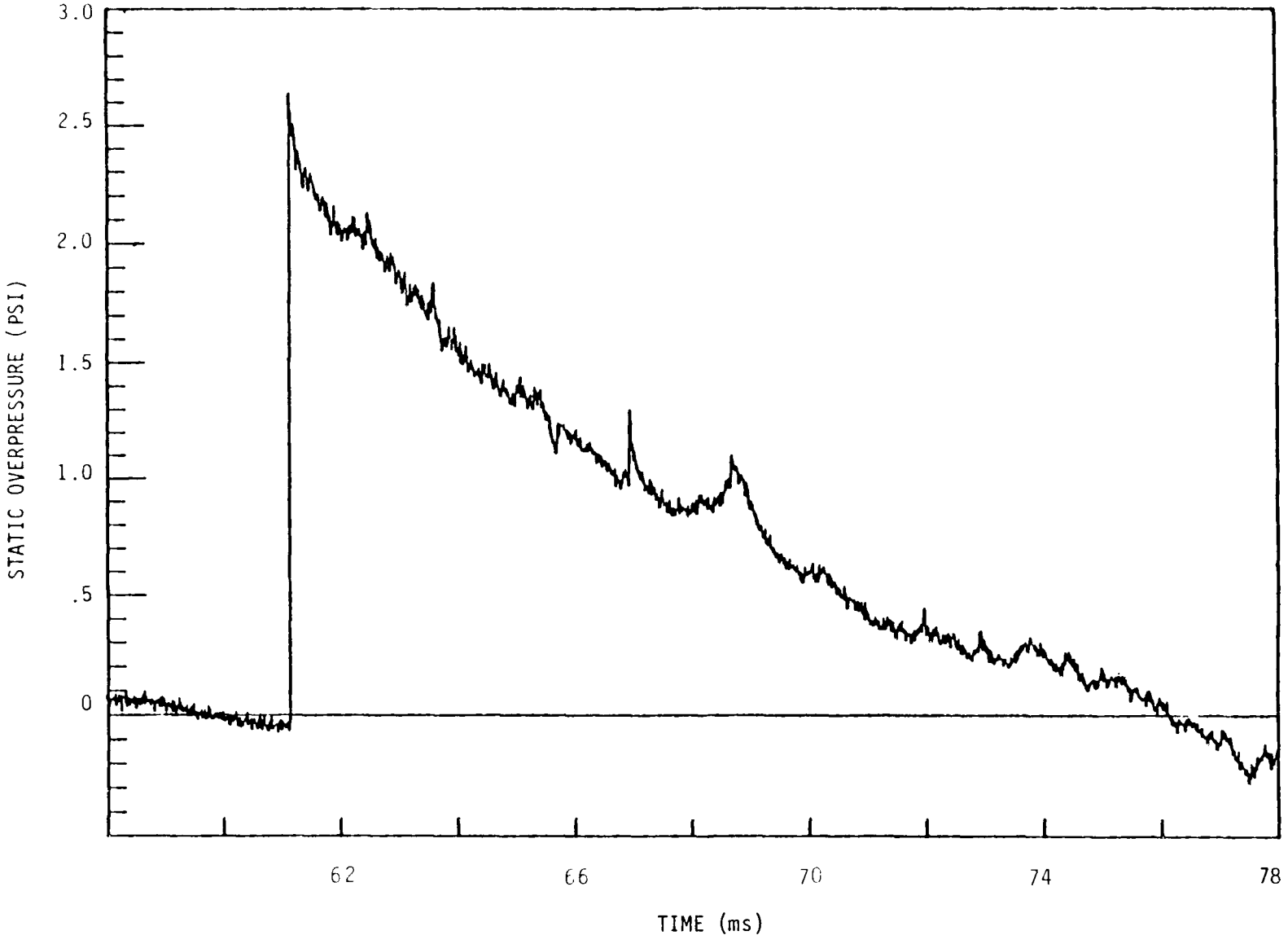

Figure 28. Data from FAE test CD-13 (no secondary wave); 22.7 kg (50 lbm) propylene oxide, R = 29.9 m (98 ft.).

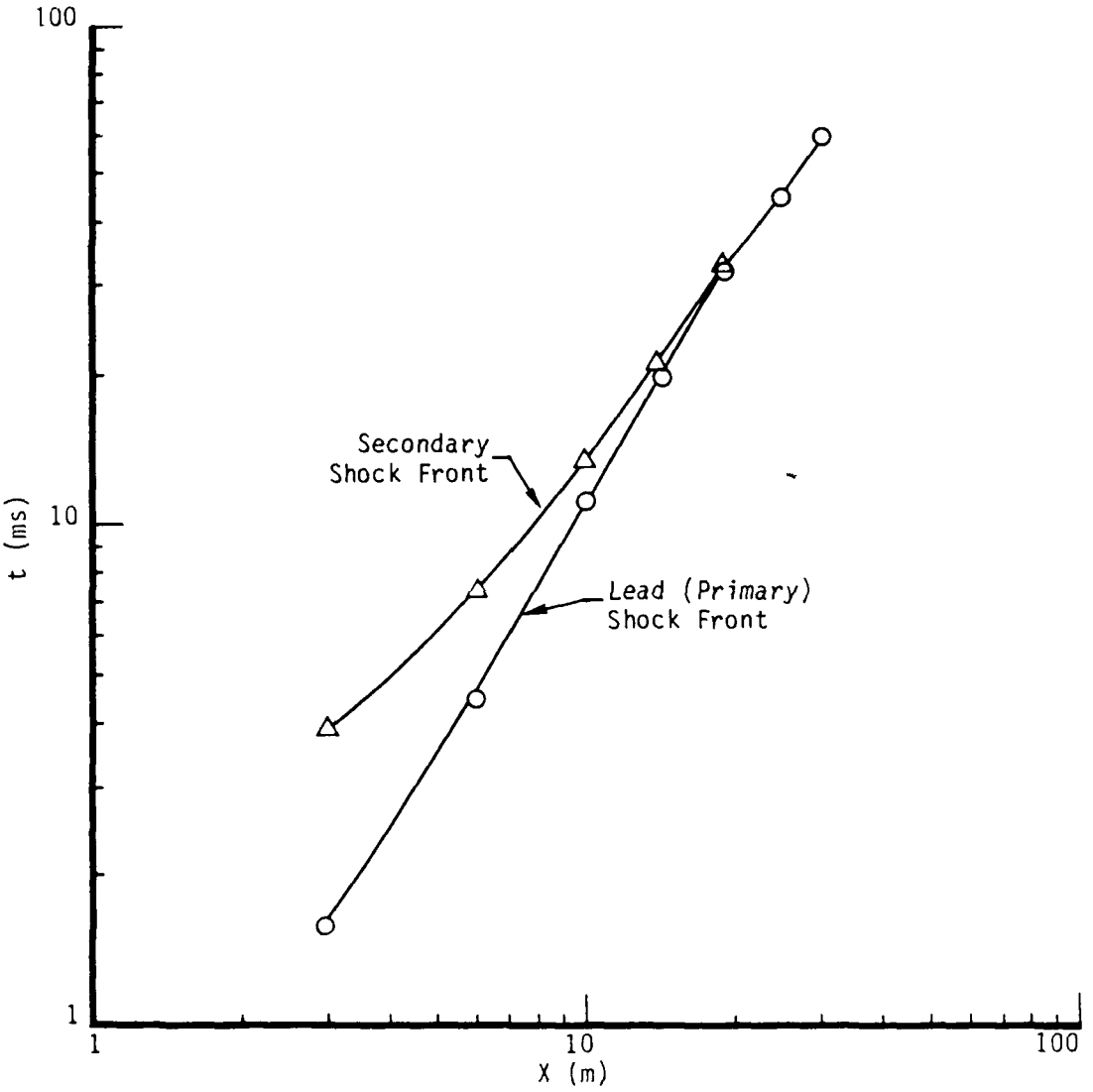

Figure 29. Position versus time (x-t) plot of blastwave lead shock and secondary wave front. Data from FAE test CD-13; 22.7 kg (50 lbm) propylene oxide.

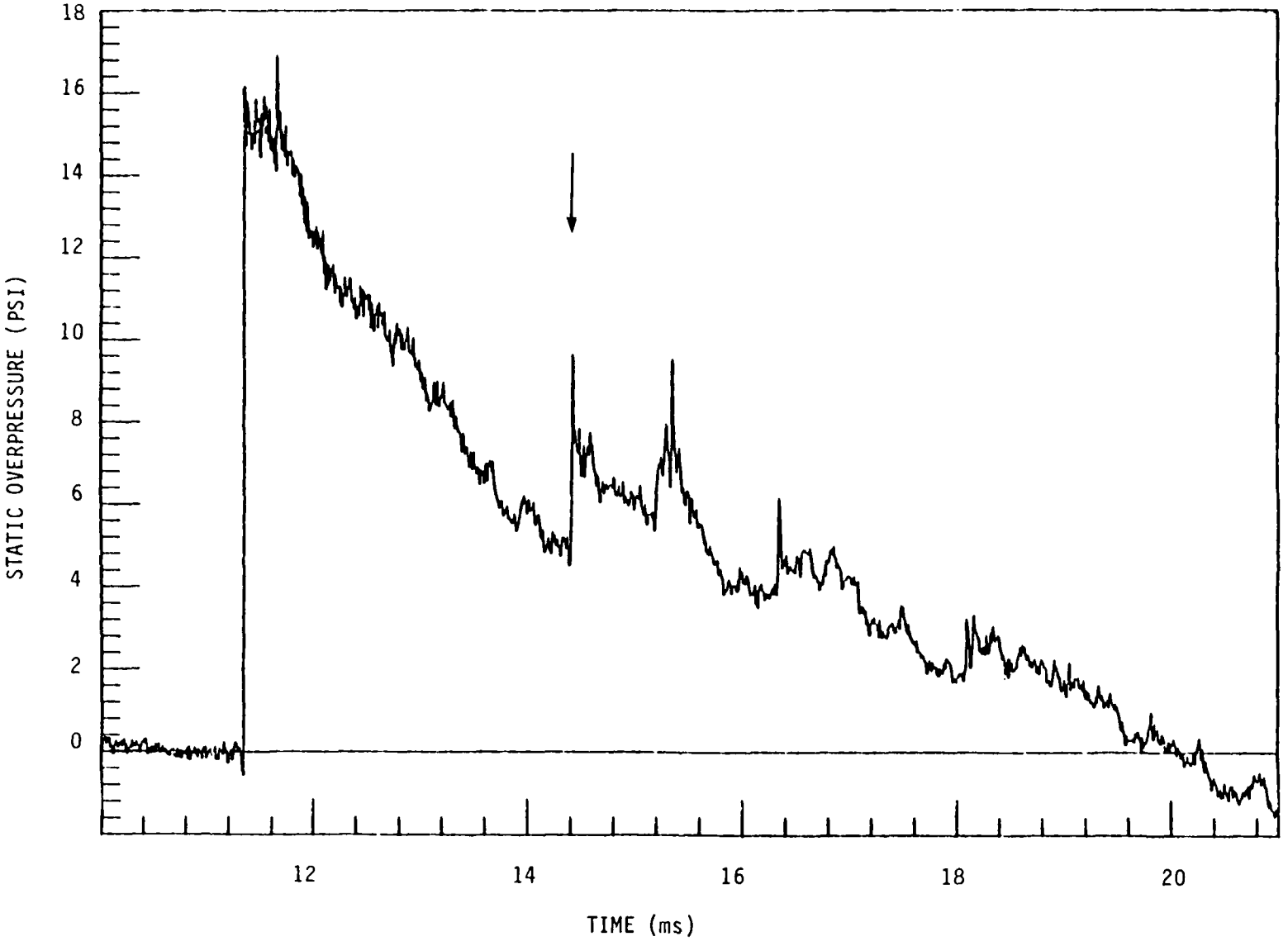

Figure 30. Secondary wave in experimental pressure profile. Arrow indicates conjectured location of wave front. Data from FAE test CD-13; 22.7 kg (50 lbm) propylene oxide, R = 10.1 m (33.0 ft). Transducer located 90° from that of Figure 25.

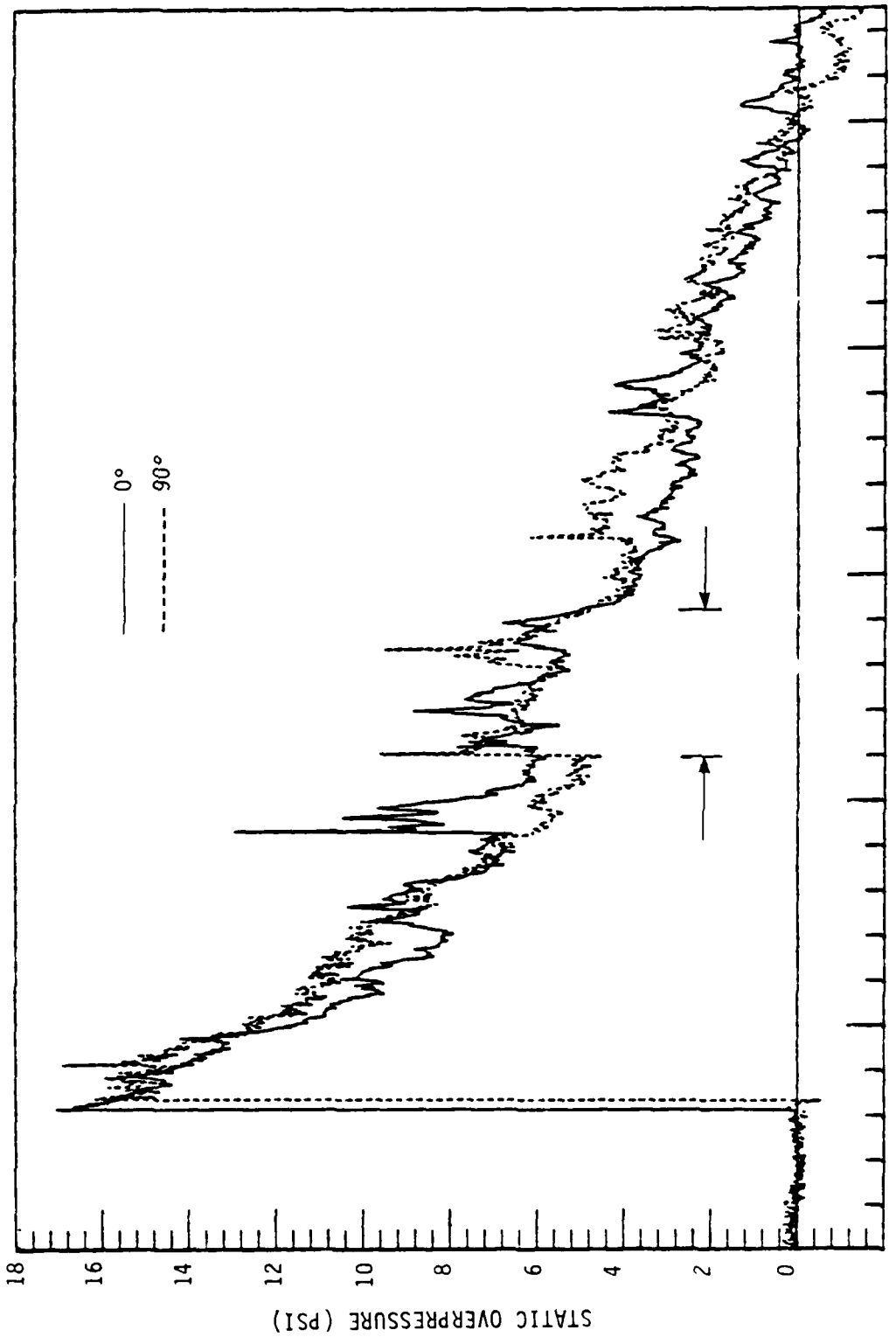

Figure 31. Superposition of Figures 25 and 30. Time referred for both traces to same instant (detonation initiation).

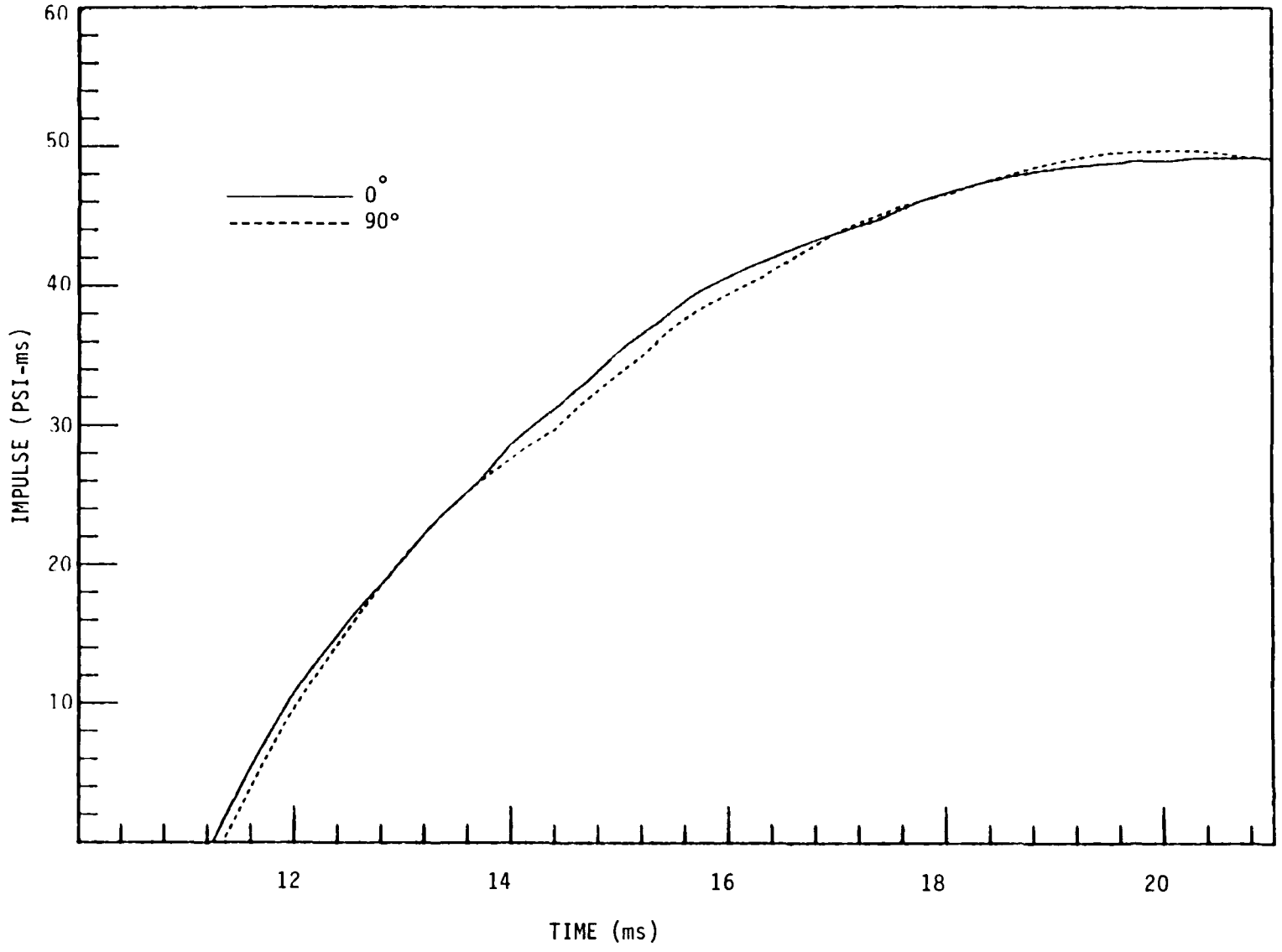

Figure 32. Static overpressure impulse development from pressure traces in Figure 25 (0°) and Figure 30 (90°).

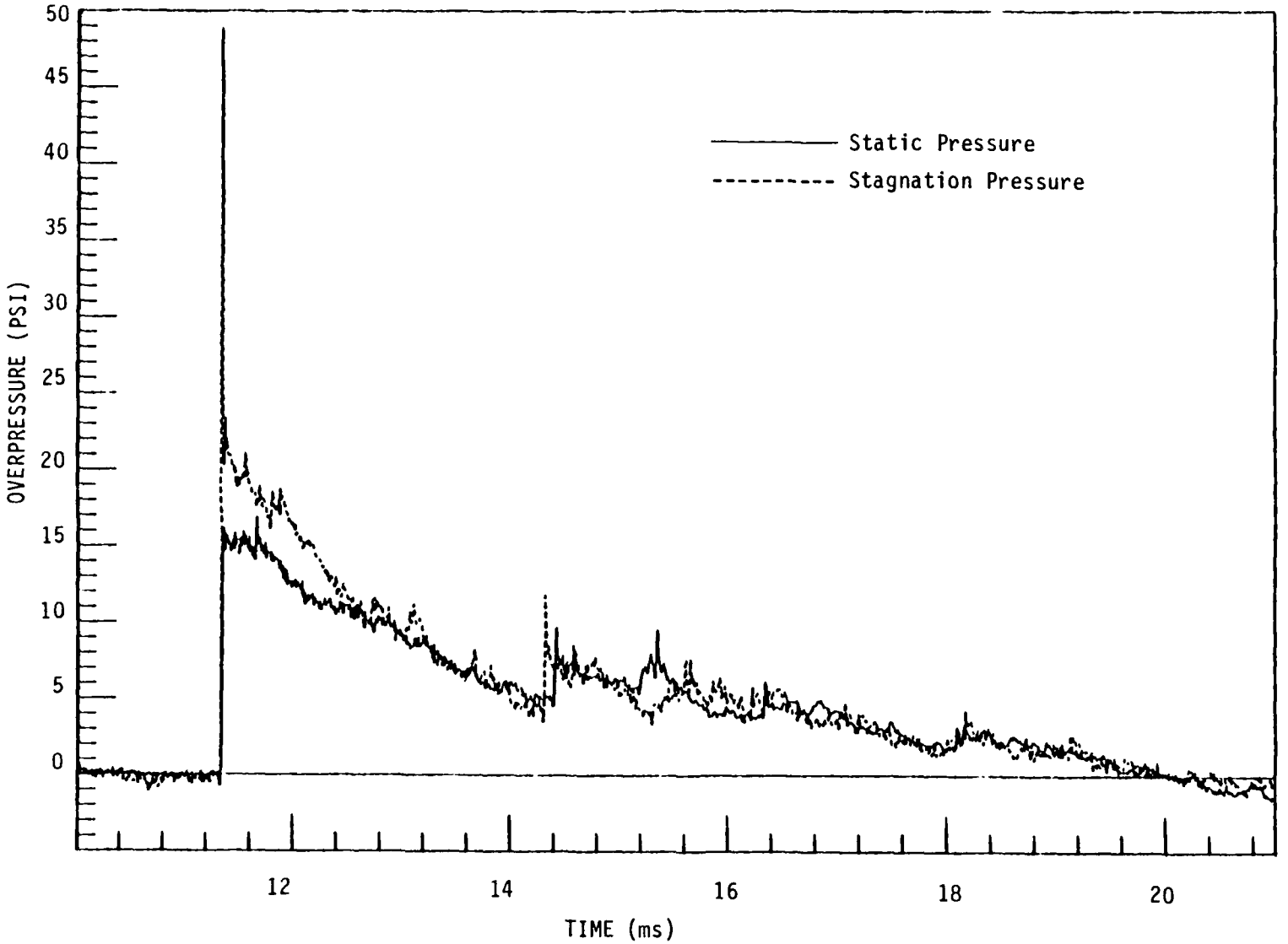

Figure 33. Superposition of static and stagnation overpressures. Data from test CD-13 (at 90° location); 22.7 kg (50 lbm) propylene oxide, R = 10.1 m (33.0 ft).

as in Figure 34, the two waveforms do not correspond, for reasons that are not presently understood.

A possible source of the large-amplitude secondary wave systems could be the result of temporally or spatially incoherent energy release by the detonating fuel-air cloud. The energy of combustion is apparently being coupled to the atmosphere asymmetrically, or as a series of pulses, rather than added uniformly and only benind a point-symmetrical detonation front of zero thickness. (Calculations of ideal fuel-air explosions (References 2, 4, 5) have generated only low-amplitude, negative-phase waves of the type represented schematically on Figure 21(c). All of these calculations have in common the assumptions of point symmetry; uniform initial fuel-air mixture; energy release only at the detonation front; kinetically frozen combustion produces; perfect gas behavior; and central, hard detonation initiation. Large-amplitude secondary waves have also not been observed during FAE and FOE* experiments in wnich the clouds were initially envelope-confined (References 6 through 8), with one possible exception (Reference 9). The use of envelope confinement in these experiments assured accurate geometric symmetry and precise central initiation.

Several characteristics of fuel-air explosions are thought to have a possible influence on the formation of secondary waves. These are cloud shape, initiator location, fuel distribution, initiator strength, detonation reaction zone length, and product gas chemical equilibrium shifts.

1. CLOUD SHAPE

If the detonating fuel-air cloud is not hemispherical, regions adjacent to the cloud boundaries will exist in which components of the detonation and the transmitted air shock meet at oblique angles, due to differences in their propagation velocities and directions. The oblique shock interactions will generate reflected waves which

*Fuel-oxygen explosion.

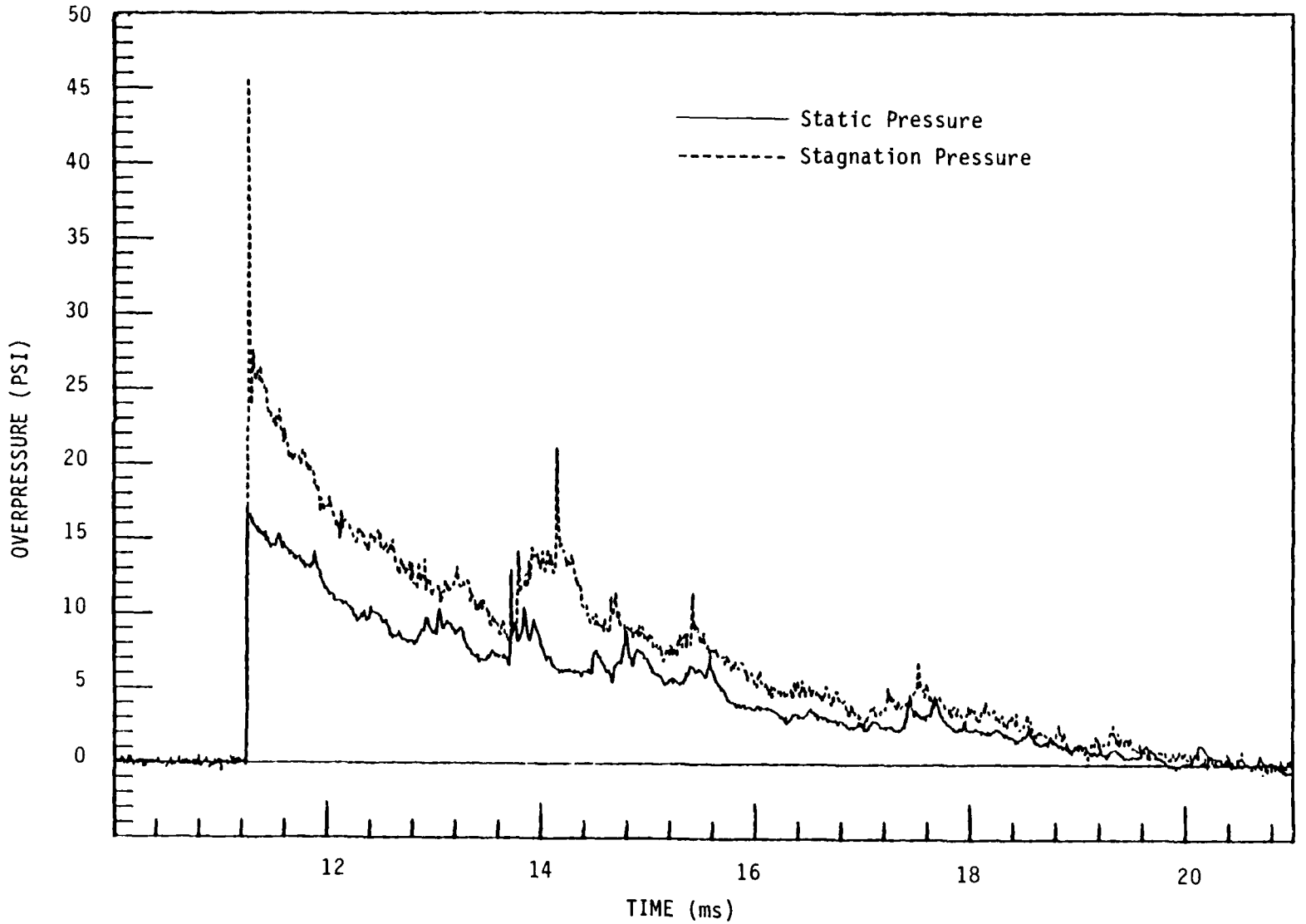

Figure 34. Superposition of static and stagnation overpressures. Data from test CD-13 (at 0° location); 22.7 kg (50 lbm) propylene oxide, R = 9.93 m (32.6 ft).

may be shocks. The reflected waves could strike the ground at an appreciable distance behind the lead shock if the interaction occurs substantially above ground.

This phenomenon, due to shape, has been observed with cylindrical HE charges having sharp corners (References 10 and 11). The mechanism is illustrated schematically for that case on Figure 35, while Figure 36 shows a series of experimental pressure records taken on the ground along the axis of a detonated cylindrical HE charge. A strong secondary wave can be seen on the first three traces as it overtakes the leading blastwave shock. According to Reference 10, such secondary waves were eliminated when the ends of the cylindrical charges were shaped into hemispheres. This **demonstrated that the sharp-cornered charge shape was responsible for the secondary waves. It is possible that an equivalent mechanism could be operative in fuel-air cloud explosions, if the clouds formed are not exactly hemispherical.**

2. INITIATOR LOCATION

Ideally, an FAE cloud should be initiated at the center of symmetry. If a normal hemisphere is initiated above ground, either a spherical detonation or the initiating blastwave will reflect from the ground. The region of reflection will comprise an oblique detonation front and an oblique shock front. This differs from the ordinary reflection of a spherical blastwave from a surface, and may be accompanied by additional shocks or expansions. In the case of marginal detonation initiation, partially reacted or unreacted fuel may be ignited by the reflected shock, producing a second reaction front. In addition, above-ground initiation would result in a spherical detonation that would overtake the cloud boundary in a non-coincident fashion. This could produce a boundary interaction, leading to reflected waves, in a manner equivalent to that described in (1) above. The same type of boundary interaction would also occur if the initiator were located on the ground but were offset horizontally. Horizontal misalignment of the initiator is equivalent to cloud displacement due to atmospheric movement.

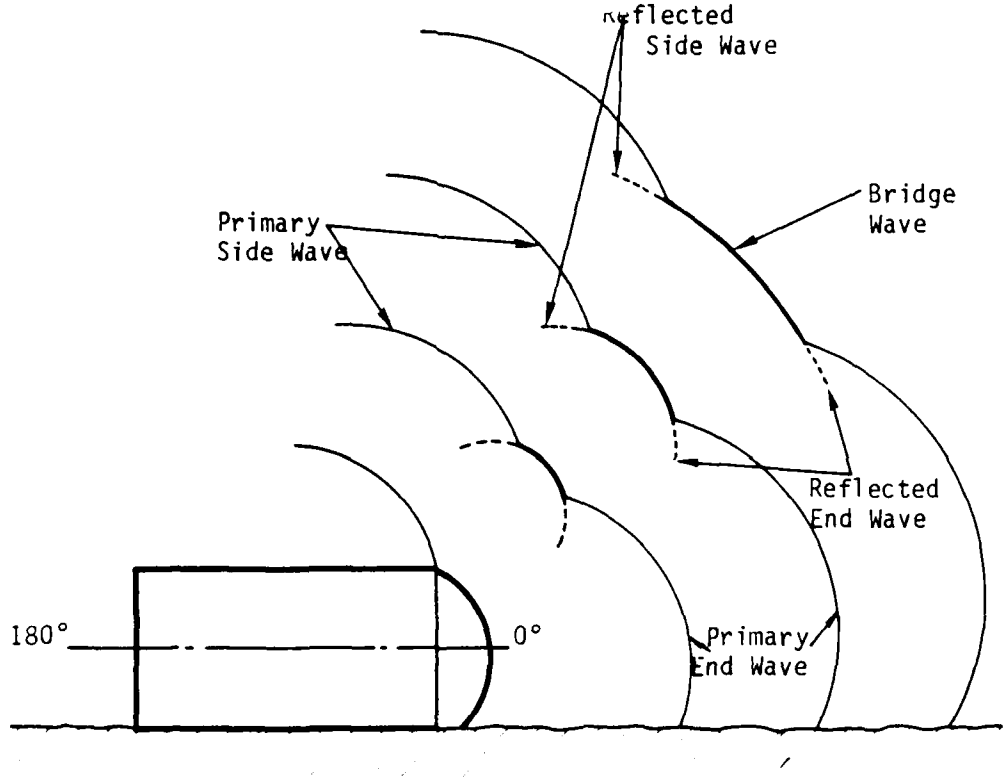

Figure 35. Schematic of multiple wave development from corner of cylindrical high explosive charge (from Reference 10).

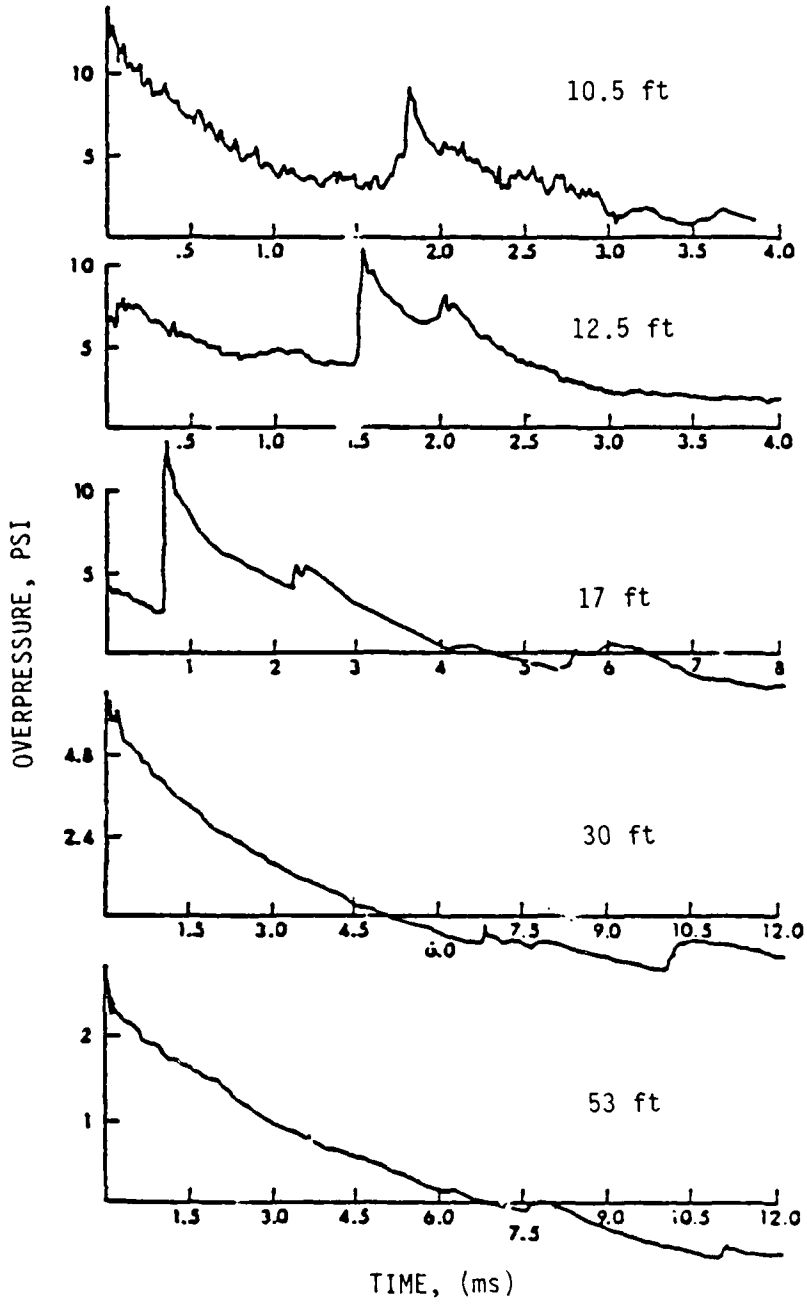

Figure 36. Experimental pressure records from detonation of cylindrical explosive charge with sharp corners. Data taken on ground along charge axis direction (from Reference 11).

Figure 37 is a frame from a high speed film of a propylene oxide FAE. The 25 gm (0.55 lbm) C-4 initiator in this test was located 1.2 m (4 ft) above ground along the vertical axis of the cloud. The reflected wave is very clearly defined in this example. It should be noted that the strength of the reflected wave is associated not only with the initiator energy, which was very small in this case, but with all of the detonated fuel in the sphere of radius equal to the initiator height (vertical offset).

3. FUEL DISTRIBUTION

Non-uniform fuel distribution would lead to refraction of the detonation front within the cloud. This could generate reflected compression or expansion waves. If the initiator strength were marginal, initiation might be directional, leading to an irregular detonation front with multiple wave reflections.

Fuel non-uniformity could take several forms. The fuel could be contained in pockets spaced irregularly within the cloud. This type of non-uniformity could account for rotational asymmetry of secondary waves. Another non-uniformity might be a large void volume in the vicinity of the cloud center, which would lead to multiple wave reflections (presuming that the cloud could be centrally initiated under these conditions). Also, the droplet size distribution might vary within the cloud, so that the detonation reaction zone would be continually undergoing transitions with accompanying wave reflections.

4. INITIATOR STRENGTH

Critical region (marginal) initiation (Reference 12) could potentially generate one or more nested explosions, as well as an inward-moving detonation (retonation), similar to what occurs in deflagration-to-detonation transition (Reference 13). When initiation is marginal, a galloping behavior is observed (Reference 14); that is, the detonation front velocity oscillates in a pulsed

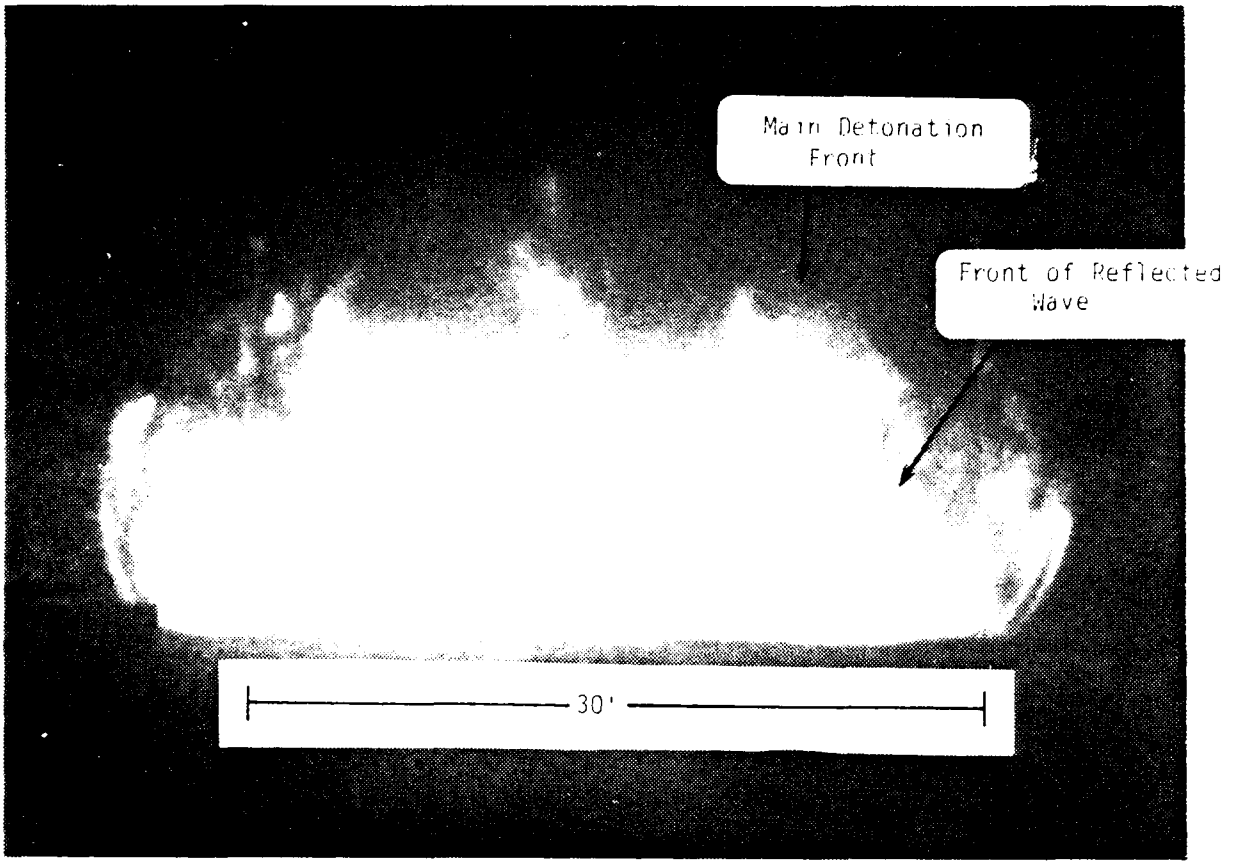

Figure 37. Frame from high speed film taken during FAE test 2533; 22.7 kg (50 lbm) propylene oxide. Initiator height was 1.22 m (4 ft) above ground, located on cloud axis. The distance between the vertical poles is 9.2 m (30 ft).

manner. Presumably, reflected waves are formed in this process. In addition, in the case of marginal initiation, the detonation shock front and reaction zone tend to separate. If the reactions following ignition are then extremely fast, a compression pulse will form during this unsteady initiation process.

5. REACTION ZONE LENGTH

If initiation is not marginal or excessive, a steady detonation develops within the boundaries of the FAE cloud. The normal hydrodynamic structure of a detonation comprises a shock front followed by a pressure drop when the smooth, exothermic chain-breaking reactions commence. However, in the case of some liquid-fuel/oxidizer combinations (especially when liquid fuels and pure oxygen are involved) the ignition is not smooth but explosive (Reference 15). In such cases, multiply-nested blastwaves, superimposed on a globally decaying pressure profile, appear in the reaction zone (Reference 16). If the reaction zone is extremely long due to large droplets, marginal stoichiometry, or substantial but not complete pre-vaporization of the fuel (Reference 17), these nested blastwaves could persist beyond the cloud boundary.

A second effect of a long reaction zone might be that it would produce a strengthened rarefaction behind the detonation. A strengthened rarefaction could be expected if the mass in the detonation reaction zone is comparable to the total fuel-air cloud mass (Reference 2). A strong rarefaction would change the characteristics of the gas dynamics which normally generate an inconsequential secondary wave in the negative phase. It may be that this secondary wave would be amplified by the altered gas dynamics.

6. COMBUSTION PRODUCT EQUILIBRIA

The products of combustion in a detonation are highly dissociated due to their elevated temperature. In the rarefaction

that follows, the product temperature drops substantially. Further temperature reduction occurs within a fuel-air cloud after the detonation passes through the cloud/air interface. Equilibrium recombination of the combustion products accompanies these temperature reductions, with recovery of the dissociation energies. If the recombination occurs with sufficient rapidity, a compression wave packet could be formed from this effectively impulsive energy addition.

As an example, Figure 38 shows the calculated time variation of static temperature within a detonated heptane vapor-air cloud. The calculation (Reference 2) was carried out for a uniformly stoichiometric, 4.42 m (14.5 ft) radius cloud, which corresponds to the small scale experiments. The products of combustion in this calculation were assumed chemically frozen so that the temperature variations indicated are only suggestive of the magnitude of change. The detonation front arrives at the location in Figure 38, R = 2.91 m (9.54 ft), at t = 1.62 ms. At that time, the temperature rises to the C-J detonation level, T = 2550 °C (4620°F). The detonation products consist of significant amounts of the chemical species N_2, H_2O, CO, CO_2, O_2, OH, H_2, NO, H, and O. Within the next 8 to 10 ms the temperature at this location drops by nearly 1000°C (1800°F) to about T = 1580°C (2870°F). At this relatively low final temperature the products will re-equilibrate to a condition in which the major constituents are N_2, H_2O, and CO_2. This represents effectively complete combustion and the energy of dissociation expended at the higher temperature is returned to the flow.

It was anticipated that the effects of initiator location, initiator strength, equilibrium shifts, and detonation reaction zone length would likely be negligible with large-scale clouds, although these same effects might be contributory or dominant at smaller

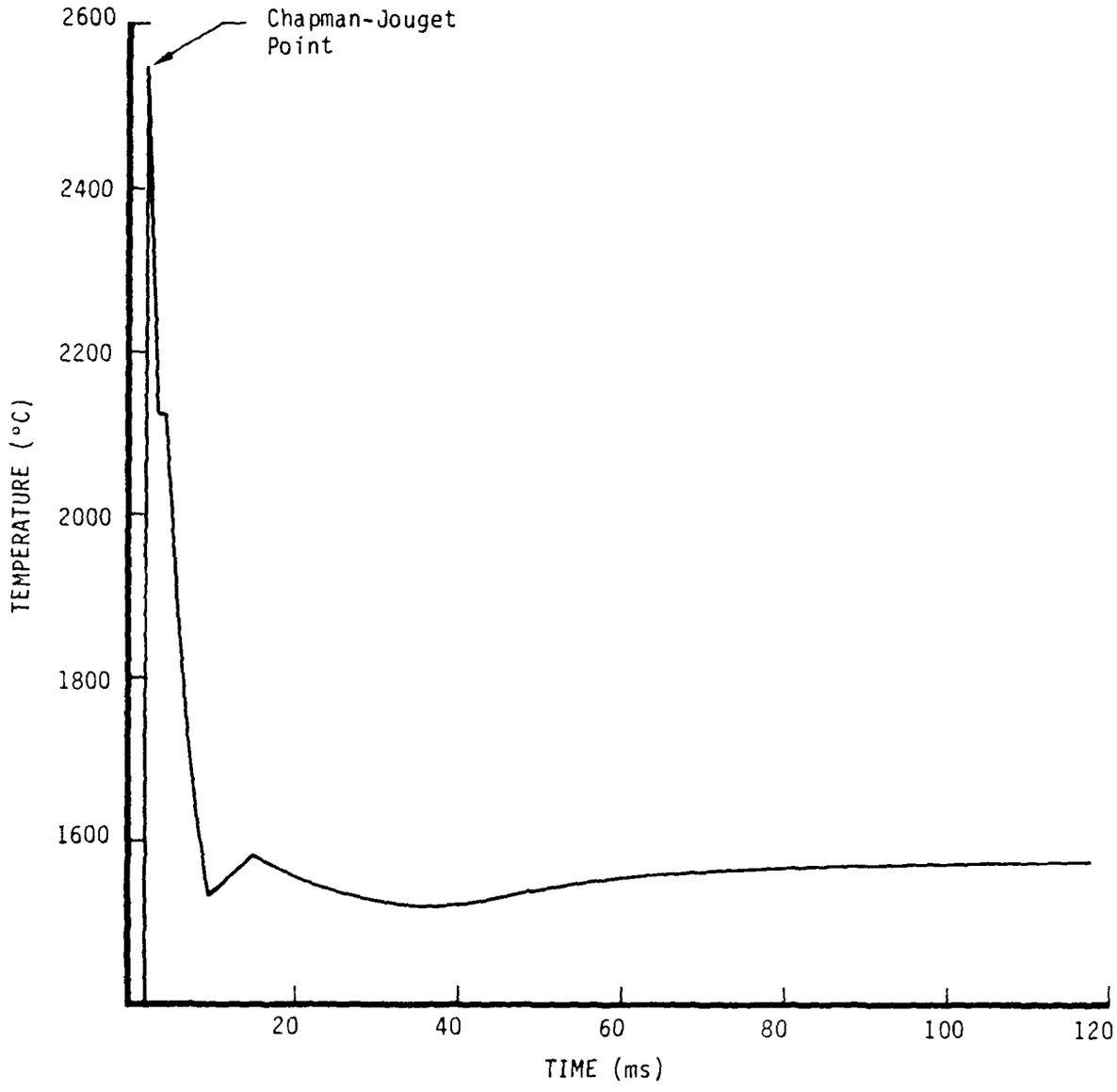

Figure 38. Calculated temperature variation inside detonated fuel-air cloud (see text for conditions).

scales. However, it was felt that any impact of cloud shape asymmetry or fuel distribution non-uniformity would not diminish with increasing scale, and for that reason it was thought that their effects should be investigated first.

The shape of the fuel-air cloud is important to the nuclear airblast simulator objectives for reasons other than the possible contribution of asymmetry to secondary waves. A hemispherical FAE cloud is theoretically the most efficient shape (Reference 18) and the cloud dimensions are minimized for a given specified yield. In addition, predictable testing in all directions and at the highest overpressure levels is possible from a hemispherical FAE. However, truly hemispherical clouds have not as yet been formed at small scale with the point source, multiple-nozzle impulsive dispenser. It was accordingly felt that the initial attempts to eliminate secondary waves in FAE airblasts should be directed to improvements in cloud shaping. If cloud shape were to prove inconsequential to the formation of secondary waves, the FAE simulator technology would in any case be advanced by such investigations.

The shape of FAE clouds that are formed by point-source dissemination is distorted by large scale air vortices (Reference 2). The process by which this distortion takes place is illustrated on Figure 39. Liquid jets flowing radially outward from the source disseminator drag on the atmospheric air, causing it to move away from the source. This reduces the pressure near the center of the cloud so that air is drawn inward on the underside of it. At the center, this inward-moving air is turned vertically, forming into torroidal vortices around the cloud axis. Droplets become entrained in the vortex motion, deforming the cloud. The vertical air movements in the vicinity of the dispenser deflect the liquid jets as they emerge from the nozzles, further distorting the cloud shape. An example of a distorted cloud is given in Figure 40.

Cloud shape distortion is aggravated by increasing either the dispenser jet momentum or the number of jets in the hemispherical

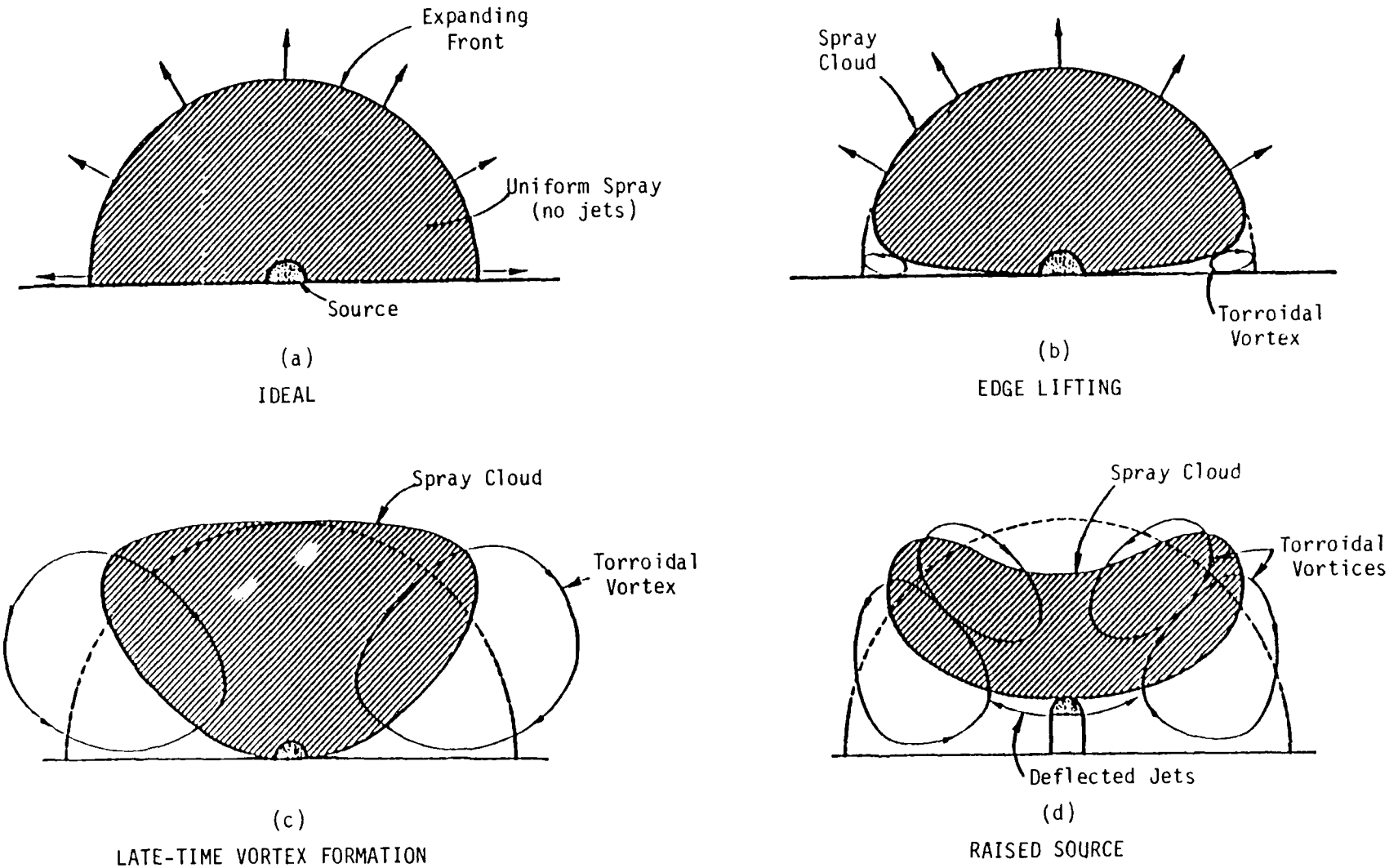

Figure 39. Distortions of expanding point-source spray clouds induced by aerodynamic interactions between spray and air. The dashed lines represent the desired hemispherical shape.

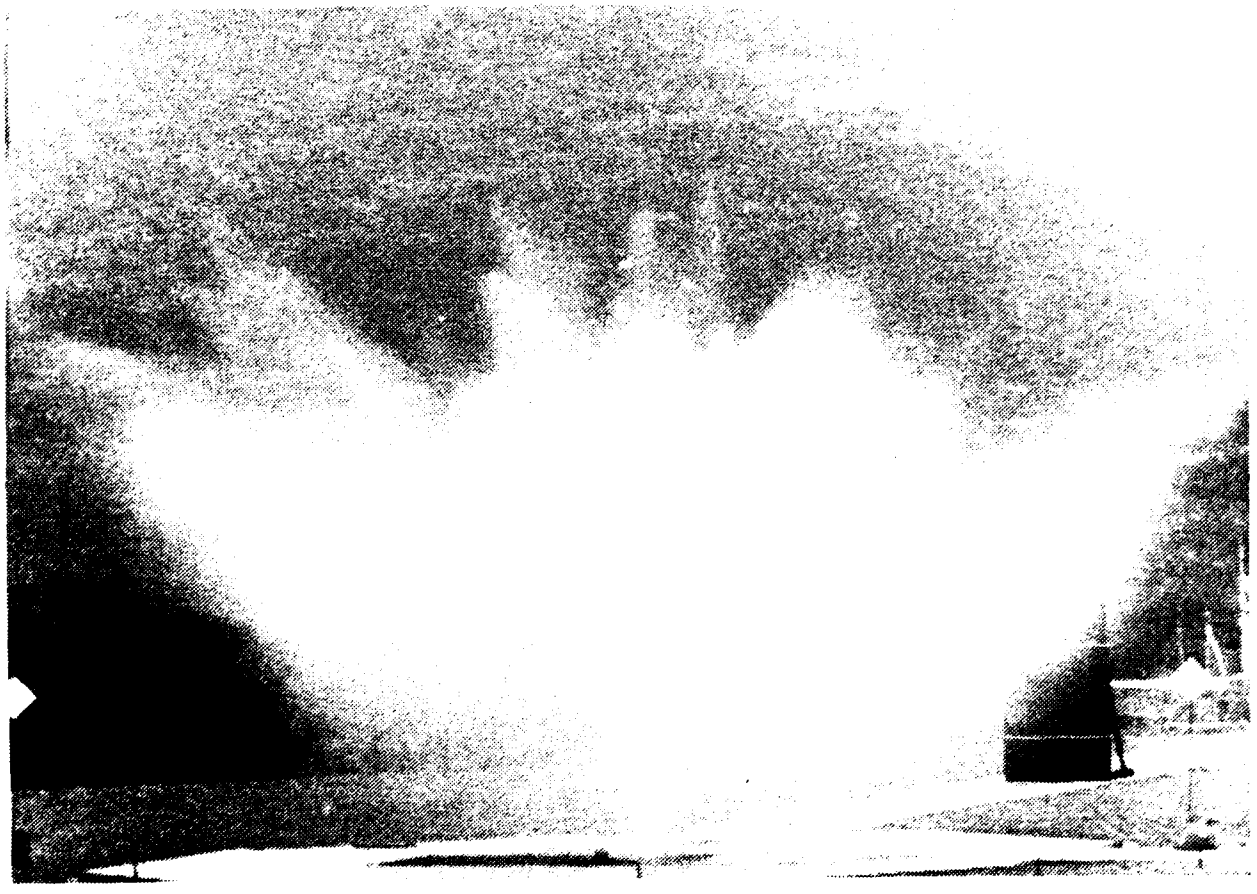

Figure 40. Frame from high speed film showing fuel-air cloud distorted by large-scale air vortices; test CF-9, 18.1 kg (39.9 lbm) heptane, 1400-nozzle point source. The distance between the diamond-shaped markers is 9.2 m (30 ft).

array. When a small number of low momentum jets are used, large-scale air vortices do not form because the smaller pressure drop at the cloud center is relieved by air counterflow between jets. In this case it is likely that a large number of low-strength vortices develop between pairs of adjacent jets. Unfortunately, the fuel is poorly dispersed with this arrangement, being confined to cylindrical regions near the individual jet centerlines. The cloud takes on a spiked appearance, an example of which appears in Figure 41. When detonated, clouds of this shape generate explosions of relatively low efficiency. On the other hand, if a greater number of liquid jets at higher velocity are used, the jets spread laterally and overlap. This fills in the cloud more uniformly, but it is when the cloud is filled in that large-scale voctices form and distort the cloud shape as in Figure 40.

A number of attempts were made to overcome vortex-induced cloud distortion while maintaining reasonably uniform fuel distribution. For these tests, a large number of high velocity jets was used, but several clusters of dispenser nozzles were blocked. The blocked groups of nozzles were uniformly spaced over the hemispherical array. The purpose of blocking clusters of nozzles was to provide a limited number of unobstructed air paths to the cloud center. It was hoped that a blockage pattern could be found that would allow enough airflow through these openings as to relieve the reduced pressure at the cloud center, without compromising the fuel distribution uniformity throughout the majority of the remaining cloud volume. This would reduce the tendency for air to spontaneously flow into the cloud on its underside, and would thereby prevent the formation of large-scale torroidal vortices.

The two types of nozzle blockage patterns that were tested are illustrated on Figure 42. Blockage was accomplished by bolting machine screws through the nozzle openings in the dispenser head. The dimple pattern in Figure 41(a) consists of seven equally spaced circular clusters. Tests were conducted with this pattern in which

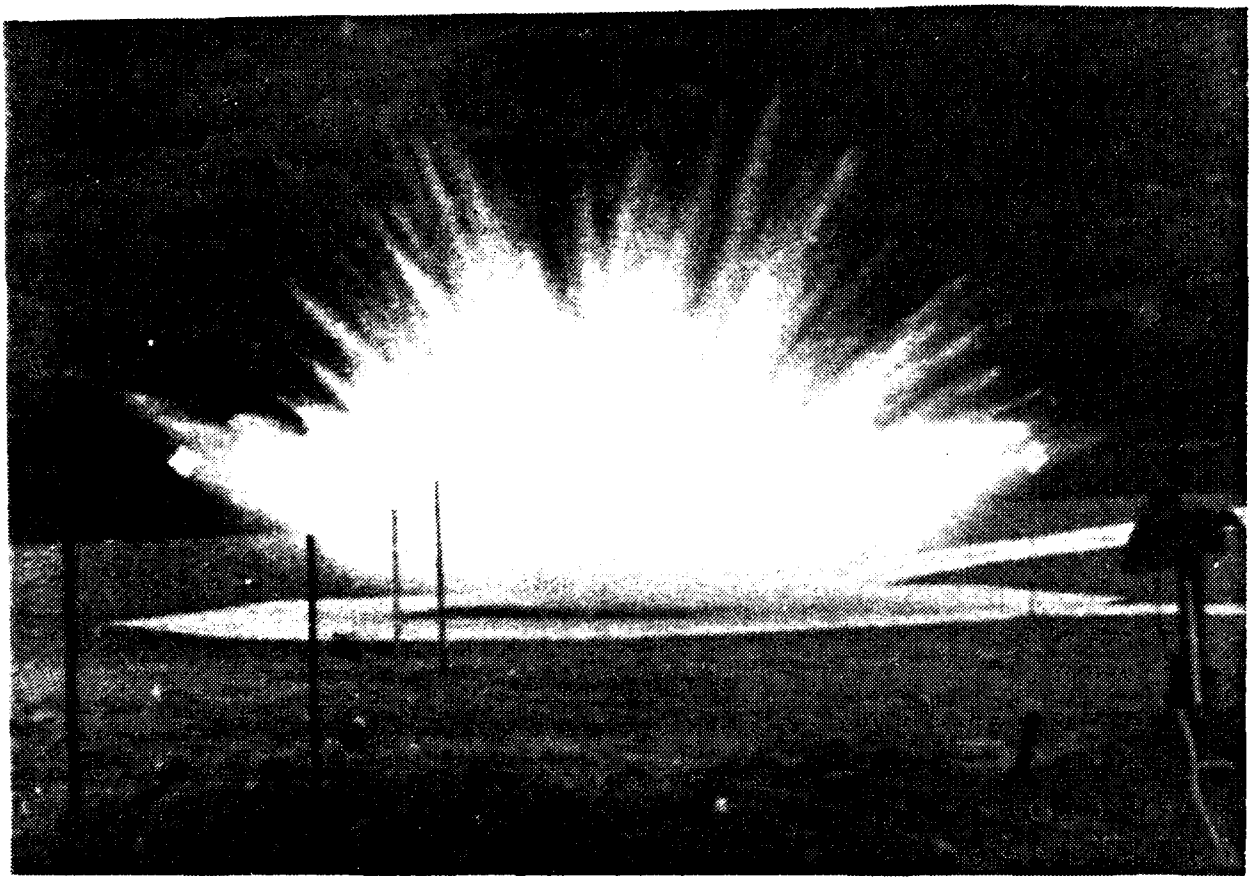

Figure 41. Frame from high speed film showing fuel-air cloud formed from partially overlapping jets; FAE test CD-9, 78.5 percent heptane, 21.5 percent propyl nitrate by volume, 0.0265 m^3 (7 gal.) total mixture, 600-nozzle point source. The distance between the diamond-shaped markers is 9.2 m (30 ft).

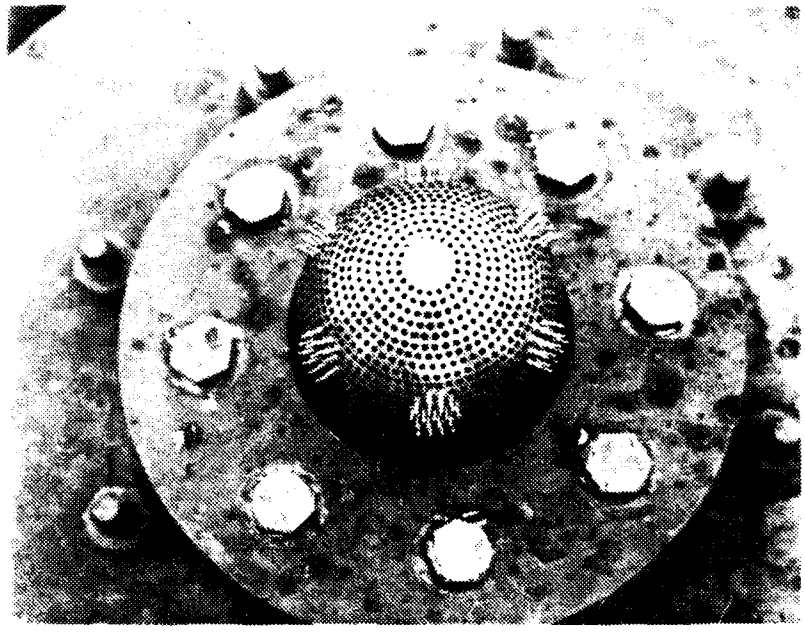

(a)

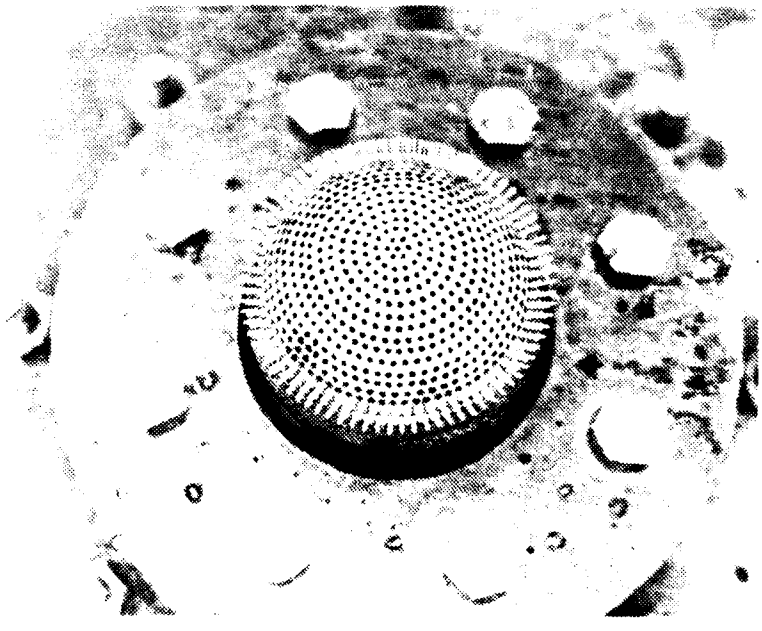

(b)

Figure 42. Dispenser head nozzle blockage patterns: (a) dimple-type pattern, (b) ring pattern.

the total blockage amounted to 2, 10, 15, 20, and 25 percent of the total number of nozzles. The other blockage pattern, which is shown in Figure 42(b), is a continuous axisymmetric ring. The ring was located so as to roughly divide the nozzle head into two equal areas (with the same number of nozzles above and below the ring). In this pattern, tests were conducted with blockage amounting to 5.5, 7.5, and 10 percent of the total number of nozzles. The test conditions are summarized in Appendix B.

Figures 43 and 44 show the effect on cloud shape of nozzle blockage in the pattern of Figure 42(a). These examples should be compared with Figure 40, which shows a cloud formed under similar conditions but with no blockage. With 25 percent blockage (Figure 43), the cloud extends fully to the ground, and its overall size is greatly increased. The shape is characterized by a number of large thumblike projections and deep indentations, presumably the result of local vortices that form from air drawn in through the blocked areas. When a cloud of this shape was detonated, the pressure records on Figure 45 were obtained. A secondary wave of moderate strength appears on these records. Reducing the nozzle blockage to 10 percent seemed to improve the cloud shape, but when the cloud in Figure 44 was detonated, the pressure records (Figure 46) indicated the presence of a strong secondary wave.

Nozzle blockage in the ring pattern (Figure 42(b)) yielded very striking cloud shape changes. The changes, however, were not in the direction of improved hemisphericity. Figure 47 is an example of this. The cloud extends to the ground but the void region is very large compared with the fractional area that was blocked on the nozzle head. None of the clouds having this shape were detonated.

The use of nozzle blockage to modify cloud shape was abandoned after these disappointing results. Other techniques will have to be tried if hemispherical clouds having uniform fuel distribution are to be attained. For example, experiments might include nozzle arrays with some downward-directed jets, or arrays which have variable nozzle diameters or jet velocities.

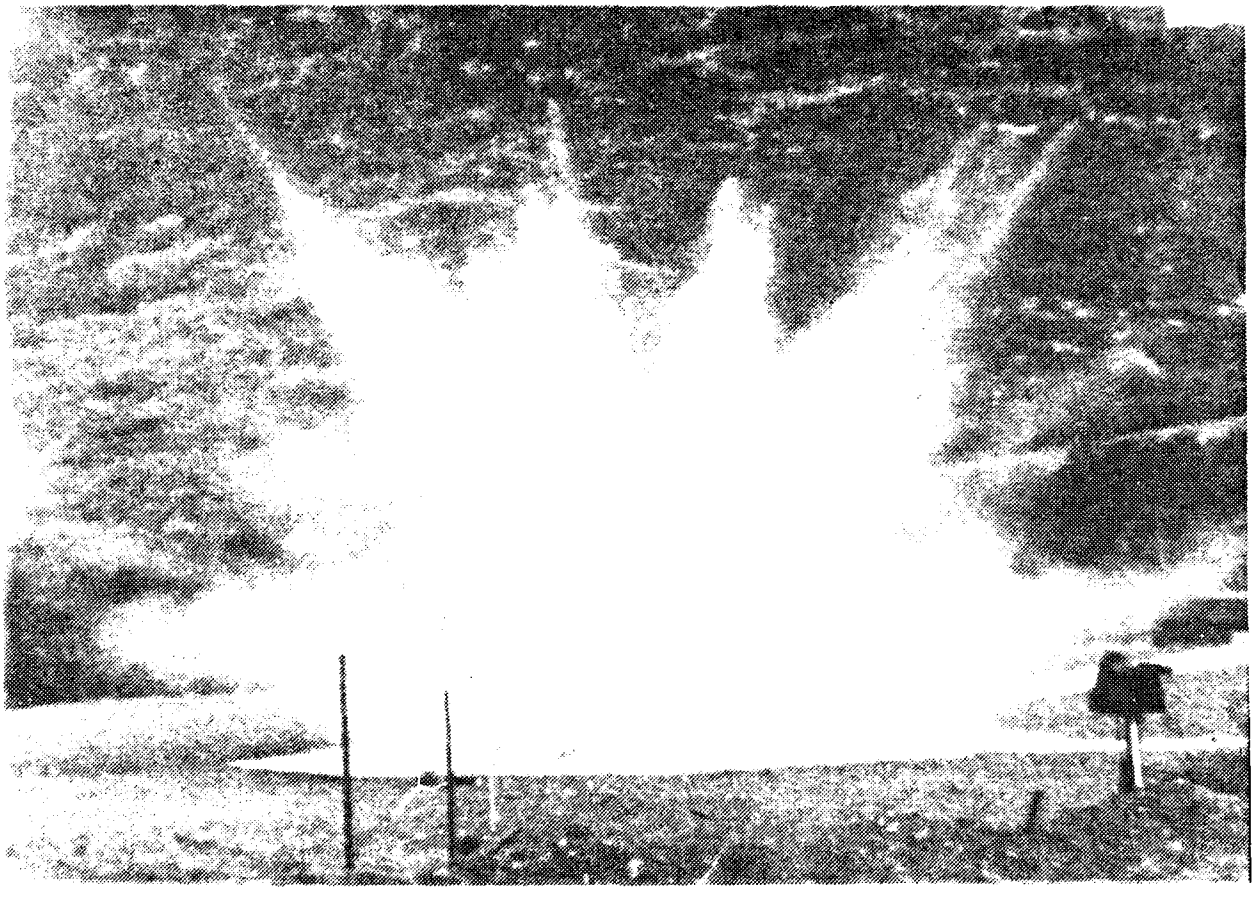

Figure 43. Heptane cloud formed with dimple-type nozzle blockage pattern, 1400-nozzle head with 20 percent blockage, test CF-15. The distance between the diamond-shaped markers is 9.2 m (30 ft).

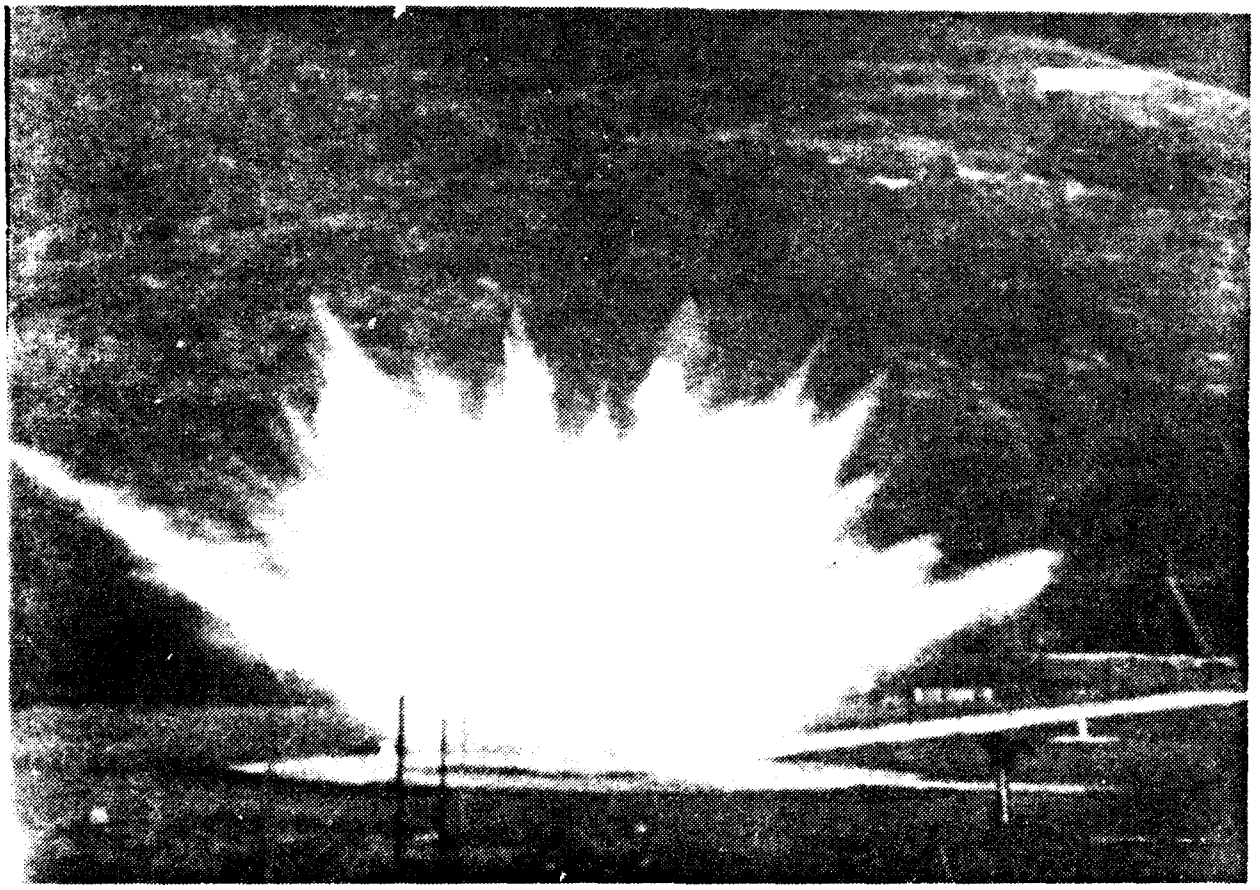

Figure 44. Cloud formed with dimple-type nozzle blockage pattern, 1400-nozzle head with 10 percent blockage, FAE test CD-11, 78.5 percent heptane with 21.5 percent propyl nitrate by volume. The distance between the diamond-shaped markers is 9.2 m (30 ft).

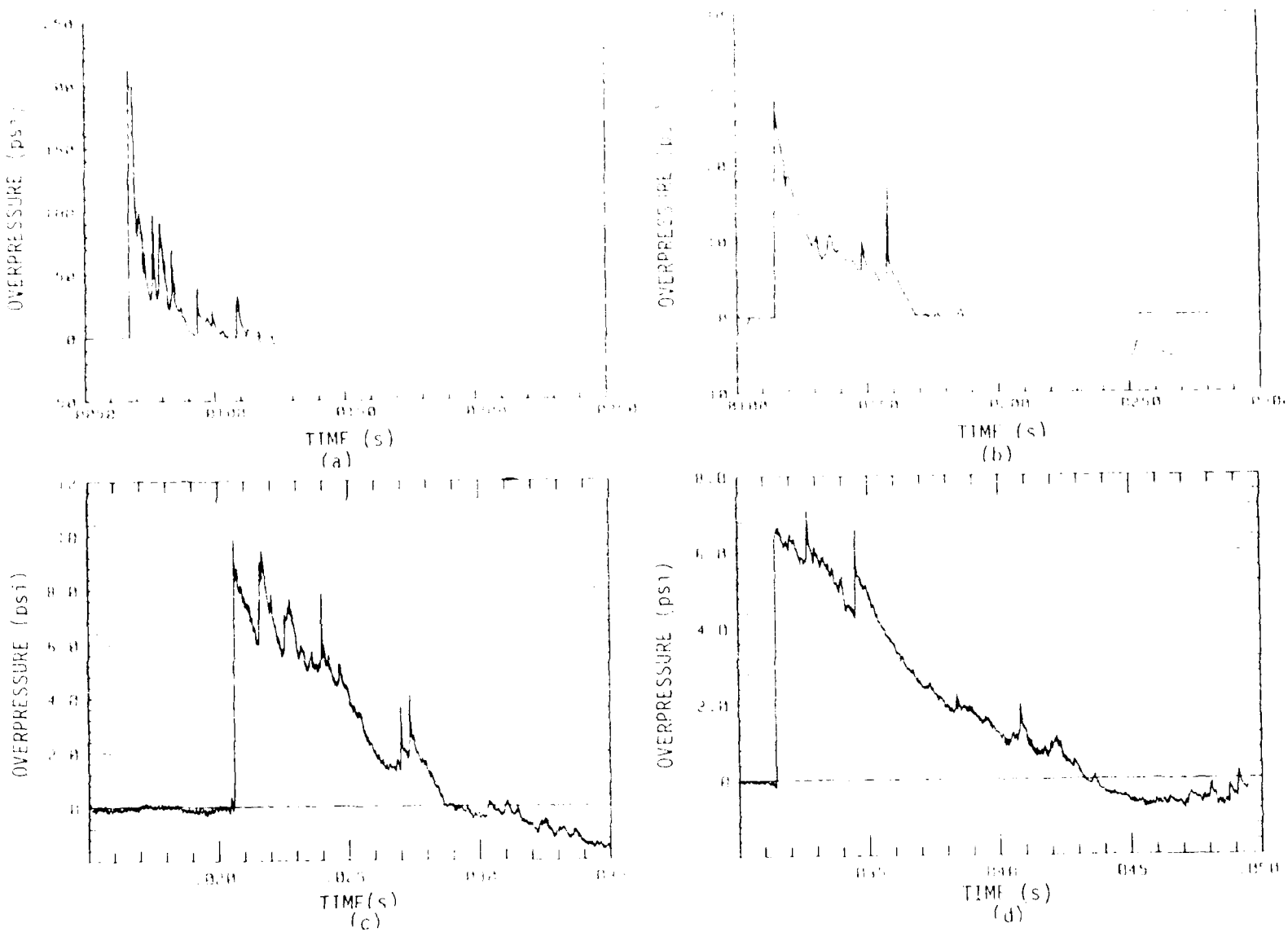

Figure 45. Raw static overpressure records, FAE Test CD10, 78.5% heptane, 21.5% propyl nitrate by volume, 0.0256 m^3 (7. gal.) total mixture, 1400-nozzle head with 25% dimple-type blockage. (a) R = 5.92 m (19.4 ft); (b) R = 9.93 m (32.6 ft); (c) R = 13.9 m (45.6 ft), (d) R = 18.9 m (62.0 ft).

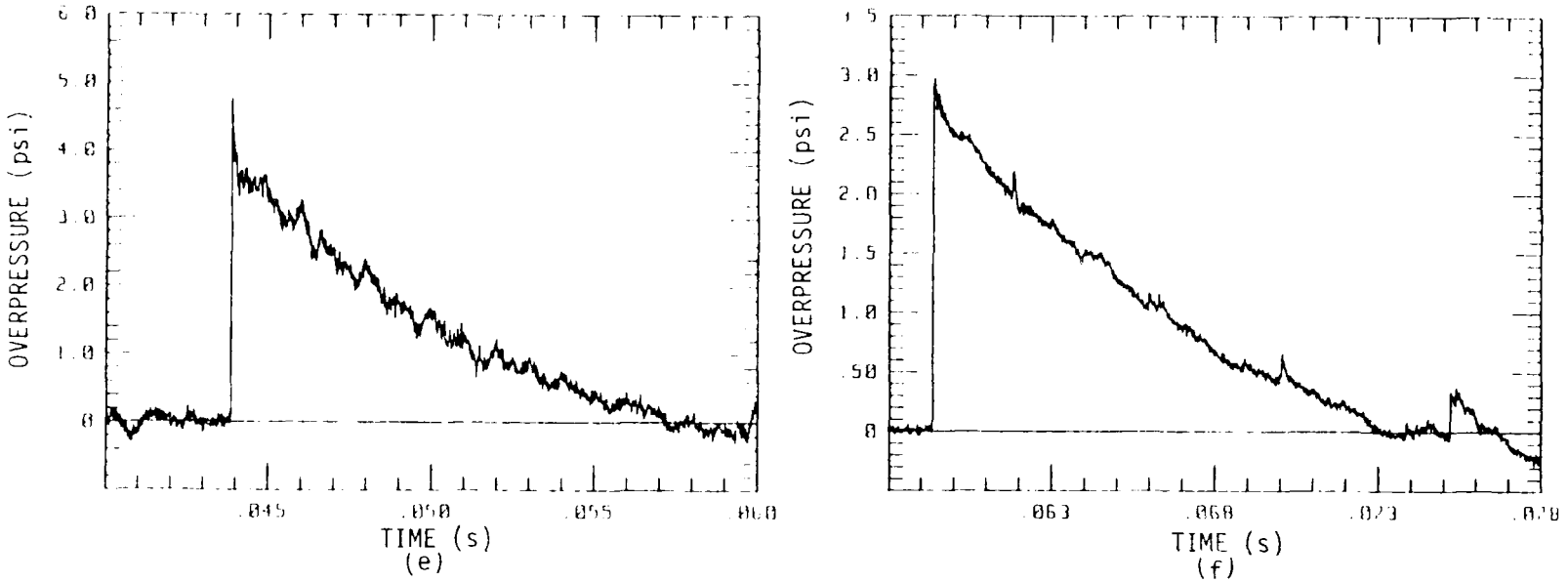

Figure 45 (cont'd) Raw static overpressure records, FAE Test CD10, 78.5% heptane, 21.5% propyl nitrate by volume, 0.0256 m^3 (7 gal.) total mixture, 1400-nozzle head with 25% dimple-type blockage. (e) R = 23.9 m (78.3 ft); (f) R = 29.9 m (98 ft).

AD-A149 473 INVESTIGATION OF A REUSABLE FUEL-AIR EXPLOSIVE NUCLEAR AIRBLAST SIMULATOR(U) S-CUBED LA JOLLA CA T H PIERCE ET AL. 01 FEB 82 SSS-R-81-4897 DNA-5990F 2/2

UNCLASSIFIED DNA001-80-C-0067 F/G 18/3 NL

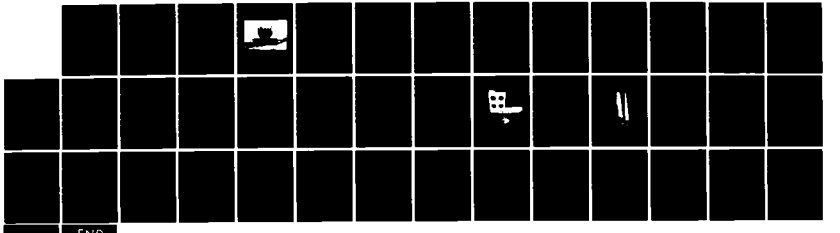

END

FILMED

DTIC

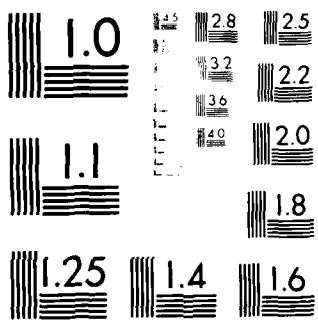

MICROCOPY RESOLUTION TEST CHART
NATIONAL BUREAU OF STANDARDS-1963-A

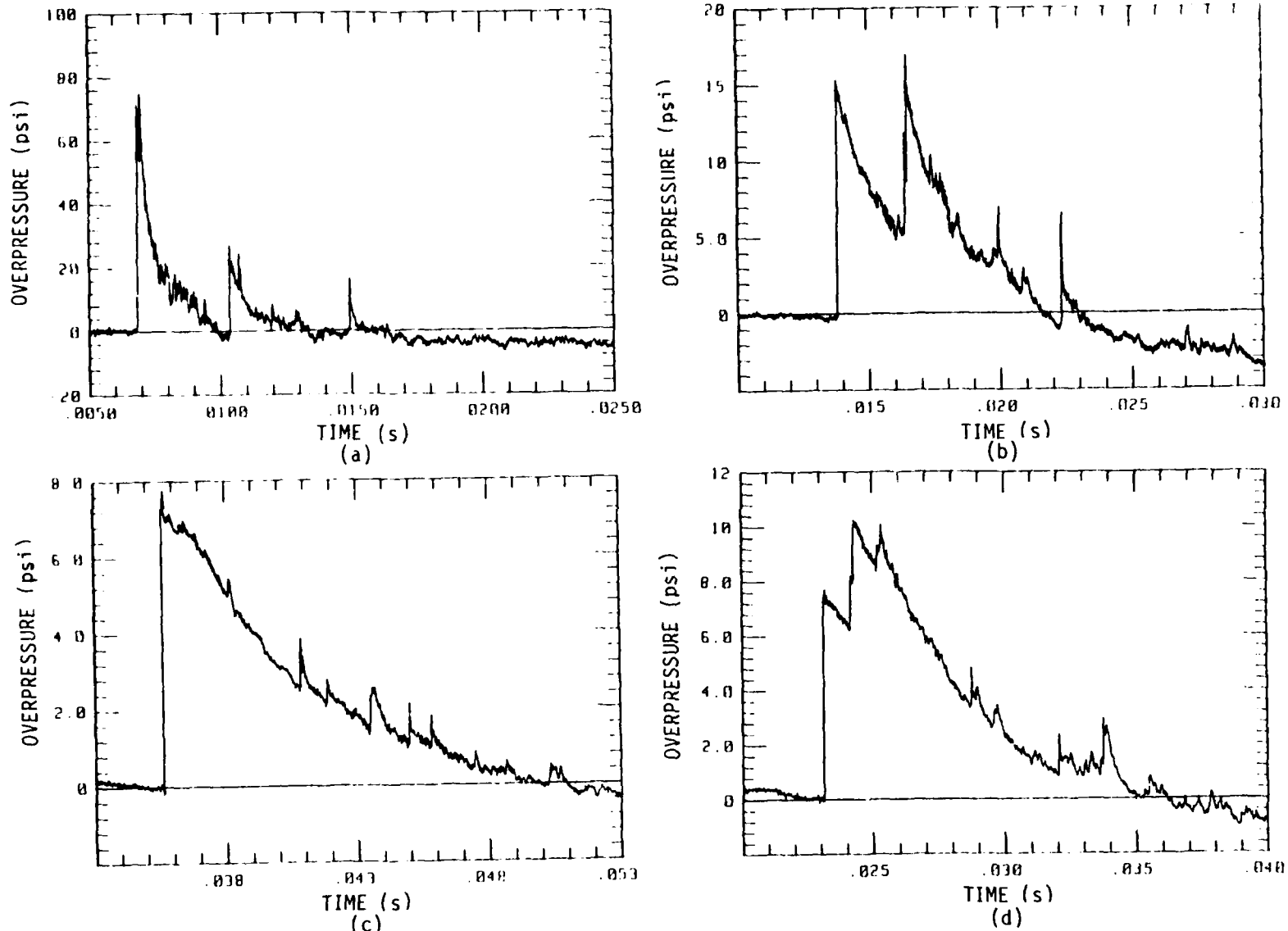

Figure 46. Raw static overpressure records, FAE Test CD11, 78.5% heptane, 21.5% propyl nitrate by volume, 0.0265 m^3 (7 gal) total mixture, 1400-nozzle head with 10% dimple-type blockage. (a) R = 59.2 m (19.4 ft); (b) R = 9.93 m (32.6 ft); (c) R = 13.9 m (45.6 ft); (d) R = 18.9 m (62.0 ft);

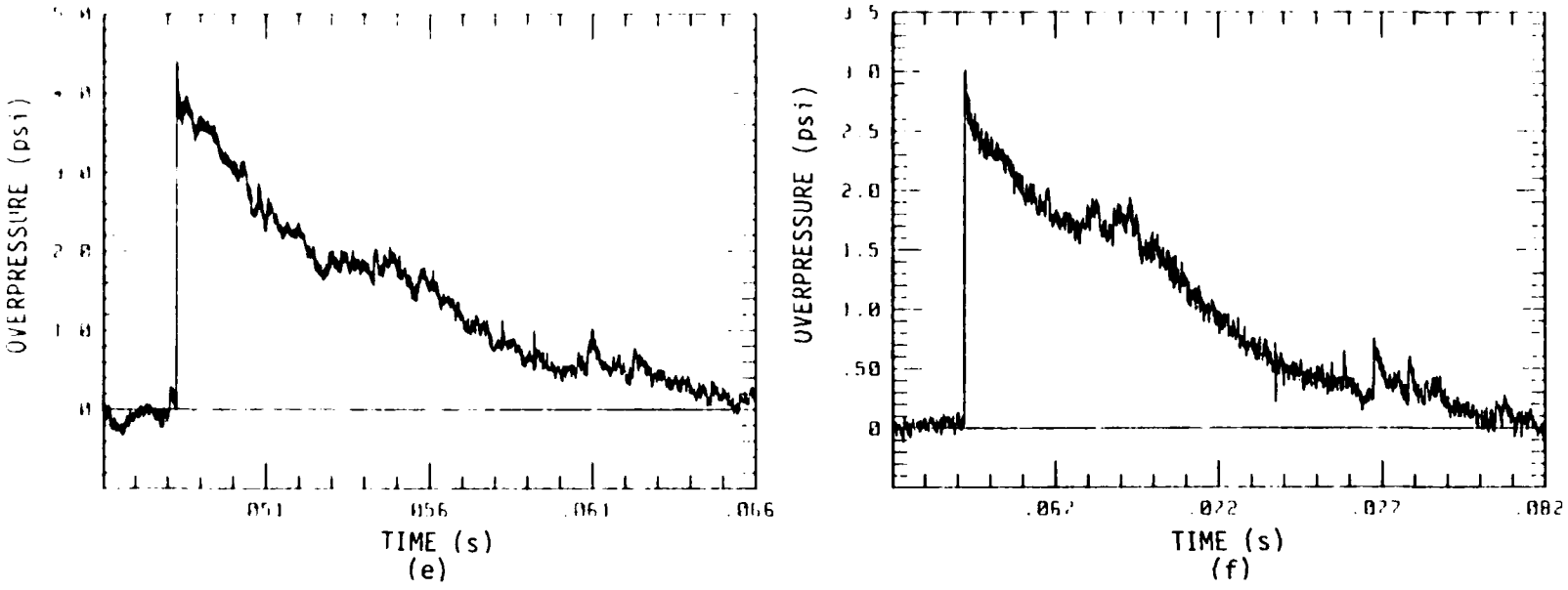

Figure 46 (cont'd) Raw static overpressure records, FAE Test CD11, 78.5% heptane, 21.5% propyl nitrate by volume, 0.0265 m^3 (7 gal) total mixture, 1400-nozzle head with 10% dimple-type blockage. (e) R = 23.9 m (78.3 ft); (f) R = 29.9 m (98 ft).

Figure 47. Heptane cloud formed with ring-type nozzle blockage pattern, 1400-nozzle head with 10 percent blockage, test CF-17. The distance between the diamond-shaped markers is 9.2 m (30 ft).

Since well-shaped aerosol clouds were not successfully produced in these experiments, the issue of cloud shape effects on secondary wave production in FAE airblasts remains unsettled. For purposes of isolating the effects of cloud shape in a controlled manner, it is suggested that gas-phase fuel-air mixtures be detonated, with the reactants initially contained in thin plastic envelopes (balloons) of various geometric shapes.

IV. PRESSURE INSTRUMENTATION REFINEMENTS

The earliest FAE/nuclear airblast simulation feasibility experiments were conducted on an unimproved test site area (References 1 and 2). The site was reasonably level but it had not been fully graded. It was located in a valley near the outlet of a small canyon, with shallow hills on two opposite sides.

Pressure transducers in use at the time were Sensometrics Model SP-91. These strain gage transducers were mounted on 1/3 m (1 ft) square steel or plywood plates and installed directly in the ground with the upper surface at ground level. Output from the transducers was recorded on a Honeywell Model 1858 oscillograph having a frequency response to 5 kHz. In most of the tests, however, the pressure transducer signals were filtered with a first-order lowpass circuit which limited the effective system response to about 1-2 kHz. Filtering was incorporated to eliminate intractable higher frequency noise, and although this measure also rounded shock wave peaks and obscured some waveform details, those details were not considered essential to the objectives of the early efforts.

Examples which characterize the data taken from early FAE tests are given in Figures 48 and 49 (Reference 19). These samples are taken from the same experiment. The two transducers were located at approximately the same radial distance, but they were 90 degrees apart. A number of impulsive pressure excursions are evident on both waveforms, and in addition, what appears to be a significant secondary wave is present on Figure 48. The substantial rotational asymmetry between pairs of pressure traces such as these was partly responsible for uncertainty as to whether the waveform aberrations were a result of peculiarities inherent to fuel-air explosions, or whether these disturbances could be attributed to characteristics of the instrumentation layout and installation.

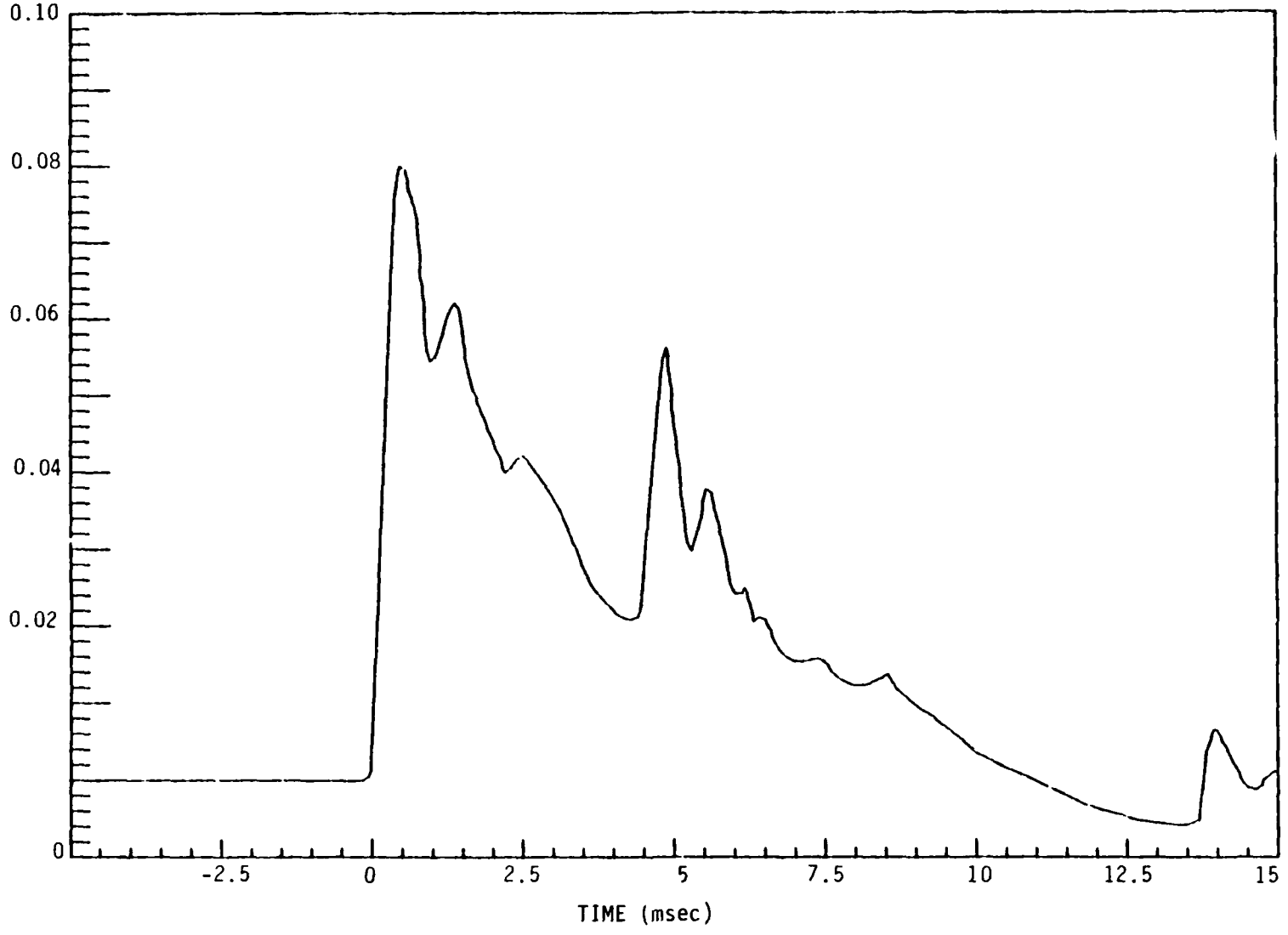

Figure 48. Pressure record obtained from FAE test 2531, 0.0265 m^3 (7 gal.) propylene oxide, R = 12.2 m (40 ft.).

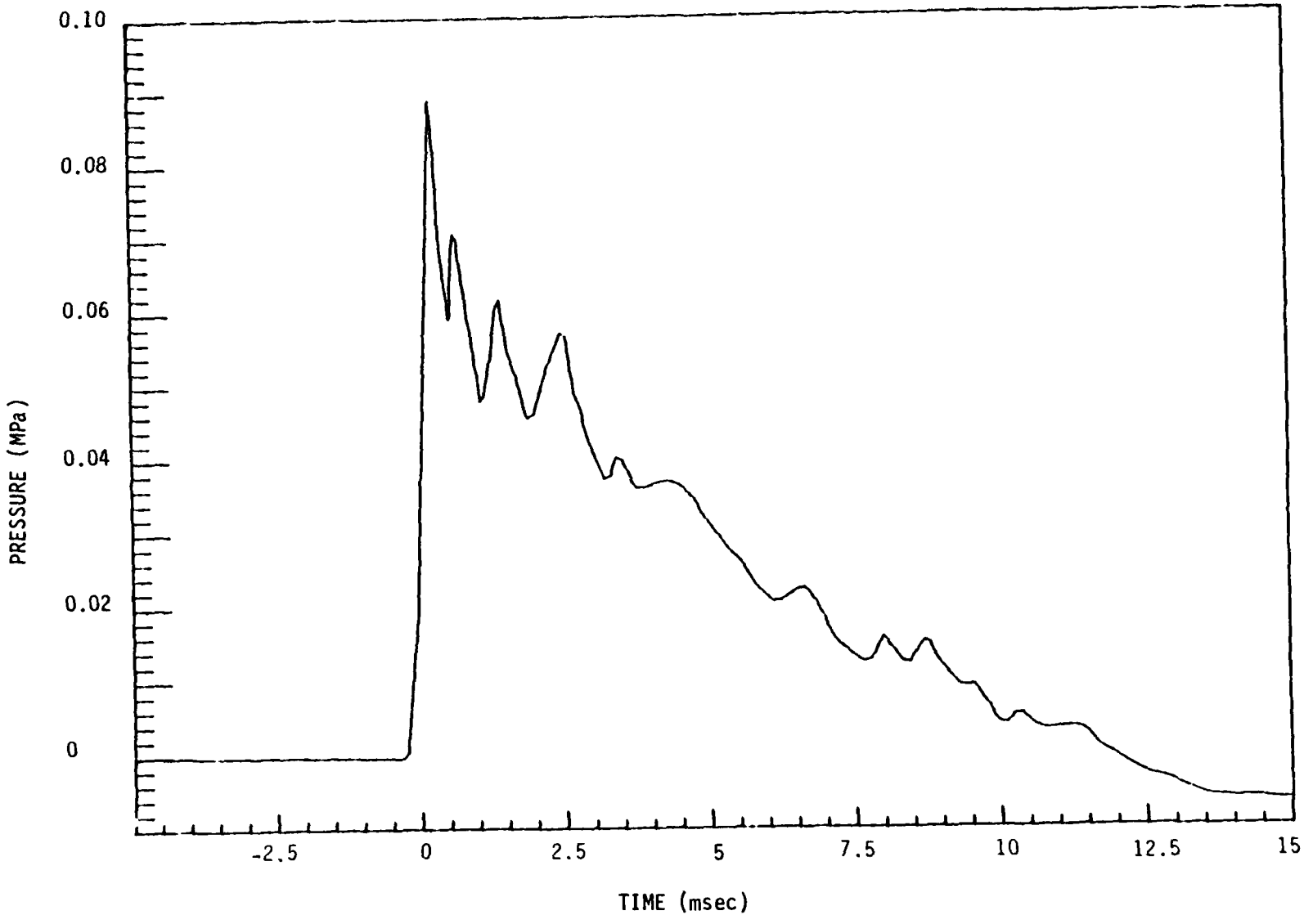

Figure 49. Pressure record obtained from FAE test 2531, 0.265 m^3 (7 gal.) propylene oxide, R = 13.4 m (44 ft.).

It was accordingly undertaken to improve the test site, with careful attention given to the transducer mountings and to their locations with respect to adjacent hills. The upgraded facility is described in detail in Reference 2. At the same time, piezoelectric pressure transducers (PCB Model 102A12) were acquired to replace the strain gage pressure transducers. In subsequent FAE testing, the piezoelectric transducers were used in conjunction with an EMI Model SE7000A 14-channel tape deck. At a recording velocity of 305 cm/s (120 in/s), this tape recorder has a frequency response to 80 kHz. It was the limiting component in the new data acquisition chain. Filtering was not used on the input to this device.

During the first tests of the improved experimental facility and instrumentation* (FAE tests CD-1 to CD-5), the pressure records from transducers close-in to the blast source exhibited considerable ringing. A worst-case example is given on Figure 50. The ringing was not a simple sinusoid; it could be ameliorated but not eliminated by a data processing procedure involving narrowband filtering of the waveform Fourier transform. It was felt that this ringing problem compromised the virtues of the instrumentation improvements, and that further FAE experiments should be postponed until the problem was resolved.

Piezoelectric pressure transducers respond to acceleration as well as to pressure. Generally, the extent of sensitivity to acceleration varies with the direction of movement. Most commercially available transducer designs include components which partially compensate at least for axial acceleration sensitivity. (A comparison of some widely used airblast pressure transducers appears on Table 2.) It was believed that physical oscillations of the pressure transducers were responsible for the pressure waveform ringing.

A number of steps were taken to refine the pressure instrumentation so as to reduce ringing and improve data confidence. These steps included modifications to the transducer

* See Appendix A.

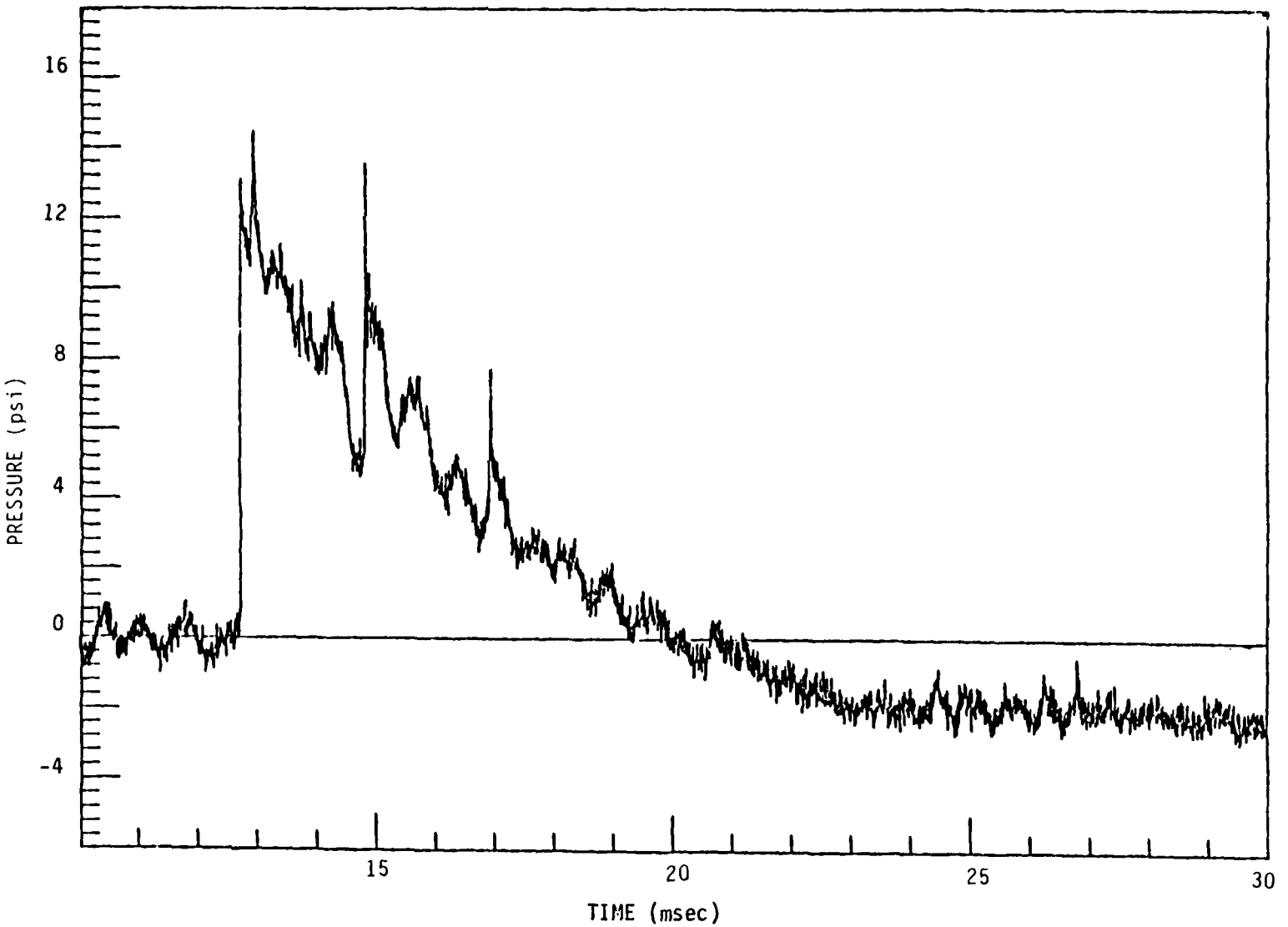

Figure 50. Pressure record obtained from FAE test CD-5, 0.265 m^3 (7 gal.) propylene oxide, R = 9.93 m (32.6 ft.).

TABLE 2

PRESSURE TRANSDUCER PERFORMANCE SPECIFICATIONS
(DATA DERIVED FROM MANUFACTURERS BROCHURES)

Transducer	PCB	Endevco	Kulite	Kistler	Kistler
Type	102M58 Piezoelectric Built in amp.	8510 Piezoresistive	XTE-190 Piezoresistive	603B Piezoelectric Charge Mode	6602 Piezoelectric Built in amp.
Range	500 psi	15 psi-500 psi	25 psi-500 psi	30 psi-3000 psi	100-500 psi
Resonant Frequency (KHz)	500	100-500	100-350	>400	130
Rise time (μsec)	1.0	--	--	1.0	3.0
Time Constant (sec)	>5	$\sim\infty$	$\sim\infty$	--	25-110
Acceleration Sensitivity (psi/g) (Axial)	0.002	0.0004	0.0001-0004	< 0.0015	0.015
Flash Sensitivity (psi/°F)	--	0.003-0.01	--	--	--
Sensitivity (mv/psi)	+20	+20-+0.63	+20-+-.15	+0.35/pc/psi	-50-10
Linearity (+ percent F.S.)	1.0	0.5	1.0	1.0	1.0

mountings, construction of a device for in situ pressure calibration, and testing of transducer-face thermal shields.

1. TRANSDUCER MOUNTING

A cross-sectional sketch of the original transducer mounting arrangement is given in Figure 51. The sketch is drawn to scale. Transducers were installed directly into the steel mounting plates, which have dimensions of 15.2 cm x 61 cm x 1.9 cm (6 in. x 24 in. x 3/4 in.). The cover plates were secured to steel angle-iron supports with three recessed socket head cap screws on each of the two long sides. This arrangement was used in FAE tests to CD-5.

In a first attempt to reduce ringing, the mountings were modified by installing the transducers in simple plastic inserts which were epoxied into the steel plates. Delrin inserts were tried on FAE test CD-6, and teflon inserts were tried on the next and otherwise identical test, CD-8. The transducer ringing was not suppressed in either of these two tests.

A special FAE test (CDP-1) was then conducted in which four additional transducer mounting variations were examined for their effectiveness in reducing ringing. The arrangements tried were as follows:

a. A transducer was installed in a threaded washer which was potted into Biwax Corporation Type 601 encapsulant, as shown schematically in Figure 52(a). This encapsulant has been found in other applications to very effectively damp mechanical vibrations.

b. A transducer was potted into Biwax 601 as in (a), but the mounting plate was laminated. The laminations comprised a top layer of 7.94 mm (5/16 in.) steel and a bottom layer of 6.35 mm

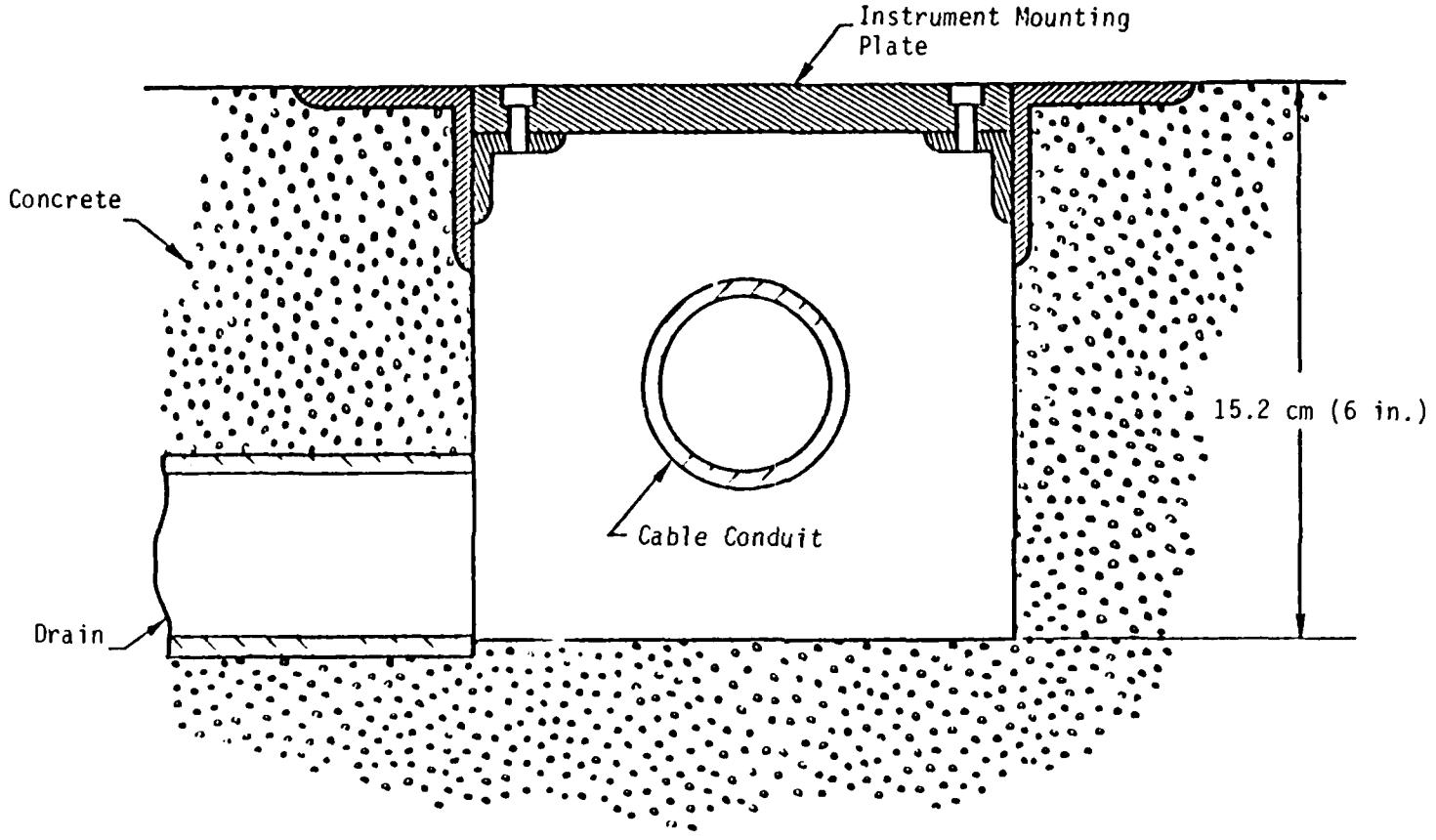

Figure 51. Cross-sectional view of instrumentation trough.

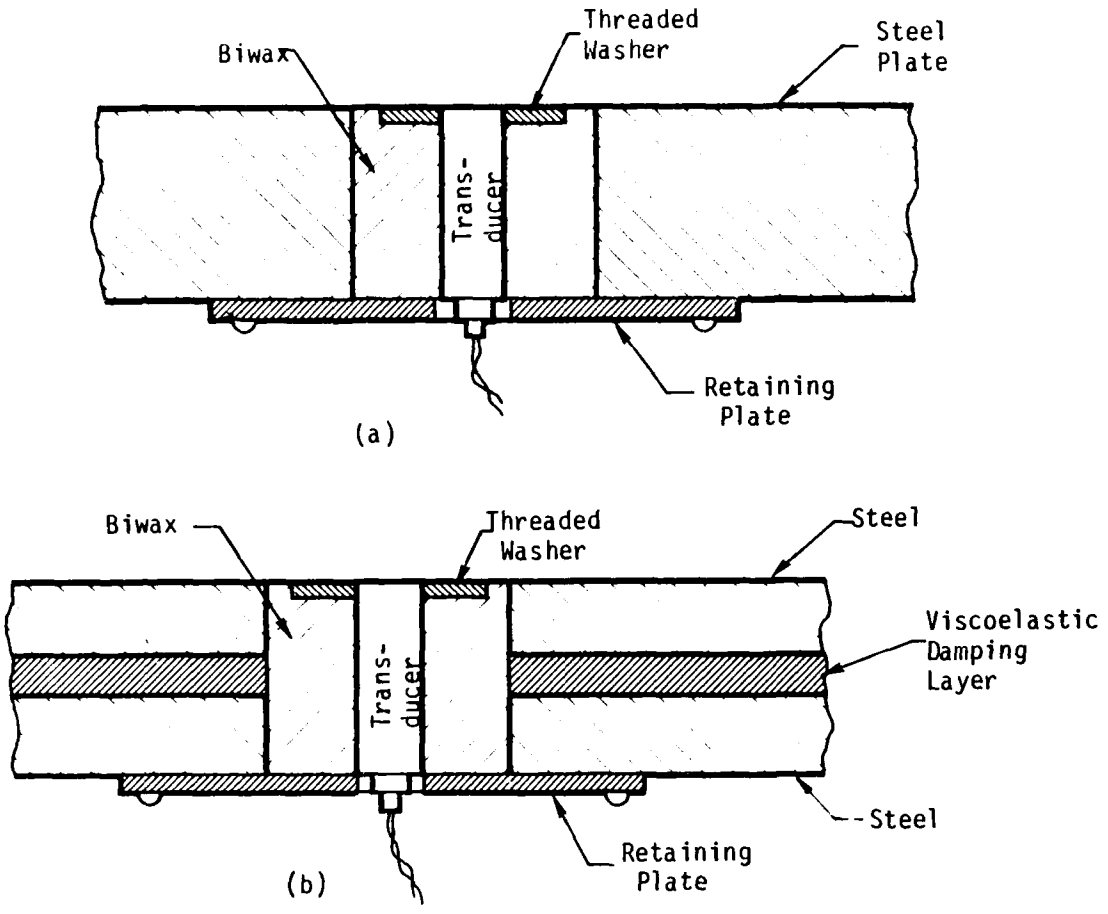

Figure 52. Transducer mountings: (a) Biwax suspension in steel plates, (b) Biwax suspension in laminated plate.

(1/4 in.) steel. A 4.76 mm (3/16 in.) thick layer of a viscoelastic compound (E.A.R. Corporation type C2003) was glued between the steel plates with Bostik adhesive. This arrangement is sketched in Figure 52(b). The overall thickness of this lamination was the same as the thickness of the other plates.

c. A mounting plate was made in which lamination, as in (b) above, was used, but without the Biwax suspension. The transducer was installed directly in the top steel plate of this laminate.

d. One of the mounting plates was rigidly pinned to the concrete floor of the instrumentation trough in which it was installed. The plate was securely bolted to five, 5 cm (2 in.) dia. steel reinforcing rods that had been grouted into the instrumentation trough with Burkestone hydraulic concrete. The plate itself was made of plain steel with a Delrin insert supporting the transducer.

In addition to these four mounting arrangements, one transducer was directly installed on a plain steel plate. On this same plate, a dummy transducer was installed in a blind hole. All of the plates were located on the test pad within 13.9 m (45.6 ft) of the explosion center. (Transducer ringing had not previously been significant beyond this range.)

When test CDP-1 was conducted, none of the four mounting techniques proved to be effective in significantly reducing ringing. The mounting arrangement in which both Biwax suspension and plate lamination were used yielded the best results, but ringing

was not eliminated. The results from the plain steel plate (on which both active and dummy gages were mounted) appear on Figure 53. The major frequency component in the pre-shock ringing of the active transducer was about 400 Hz. The major frequency component in the dummy gage signal (which has been scaled to pressure units) is about 1500 Hz.

In a second FAE test of this type (designated CDP-2), pairs of active transducers were mounted directly on each of three plain steel plates. Each pair consisted of a PCB piezoelectric transducer and an Endevco Model 8510 piezoresistive strain gage transducer. The resonant frequencies of these devices are 500 kHz and 240 kHz, respectively.

The objective of CDP-2 was to evaluate the relative performance of these two transducers when mounted in the simplest fashion. The Endevco transducer was chosen for comparison with the PCB because it has equivalent high frequency response capability, but is of a different generic type, with much lower acceleration sensitivity. Figure 54 gives the results of drop bar tests of these two transducers, using the apparatus described in References 20 and 21.

Figure 55 shows the results obtained from one of the three transducer pairs during test CDP-2. The two pressure records in this pair have been superimposed in absolute time with respect to detonation initiation. The overshoot that can be seen at the leading shock appeared only on the Endevco, a characteristic of that transducer which was also evident in shock tube tests. The Endevco record appears somewhat more finely detailed than that obtained from the PCB, possibly due to the difference in sensing element size. The sensing element diameter of the PCB is approximately 5.8 mm (0.23 in.), while that of the Endevco is 2.5 mm (0.10 in.).

On Figure 55 there appears to have been some negative displacement of the average PCB signal level. This is presently

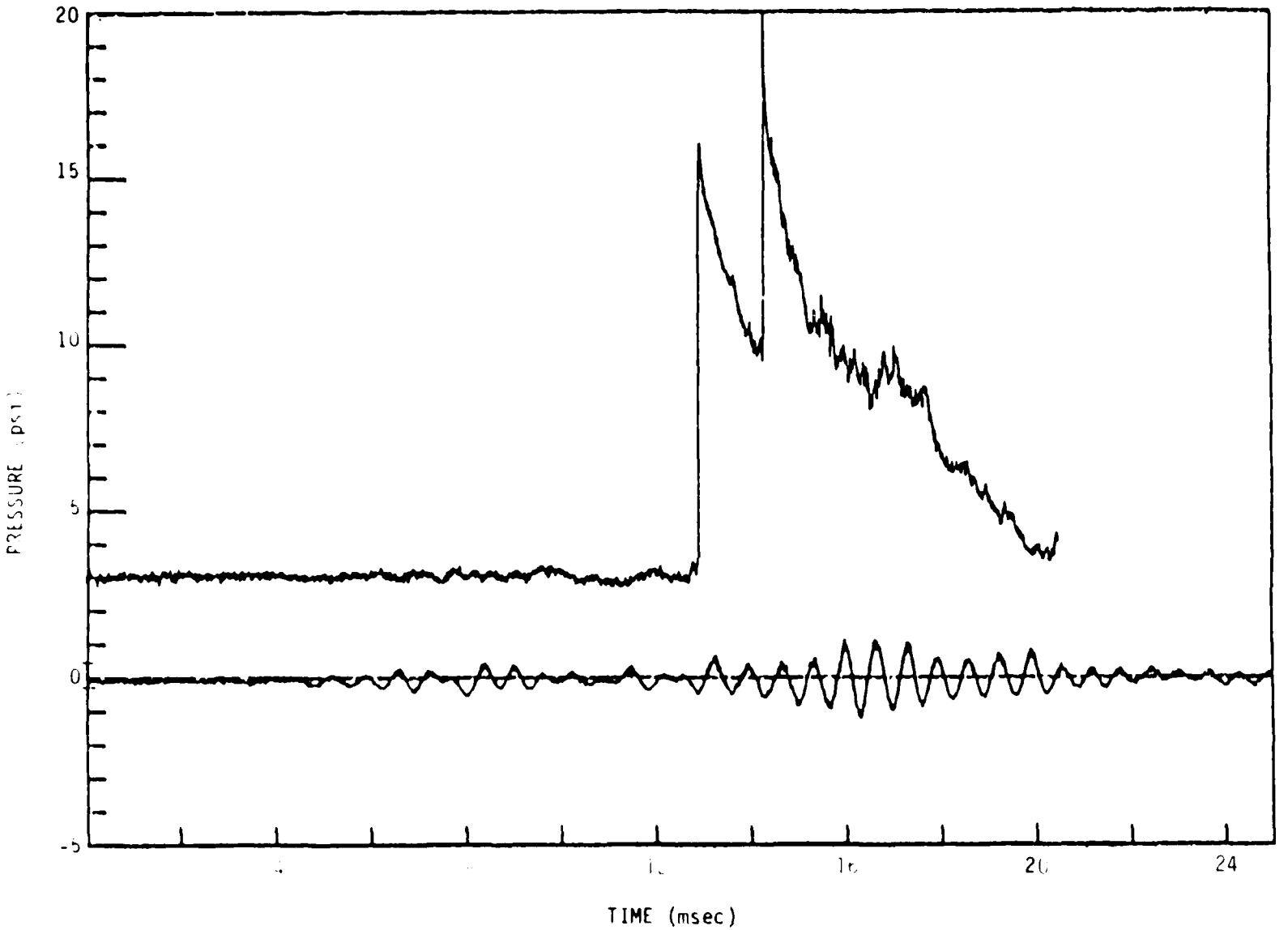

Figure 53. Active and dummy pressure gage records from FAE test CDP-1, 0.0265 m^3 (7 gal.) propylene oxide, R = 9.93 m (32.6 ft.). The dummy gage output has been converted to virtual pressure units for comparitive purposes.

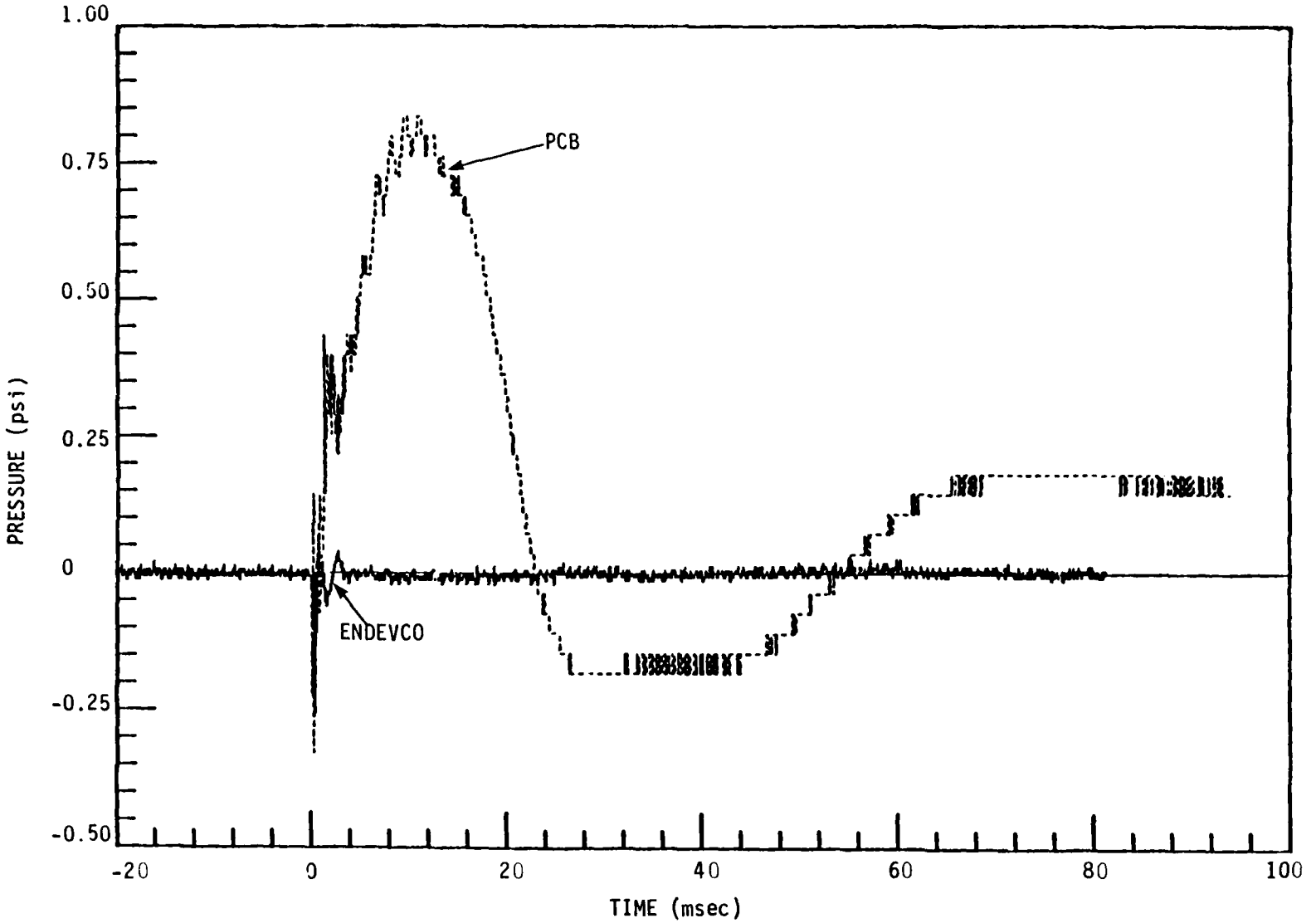

Figure 54. Results of drop bar acceleration sensitivity tests of PCB and Endevco transducers. Peak acceleration was ~980 m/s^2 (100 g) in both cases. Gage output was converted to virtual pressure units for comparitive purposes.

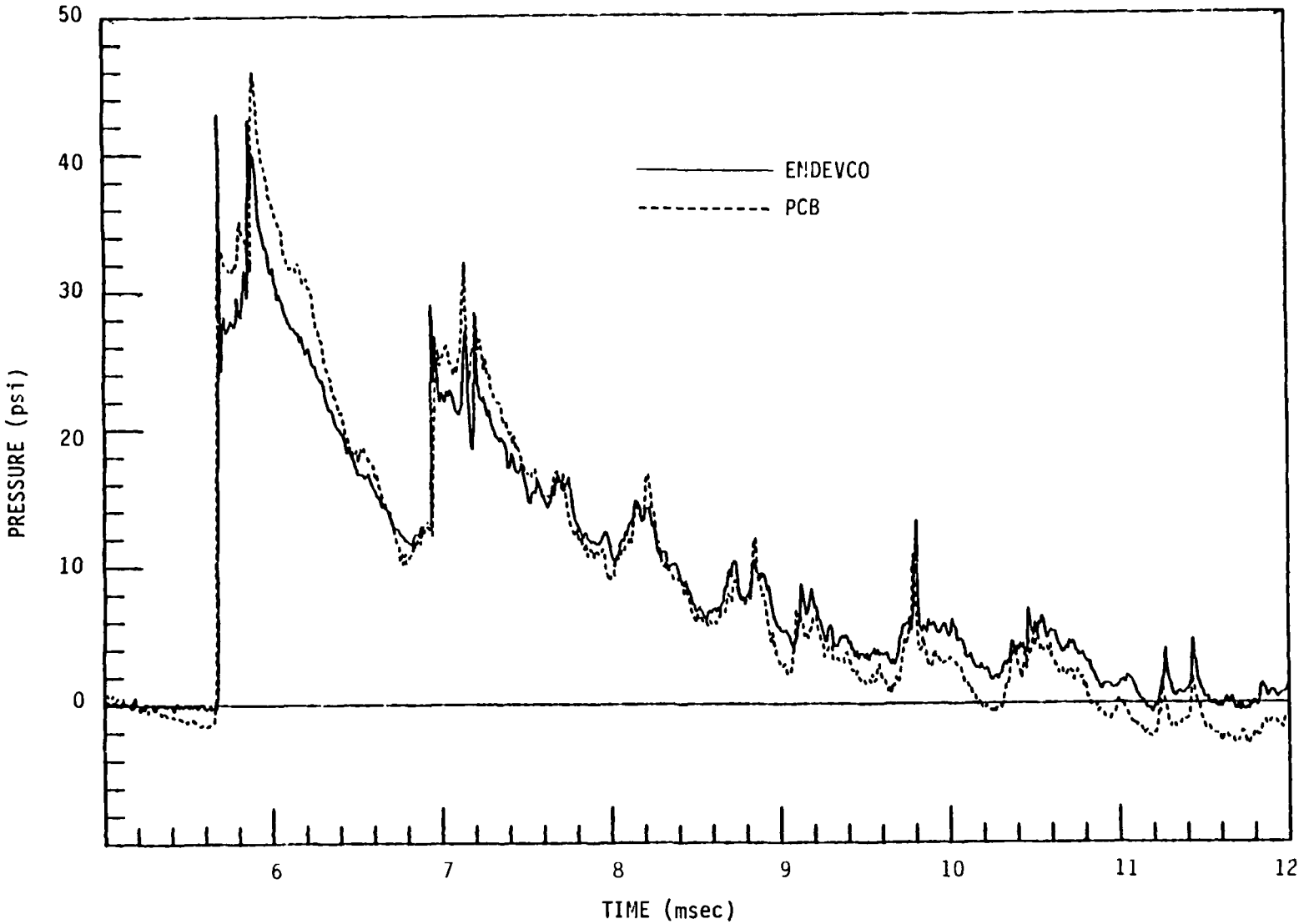

Figure 55. Pressure records obtained from FAE test CDP-2, 0.0265 m^3 (7 gal.) propylene oxide. Both transducers mounted at same location, R = 5.92 m (19.4 ft.).

believed to be due to inadequate thermal protection of the sensing element at the time of this test. The sensing element of the Endevco was protected with a graphite/silicon-grease compound (on the recommendation of the manufacturer). However, the coating used on the PCB was plain silicon grease, which was later shown to be ineffective as a thermal shield.

Noticible pre-shock ringing appeared only on the PCB pressure record. There was also a rather significant quantitative discrepancy between the two records during the first half-millisecond following shock passage. However, apart from the apparent negative drift in the PCB signal, the two transducers tracked very closely throughout the remaining positive phase.

Considering the magnitude of difference in acceleration sensitivity between the PCB and Endevco transducers that were used in test CDP-2, it was concluded from this that the post-shock oscillations on the pressure waveforms in Figure 55 must have been largely of gasdynamic origin. It was noted that the lower amplitude pressure oscillations were most prevalent in those records from transducer locations that are presumably engulfed by the expanding fuel-air cloud combustion products. It was felt that some of the oscillations at these locations may have been due to combustion product turbulence. In any event, the oscillations did not appear to be entirely the result of transducer acceleration sensitivity.

Since transducer ringing was not alleviated by simple modifications in the mounting arrangements, the decision was made to circumvent the problem in future work by employing piezoresistive type transducers at those locations that are close to the explosion source. The tradeoffs which may have to be made include the overshoot problem with some piezoresistive transducers, as well as possible difficulties with durability and serviceability. Alternatively, the use of piezoelectric transducers might be continued, but individual units should then be carefully selected for their low acceleration sensitivity. In drop tests of those PCB

transducers that were used in the presently reported FAE experiments, acceleration sensitivities in terms of virtual pressure varied over more than an order of magnitude, from a minimum of 1.4 Pa-s^2/m (0.002 psi/g) to a maximum of 21 Pa-s^2/m (0.03 psi/g).

2. IN-SITU PULSE PRESSURE TRANSDUCER CALIBRATOR

Most commercial pressure transducers are subject to changes in calibration due to weather conditions, aging of parts, connector cleanliness, and cable properties. Hysteresis effects may alter the calibration during loading. In order to establish confidence in the accuracy of pressure measurements, in situ calibration is essential, preferably before and after each experiment. For purposes of calibrating piezoelectric type transducers, a device is needed that will apply pressure to the sensing element in a time period that is short compared to the decay time constant of the transducer.

A pulse calibrator of this type was designed and built for in-situ use in conjunction with the FAE experiments. A photograph of the device appears in Figure 56. In this figure, a static pressure transducer is shown installed in the steel cover plate of one of the instrumentation troughs. The pulse calibrator head is resting on the cover to the right of the transducer. In use, the head would be centered over the transducer by means of scribed alignment markings on the cover plate.

The calibrator head is a modified D.C. electromagnet (Magnet Sales and Manufacturing Model EM-R6B) having a holding force of 2670 N (600 lb). An O-ring groove was machined into the face of this magnet. A small circular recess, 12.7 mm (1/2 in.) dia. x 1.59 mm (1/16 in.) deep, was cut into the center of the magnet face to prevent mechanical contact with the transducer, and a 3.18 mm (1/8 in.) diameter hole was drilled through the axis of the magnet. An electric solenoid-actuated valve (Skinner type X54) was mounted as closely as possible to the top surface of the magnet. The solenoid valve, which normally operates on 24 VDC, has an effective orifice

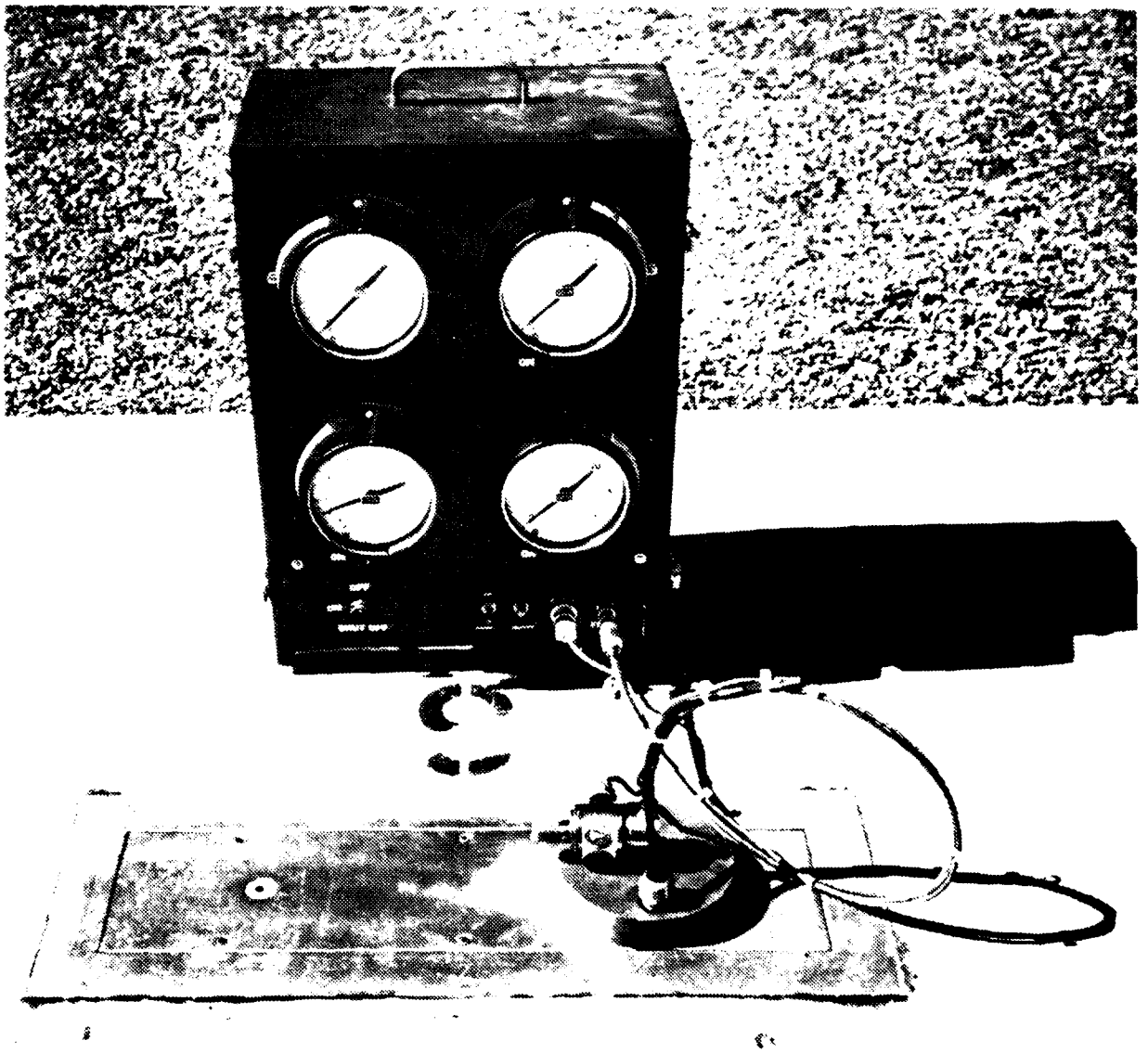

Figure 56. In-situ pressure transducer pulse calibrator.

diameter of 4.76 mm (3/16 in.), and a nominal opening time of 15 ms. For this application, faster opening was obtained by discharging a 3000μF capacitor at 250V through the solenoid with a momentary switch. The current decays to a steady-state level consistent with continuous solenoid operation through the use of a resistor in series with the 250V battery. The decay time constant is on the order of 200 ms.

The pressure source for calibration is nitrogen gas, which is stored in a 0.0038 m^3 (1 gal) bottle built into the portable gage case shown behind the instrumentation trough in Figure 56. This bottle is initially charged from a gas cylinder to the highest pressure needed in the calibrations. Nitrogen is then exhausted from the bottle as needed for lower pressure calibrations. The bottle is connected to the calibrator head with 6.4 mm (1/4 in.) I.D. plastic tubing. The very small volume expansion of the calibration gas that accompanies opening of the solenoid valve assures that the drop in source pressure will be negligible.

The source pressure is measured by one of four Ashcroft Model 1279A Bourdon tube pressure gages. These gages have a full scale accuracy of $\pm$ 0.5 percent. Their accuracy at part scale is proportionately lower. However, the ranges of the four gages used with the calibrator were chosen with sufficient overlap so that the maximum error of any reading over the entire pressure range of interest would not exceed approximately $\pm$ 1.5 percent.

In order to calibrate stagnation pressure stings in situ, the adaptor rack shown in Figure 57 was built. The sting is inserted into a retainer that was machined to fit the contour of the sting tip. A Conax packing gland type feedthrough connector securely nolds the sting in position, with its active surface flush with the steel inset on the adaptor rack. The sting is shown installed in the adaptor in Figure 57.

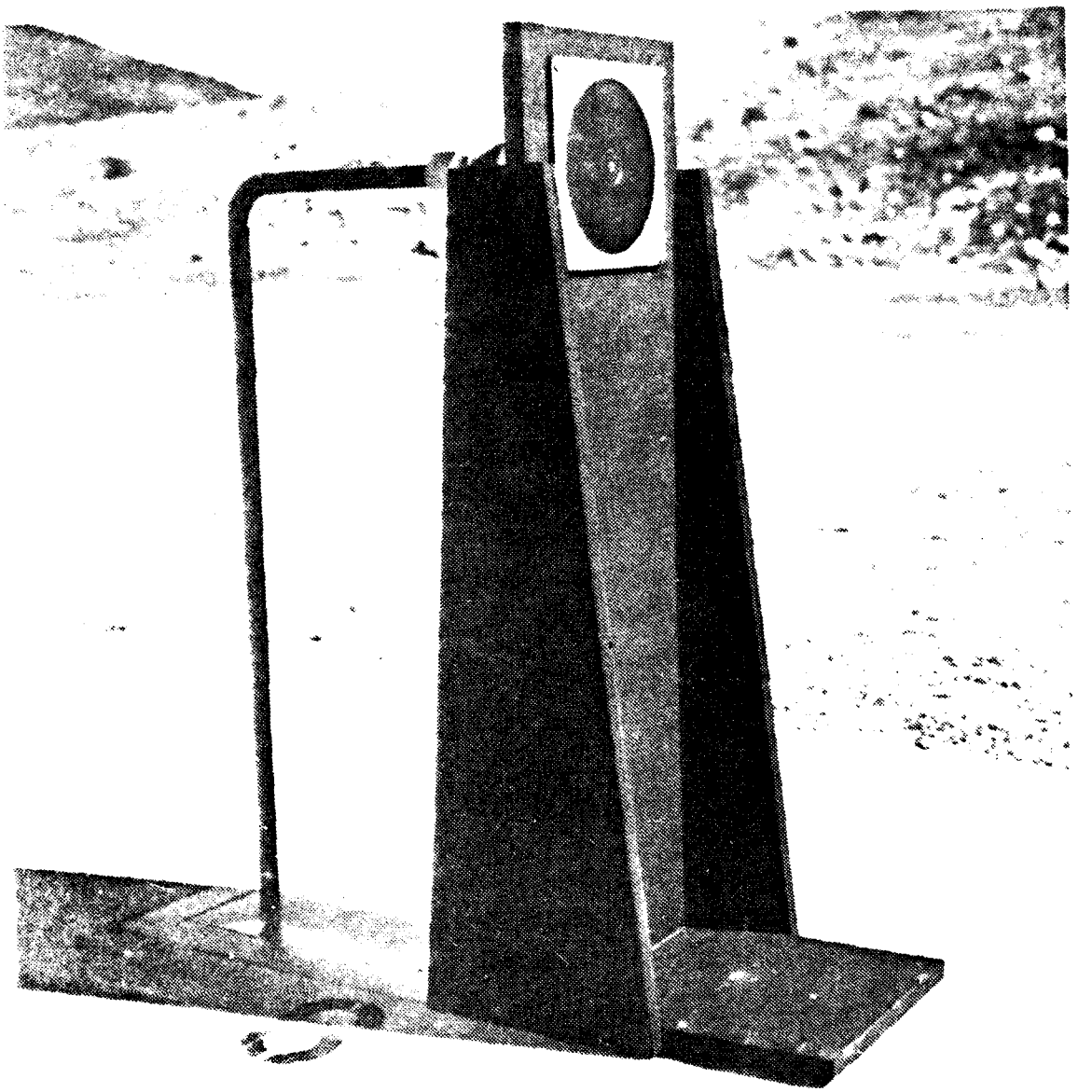

Figure 57. Pulse calibrator adaptor rack for use with stagnation pressure stings.

When the holding magnet is initially energized, a small transient signal is generated by the transducer. This signal is believed to be due to three mechanical effects: a slight displacement of internal components in the transducer by the magnetic force, impact of the electromagnet face with the trough cover, and a slight increase of pressure in the volume above the transducer due to the decrease in this volume. The transient signal decays quickly and does not interfere with the subsequent calibration process.

An example of the performance of the pulse calibrator is given in Figure 58. In this example, the supply pressure was 0.69 MPa (100 psi). The pressure risetime was about 7 ms. Oscillations with a mean frequency of about 80 Hz and having a half-wave amplitude of 4 percent of the average signal level continued for approximately 150 ms. The present overall calibration accuracy is therefore regarded as better than 4 percent. It may be possible to improve this accuracy somewhat by reducing the initial oscillations, through the use of a solenoid valve having a somewhat smaller effective orifice size (Reference 22).

The in-situ calibrator is useful for testing blast type pressure transducers immediately before and after FAE experiments. However, for assessment of response to shock waves, the transducers are periodically tested in a shock tube. An in-situ shock tube calibrator of the type described in Reference 23 could also be used for this latter purpose.

3. THERMAL SHIELDING

The piezoelectric pressure transducers used in the FAE experiments were found to be very sensitive to transient heating. The magnitude of error introduced into the positive-phase FAE blastwave pressure records by this effect was small but noticible at the 1/4-ton (nominal nuclear equivalent) scale. At that scale, most of the positive-phase durations, measured at ranges of interest, are

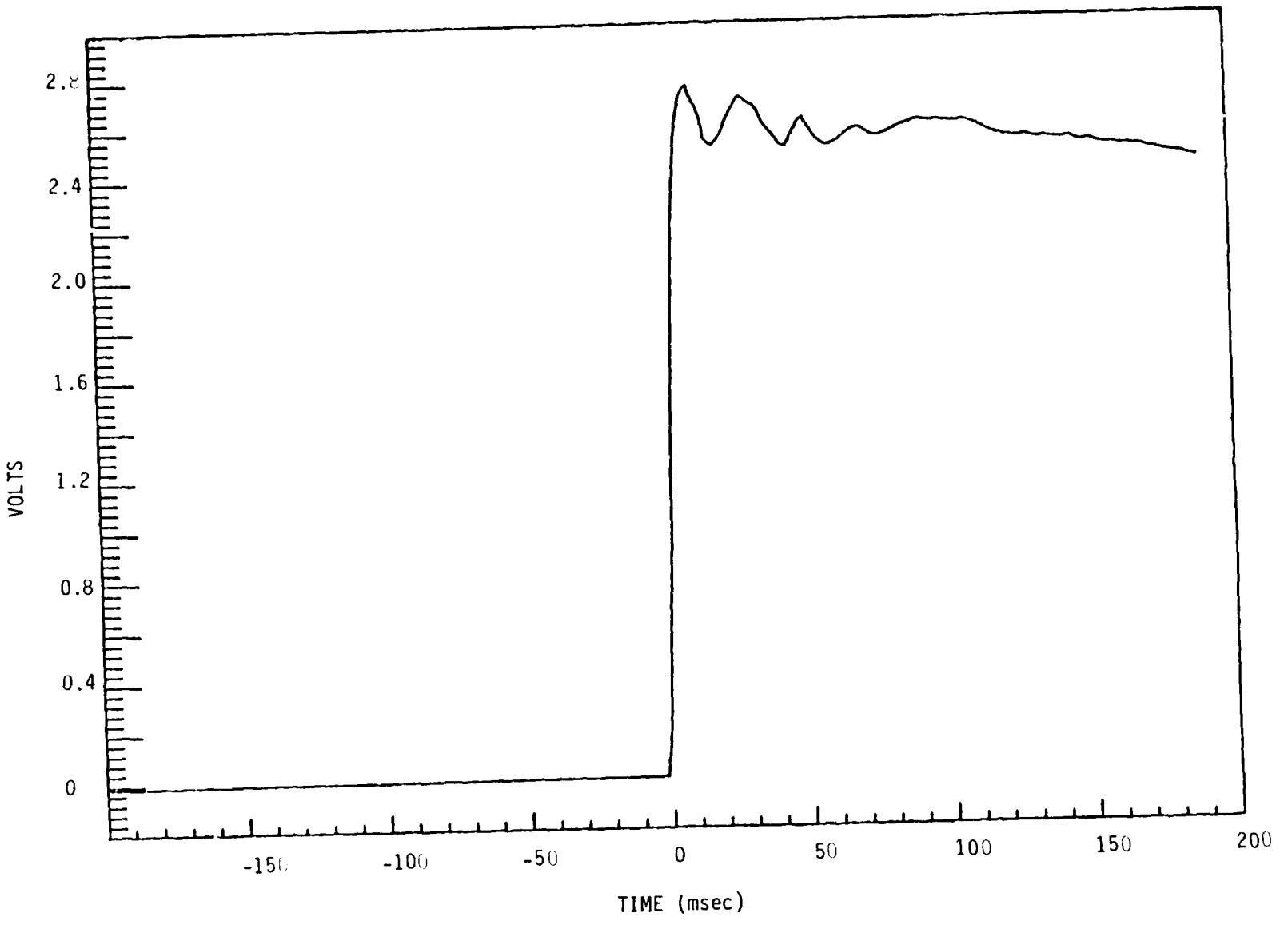

Figure 58. Voltage output from PCB pressure transducer using pulse calibrator. Calibration pressure was 0.69 MPa (100 psi).

less than 50 ms; those at positions having the greatest thermal loading are less than about 20 ms.

Figure 59(a) shows a 200 ms static pressure record from an FAE test, at a location that was just outside the initial cloud radius. The active surface of the transducer was in this case coated with a thin film of plain silicone grease. On other FAE tests, a single layer of 0.178 mm (0.007 in.) thick black plastic electrical tape had previously been used as a thermal and ablative shield, with similar results. The dramatic improvement in thermal shielding obtained by adding zinc oxide to the silicone grease coating, and used in conjunction with a single layer of black electrical tape, is illustrated by the example in Figure 59(b). The two traces in this figure are from different tests and taken with different transducers (of the same manufacture). However, the test conditions were very similar, and the transducers were located in the same position on the test pad.

Several types of easily applied thermal shields were systematically tested following the procedure described in Reference 24. A shielded test transducer and an unshielded control transducer were flush mounted on a metal plate. At a distance of 70 mm (2.75 in.) along the normal to the surface of this plate, a No. 22 photographic flash bulb was fired. This produces radiative rather than convective thermal loading, but it is felt that the relative effects of various forms of shielding would be similar in either case.

The output from the test transducer using different shield types is shown on Figure 60. The most effective shield tested consisted of a single layer of black electrical tape, coated with a commercial zinc-oxide/silicone grease heat sink compound (Chemtronics SL-1). Three layers of black tape (not shown on Figure 60) were almost as effective, but there was concern that this amount of tape might interfere with the transducer response.

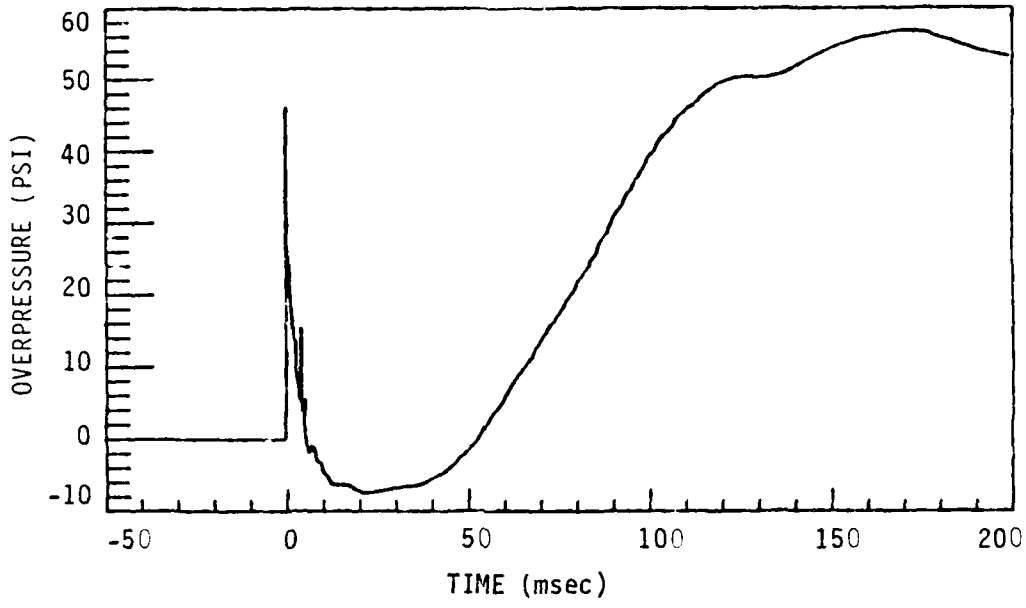

(a)

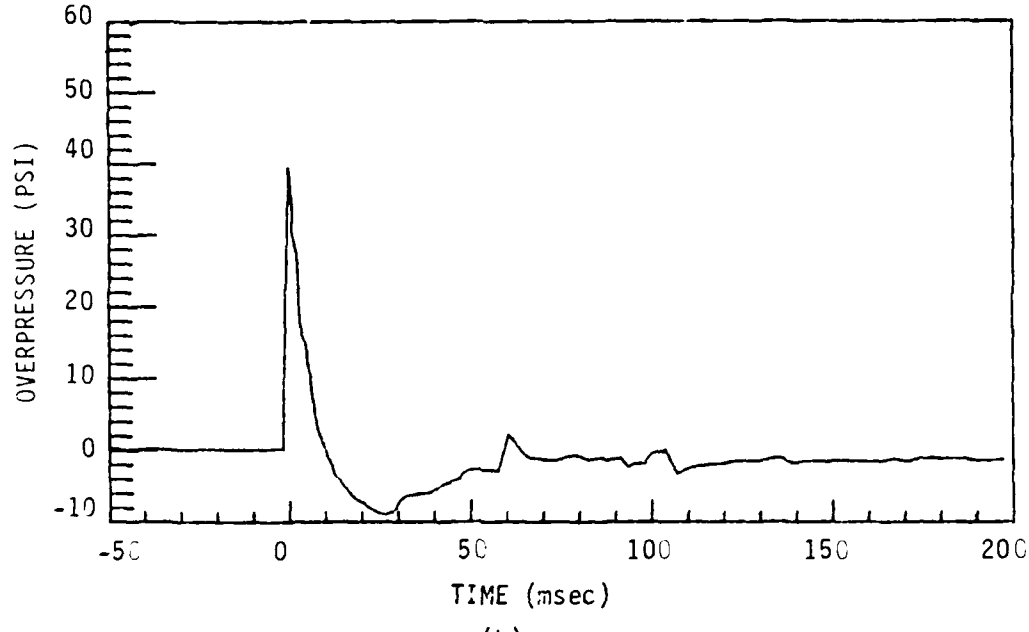

(b)

Figure 59. Pressure records obtained from FAE tests, 0.0265 m^3 (7 gal.) propylene oxide, R = 5.92 m (19.4 ft.). (a) Test CDP-2, transducer coated with silicon grease, (b) Test CD-14, transducer covered with black plastic electrical tape and coated with siliconegrease/zinc oxide compound.

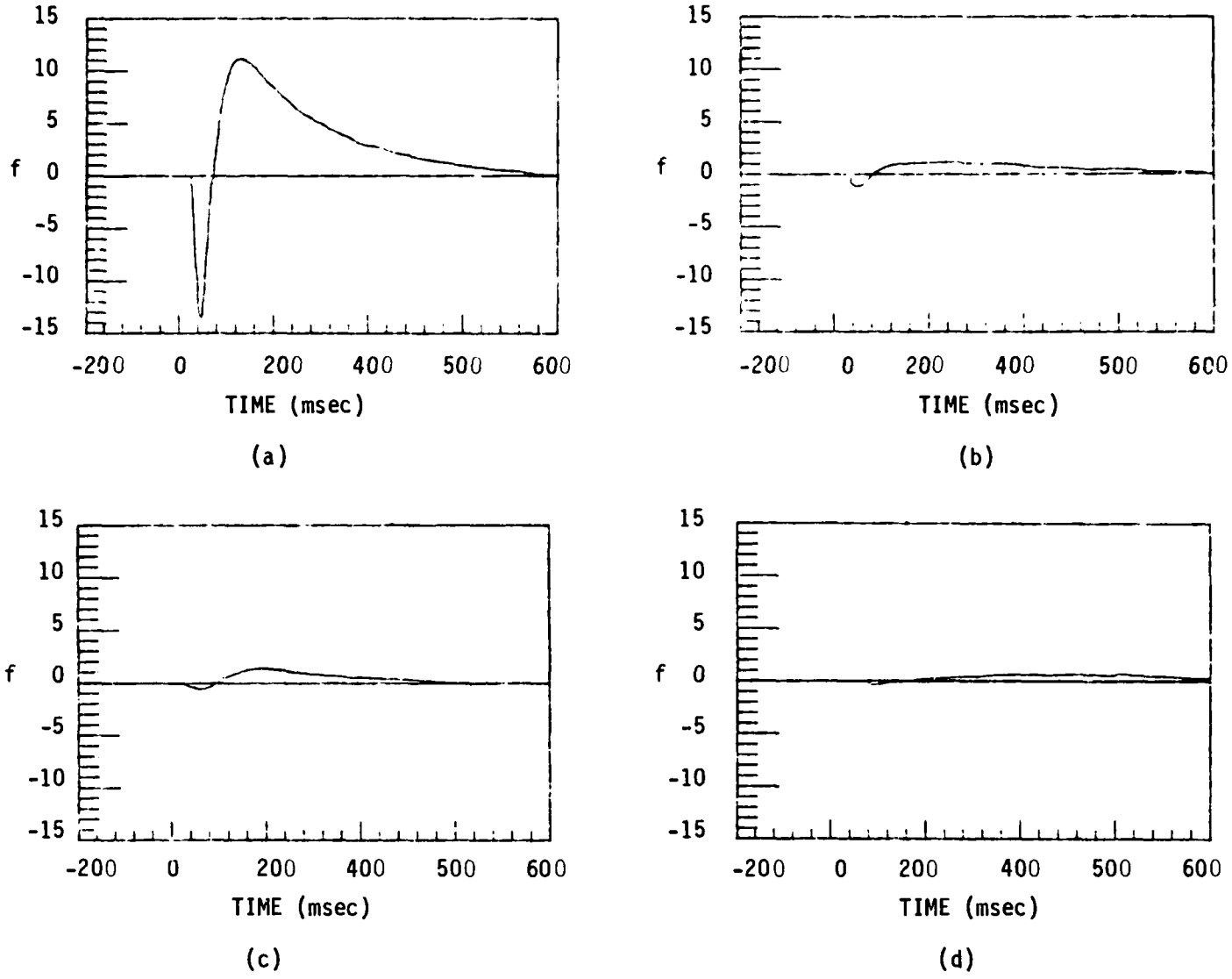

Figure 60. Pressure transducer response to radiative heat transfer. The response is normalized with respect to full scale output, expressed as the fractional value f. (a) unshielded transducer, b) transducer coated with thin layer of heat sink compound, (c) transducer covered with adhesive-backed aluminized mylar film, (d) transducer covered with black plastic electricians tape and thin layer of electrical heat sink compound.

At present, a single layer of electrical tape coated with heat sink compound is used with all piezoelectric transducers for FAE airblast measurements. The active face of the transducer is cleaned with acetone and the tape is carefully applied to avoid trapped air pockets. The transducer is then installed in a mounting plate (Figure 51). A jig is used so that when the transducer is securely fastened in place, the upper surface of the tape is 0.635 mm (0.025 in.) below the plate surface. The cavity above the transducer is then filled with the heat sink compound until the compound is flush with the top of the plate.

V. CONCLUDING REMARKS

Small-scale fuel-air clouds have been impulsively formed from a central source and detonated, but these clouds are not hemispherical, the positive-phase pressure decay is not always monotonic, and the pressure profiles frequently exhibit secondary wave systems. Large-scale impulsive jets from single nozzles have been produced, but the reach needed for a 1 KT simulator has not yet been attained. The data needed to realistically assess technical feasibility of a full-scale simulator installation have not been acquired. To complete the analysis of feasibility for a 1 KT FAE/nuclear airblast simulator, a number of additional investigations are needed.

a. Physical Feasibility

An important remaining question is whether secondary shocks and other waveform aberrations can be eliminated from the FAE airblast. If these are the result of cloud shape distortions then the question is more of a technological issue than a basic question of the FAE physics. Significant, impulse-carrying secondary waves were not clearly evident in the balloon tests conducted as part of Operation Distant Plain (References 8 and 9). In those tests, vapor-phase fuel was mixed with oxygen and the mixture confined in a balloon envelope prior to detonation. This indicates that, under conditions of accurate cloud shape, reasonable mixture uniformity, and point symmetric initiation, significant secondary wave systems may not form or may be essentially inconsequential. The simplified S^3 FAE airblast calculation (Reference 2) also showed secondary waves only in the negative phase under these conditions. However, that calculation assumed that the combustion products were chemically frozen. To investigate the possibility that second shocks might result from rapid chemical composition changes induced by cloud expansion, this calculation could be extended to include

local equilibrium and variable specific heats. The effects on secondary wave formation of cloud shape asymmetry, initiator location asymmetry, an extended detonation reaction zone, and fuel/air mixture inhomogeneities could also be treated analytically. Additionally, small-scale FAE balloon tests could be conducted to extend the Distant Plain data, with the objective of examining the existence of secondary waves under optimal conditions. Many of the problems with large-scale balloon testing are more manageable at smaller scales.

An expanded FAE data base is also needed to enable final judgements to be made as to the quality of simulation, repeatability and symmetry of the airblast that is generated when an impulsively formed fuel-air cloud is detonated. The data base should be updated as improvements in cloud shaping and fuel distribution uniformity are accomplished.

b. Technological Feasibility

Cloud formation remains one of the most serious technological problems that could impede the development of a reusable FAE/nuclear airblast simulator. The airblast from a non-hemispherical FAE is not likely to be point symmetric near the exploded cloud. It also appears possible that cloud misshapings may contribute to secondary wave systems. Further efforts in the area of cloud formation technology therefore seem essential to the advancement of the overall feasibility assessment.

c. Engineering Feasibility

Most of the previous experimental work dealing with single, impulsive jets has been of a survey nature. Systematic experiments at small and intermediate scales are now needed in order to more accurately anticipate the minimum requirements of a large-scale dispensing system. These tests should include the following

variables: nozzle diameter, dispensing pressure, volume of fuel dispensed, constancy of dispensing pressure, and the effects of fuel properties and additives. In addition, optional fuel pressurization schemes should be examined at the smallest practical scale.

REFERENCES

1. Sedgwick, R. T., Kratz, H. B., and Herrman, R. G., "Feasibility Investigation of a Permanent Fuel-Air Explosive Blast Simulator," DNA 5059T, August, 1978.

2. Pierce, T. H., and Sedgwick, R. T., "Fuel-Air Explosive Simulation of Far-Field Nuclear Airblasts," DNA 528C, December, 1979.

3. Duckworth, R. A., Mechanics of Fluids, N. Y., Longman, 1977.

4. Oppenheim, A. K., et al., "Blastwaves Generated by Exploding Clouds," in Shock Tube and Shock Wave Research, Ahlborn, B., et al., eds., University of Washington Press, Seattle, 1977.

5. Guirao, C. M., Bach, G. G., and Lee, J. H. S., "On the Scaling of Blastwaves from Fuel-Air Explosives," Sixieme Symposium International sur les Applications Militaires de la Simulation of Souffle, Deuxieme Partie, Centre D'Etudes de Gramat, Gramat, France, June, 1979.

6. Kogarko, S. M., Adushkin, V. V., and Lyamin, A. G., "An Investigation of Spherical Detonations of Gas Mixtures," Int. Chem. Engin., vol. 6, No. 3, July, 1966.

7. Desbordes, D., Manson, N., and Brossard, J., "Explosion dans L'Air de Charges Spheriques non Confinees de Melanges Reactifs Gazeux," Acta Astro., Vol. 5, 1978, p. 1009.

8. Reisler, R. E., and Ethridge, N. H., "Project 1.01 - Airblast Overpressure Phenomena," Operation Distant Plain Symposium, Vol. I, DASA 1947-1, AD821608, September, 1967.

9. Balcerzak, M. J., Johnson, M. R., and Lucole, S. W., "Nuclear Blast Simulation -- Detonable Gas Explosion, Operation Distant Plain," DASA 1945, Apr. 1967, p. 47.

10. Wisotski, J., and Snyer, W. H., "Characteristics of Blastwaves Obtained from Cylindrical High Explosive Charges," Denver Res. Inst. DRI 2286, University of Denver, November, 1965.

11. Reisler, R. E., "Explosive Yield Criteria," Minutes of the Explosives Safety Seminar (14th), AD-758990, 12 February, 1973, p. 271.

12. Bach, G. G., Knystautas, R., and Lee, J. H., "Initiation Criteria for Diverging Gaseous Detonations," Thirteenth Symposium (International) on Combustion, The Combustion Institute, Pittsburgh, 1971, p. 1097.

13. Oppenheim, A. K., Introduction to Gasdynamics of Explosions, Springer-Verlag, New York, 1970.

14. Edwards, D. H., Hooper, G., and Morgan, J. M., "An Experimental Investigation of the Direct Initiation of Spnerical Detonations," Acta Astro., Vol. 3, 1976, p. 117.

15. Ragland, K. W., Dabura, E. K., and Nicholls, J. A., "Observed Structure of Spray Detonations," Phys. Fluids, Vol. 11, No. 11, November, 1968, p. 2377.

16. Pierce, T. H., and Nicholls, J. A., "Time Variation in the Reaction-Zone Structure of Two-Phase Spray Detonations," Fourteenth Symposium (International) on Combustion, The Combustion Institute, Pittsburgh, 1973.

17. Pierce, T. H., and Nicholls, J. A., "Hybrid Gas-Phase/Two-Phase Detonations," Comb. Sci. and Tech., Vol. 9, 1974, p. 119.

18. Sedgwick, R. T., unpublished data, S-CUBED (formerly Systems, Science and Software), San Diego, California, 1977.

19. Sedgwick, R. T., et al., "Feasibility Investigation of a Permanent Fuel-Air Explosive Blast Simulator," DNA 5059, August, 1978.

20. Coleman, P., Ginn, W., and Grine, D., "Ground Motion Gauge Development," DNA 3702F, September, 1975.

21. Coleman, P. L., et al., "Review and Development of Ground Motion and Airblast Instrumentation," DNA 4036F, June, 1976.

22. Coulter, G. A., "Dynamic Calibration of Pressure Transducers at the BRL Shock Tube Facility," BRL MR 1843, AD654508, May, 1967.

23. Anson, W. A., "A Portable Shock Tube for Calibration of Piezoelectric Pressure Transducers In Situ," DRES Suffield TN-191, Ad825714, 13 December, 1967.

24. Hilten, J. S., et al., "Experimental Investigation of Means for Reducing the Response of Pressure Transducers to Thermal Transients," NBS TN961, January, 1978.

APPENDIX A

LISTING OF FAE TESTS CONDUCTED USING UPGRADED FACILITIES

Test[7]	Date	Time of Day	Air Temp. (°C)	Atmospheric Pressure ("Hg)	Relative Humidity (%)	Fuel				Dispenser		Initiator[5]		
						Type	Quantity (gal)	Additive	Temp. (°C)	Number of Nozzles	Dispensing Press. (psi)	Quantity (gm)	Height Above Nozzle (ft)	Total Delay[6] (ms)
CD-1	11-30-78	1238	25	NM[1]	NM	P.O.[2]	7	--	NM	600	NM	150	3.5	2000
CD-3	12-14-78	1045	19	NM	NM	P.O.	7	--	NM	600	100	500	5.0	800
CD-5	5-3-79	--	16	29.550	NM	P.O.	7	--	9	600	NM	500	1.3	570
CD-6	5-9-79	0940	16	29.380	NM	P.O.	7	--	7	600	NM	500	1.3	670
CD-8	5-11-79	1010	28	29.580	44	P.O.	7	--	18	600	210	500	1.3	670
CD-9	9-11-80	0925	19	29.490	75	Hept[3]	7	P.N.[4]	NM	600	NM	500	3.1	800
CD-10	9-18-80	1029	28	29.465	56	Hept	7	P.N.	NM	1400	250	500	3.0	800
CD-11	10-15-80	0938	17	29.810	65	Hept	7	P.N.	NM	1400	218	350	3.0	600
CD-12	10-22-80	1006	22	29.900	58	Hept	7	P.N.	NM	1400	220	350	3.0	325
CD-13	10-23-80	1058	29	29.546	32	P.O.	7	--	13	600	225	500	1.2	670
CD-14	11-14-80	0935	19	29.625	65	P.O.	7	--	7	600	240	350	1.2	1100
CD-P1	5-16-80	1635	19	29.455	56	P.O.	7	--	NM	600	NM	500	1.3	670
CD-P2	7-15-80	1404	28	29.490	40	P.O.	7	--	29	600	NM	500	1.3	670

Notes:

1. No measurement
2. Propylene oxide
3. Heptane
4. Propyl nitrate
5. High explosive type C-4
6. Including gas generator combustion time, dispensing time, and dwell.
7. Tests CD1-CD8 conducted under separate contract (Ref. 2)

APPENDIX B.

LISTING OF TESTS CONDUCTED TO EXAMINE CLOUD SHAPE MODIFICATIONS WITH NOZZLE BLOCKAGE(1)

Test(5)	Date	Fuel(3)	Dispensing Pressure (psi)	Blockage(2)	
				Type	Percent
CF16	10-2-80	Heptane	244	Dimple	2
CF20	10-13-80	Heptane	232	Dimple	10
CD11	10-15-80	Hept/PN(4)	218	Dimple	10
CD12	10-22-80	Hept/PN(4)	220	Dimple	15
CF15	9-25-80	Heptane	270	Dimple	20
CD10	9-23-80	Hept/PN(4)	250	Dimple	25
CF18	10-8-80	Heptane	204	Ring	5.5
CF19	10-10-80	Heptane	240	Ring	7.5
CF17	10-7-80	Heptane	243	Ring	10

NOTES:

1. Nozzle head has 1400 0.116 in. dia. holes (w/o blockage)
2. See text
3. 7 gallons dispensed in all tests
(4) Heptane and Propyl nitrate (See Appendix A)
(5) CF Designates test for cloud formation only (no detonation); CD designates cloud detonation test

DISTRIBUTION LIST

[illegible]

Assistant to the Secretary of Defense
Atomic Energy
ATTN: Executive Assistant

Defense Advanced Research Projects Agency
ATTN: TIO
ATTN: STO
ATTN: NMRO
ATTN: [illegible]

Defense Nuclear Agency
ATTN: SPSS
ATTN: SPWE
ATTN: TITL

Defense Technical Information Center
ATTN: DD

Department of Defense Explosives Safety Board
ATTN: Chairman

Field Command
DNA, [illegible]
Defense Intelligence Technical Liaison
ATTN: FCPR-1

Field Command
Defense Nuclear Agency
ATTN: FCPR
ATTN: FCTT, W. Summa
ATTN: FCTO
ATTN: FCTT
ATTN: FCT

Field Command Test Directorate
ATTN: FCTC

Joint Chiefs of Staff
ATTN: J-3
ATTN: C3S

Joint Chiefs of Staff, Washington
ATTN: [illegible] Space Tech (OS)

DEPARTMENT OF THE ARMY

Deputy Chief of Staff
ATTN: DAMO-RQC
ATTN: DAMO-NCW-F

Harry Diamond Laboratories
ATTN: DELHD-N-P
ATTN: DELHD-N-P, W. Dalton
ATTN: DELHD-N-RBH-S
ATTN: DELHD-N-P, D. Kanter

Picatinny Arsenal
ATTN: SMUPA-[illegible]

U.S. Army Engineer Waterways Experiment Station
ATTN: WESSA, W. Flathau
ATTN: WESSD, J. Jackson
ATTN: Library

U.S. Army Materiel Dev & Readiness Cmd
ATTN: DRXAM-TL

U.S. Army Missile Command
ATTN: DRSMI-AO

U.S. Army Nuclear & Chemical Agency
ATTN: Library
ATTN: MONA-OPS, C. Vortman

USA Missile Command
ATTN: Documents Section

DEPARTMENT OF THE NAVY

David Taylor Naval Ship R&D Ctr
ATTN: Code 17
ATTN: Code 1844
ATTN: Code 1843, Library
ATTN: Code 1720
[illegible] ATTN: Code 1740.5, E. Wang

Naval Civil Engineering Laboratory
ATTN: Code L51, J. Crawford
ATTN: Code L51

Naval Electronic Systems Command
ATTN: PME 117-21

Naval Facilities Engineering Command
ATTN: Code 04B

Naval Material Command
ATTN: MAT 08T-22

Naval Research Laboratory
ATTN: Code 2627, Tech Lib

Naval Sea Systems Command
ATTN: SEA-0322
ATTN: SEA-0351
ATTN: SEA-09G53, Lit

Naval Surface Weapons Center
ATTN: Code R40, I. Blatstein
ATTN: Code F31
ATTN: Code R11
ATTN: Code R14

Naval Surface Weapons Center
ATTN: Tech Library & Info Svcs Br

Office of the Deputy Chief of Naval Ops
ATTN: NOP 04BG
ATTN: NOP 981

Office of Naval Research
ATTN: Code 474, N. Perrone

DEPARTMENT OF THE NAVY (Continued)

Strategic Systems Project Office
ATTN: NSP-272
ATTN: NSP-43

DEPARTMENT OF THE AIR FORCE

Air Force
ATTN: INT

Air Force Geophysics Laboratory
ATTN: LWH, H. Ossing

Air Force Institute of Technology
ATTN: Library

Headquarters
Air Force Systems Command
ATTN: DLW

Air Force Weapons Laboratory
ATTN: NTE, M. Plamondon
ATTN: NTED, E. Seusy
ATTN: NTES
ATTN: SUL
ATTN: NTEO

Air University Library
ATTN: AUL-LSE

Ballistic Missile Office/DAA
ATTN: PP
ATTN: ENBF, D. Gage
ATTN: ENSN

Deputy Chief of Staff
Research, Development, & Acq
ATTN: AFRDQI

Strategic Air Command
ATTN: DOTP
ATTN: NRI STINFO Library

DEPARTMENT OF ENERGY

Department of Energy
Albuquerque Operations Office
ATTN: CTID
ATTN: D. Richmond

Division of Military Application
ATTN: DMA/RDNT

Nevada Operations Office
ATTN: Doc Con for Technical Library

OTHER GOVERNMENT AGENCY

Central Intelligence Agency
ATTN: OSWR/NED

NASA

NASA Scientific & Tech Info Facility
ATTN: Acquisitions Branch

DEPARTMENT OF ENERGY CONTRACTORS

Sandia National Laboratories
ATTN: Lib & Sec Class Div

DEPARTMENT OF ENERGY CONTRACTORS (Continued)

University of California
Lawrence Livermore National Lab
ATTN: Technical Info Dept Library

Los Alamos National Laboratory
ATTN: Reports Library
ATTN: J. Hopkins

Sandia National Laboratories
ATTN: Tech Lib 3141

DEPARTMENT OF DEFENSE CONTRACTORS

Aerospace Corp
ATTN: Library Acquisition M1/199

Applied Research Associates, Inc
ATTN: N. Higgins
ATTN: J. Bratton

Applied Research Associates, Inc
ATTN: J. Shinn

Applied Research Associates, Inc
ATTN: D. Piepenburg

Applied Research Associates, Inc
ATTN: R. Frank

BDM Corp
ATTN: Corporate Lib
ATTN: T. Neighbors

Boeing Co
ATTN: Aerospace Library

California Research & Technology, Inc
ATTN: K. Kreyenhagen
ATTN: M. Rosenblatt

California Research & Technology, Inc
ATTN: F. Sauer
ATTN: D. Orphal

Cushing Associates
ATTN: V. Cushing

EG&G Wash Analytical Svcs Ctr, Inc
ATTN: Library

Electro-Mech Systems, Inc
ATTN: R. Shunk

Electro-Mech Systems, Inc
ATTN: L. Piper

GEO Centers, Inc
ATTN: E. Marram

H-Tech Labs, Inc
ATTN: B. Hartenbaum

IIT Research Institute
ATTN: Documents Library

Institute for Defense Analyses
ATTN: Classified Library

DEPARTMENT OF DEFENSE CONTRACTORS (Continued)

JAYCOR
ATTN: Library

Kaman Sciences Corp
ATTN: Library

Kaman Sciences Corp
ATTN: E. Conrad

Kaman Tempo
ATTN: DASIAC

Kaman Tempo
ATTN: DASIAC

Lockheed Missiles & Space Co, Inc
ATTN: T. Geers, Orgn 52-33
ATTN: Technical Library

Lockheed Missiles & Space Co, Inc
ATTN: S. Taimuty, Dept 81-74/154
ATTN: TIC-Library

Martin Marietta Denver Aerospace
ATTN: D-6074, G. Freyer

Mitre Corp
ATTN: MS E190

National Technical Systems
ATTN: P. Ieberman

University of New Mexico
ATTN: G. Leigh
ATTN: N. Baum
2 cy ATTN: D. Calhoun

University of New Mexico
ATTN: CERF, N. Baum

Pacific-Sierra Research Corp
ATTN: H. Brode, Chairman SAGE

Pacifica Technology
ATTN: G. Kent

Physics Applications, Inc
ATTN: F. Ford

Physics International Co
ATTN: E. Moore
ATTN: Technical Library

R&D Associates
ATTN: J. Lewis
ATTN: Technical Information Center
ATTN: D. Simons
ATTN: C. Lee
ATTN: P. Haas

DEPARTMENT OF DEFENSE CONTRACTORS (Continued)

Rand Corp
ATTN: P. Davis

Rand Corp
ATTN: B. Bennett

S-CUBED
ATTN: D. Grine
ATTN: Library
2 cy ATTN: T. Pierce
2 cy ATTN: M. Groethe
2 cy ATTN: R. Sedgwick

Science Applications, Inc
ATTN: Technical Library

Science Applications, Inc
ATTN: M. Knasel
ATTN: W. Layson
ATTN: J. Cockayne

Southwest Research Institute
ATTN: A. Wenzel
ATTN: W. Baker

SRI International
ATTN: J. Colton
ATTN: G. Abrahamson

Structural Mechanics Associates, Inc
ATTN: R. Kennedy

Teledyne Brown Engineering
ATTN: F. Leopard
ATTN: D. Ormond

TRW Electronics & Defense Sector
ATTN: Technical Information Center
ATTN: D. Baer
2 cy ATTN: N. Lipner

TRW Electronics & Defense Sector
ATTN: P. Dai
ATTN: E. Wong

Weidlinger Assoc, Consulting Engrg
ATTN: M. Baron

Weidlinger Assoc, Consulting Engrg
ATTN: J. Isenberg

Weidlinger Assoc, Consulting Engrg
ATTN: A. Misovec

END

FILMED

2-85

DTIC